AN ABSTRACT OF THE THESIS OF

Robert A. Maffione for the degree of Doctor of Philosophy in Oceanography presented on August 9, 1996. Title: Optical Backscattering and Submerged Source Techniques for Characterizing the Optical Properties of the Ocean.

Redacted for privacy

Abstract approved: J. Ronald V. Zaneveld

Characterizing the optical properties of the ocean has traditionally involved measuring daylight submarine light-field quantities, most commonly plane irradiance and upwelling radiance, from which certain apparent optical properties (AOP's) can be derived. As useful as these measurements are, fundamental progress in optical oceanography also requires the determination of inherent optical properties (IOP's). Comparison of IOP's has also been problematic because, unlike radiometric measurements, there are no agreed-upon methods or standards for the characterization and calibration of IOP instruments. New instruments and methods, which include theoretical advances in raditiave transfer theory, have been developed for accurately measuring IOP's, specifically the absorption, beam attenuation, and backward scattering coefficients, and the volume scattering function (VSF) at and near 180°.

The fixed-angle backscattering-measurement approach is investigated for the application of measuring b_b. Several backscattering sensors were

developed with different optical geometries, which are shown to be accurately calibrated using a rigorous method that is partially traceable to an NIST reflectance standard. A unique instrument was developed, called Beta Pi, that measures the VSF at and near 180 degrees and was modified to include a novel variable pathlength transmissometer that is shown to make the instrument completely self calibrating, yielding highly accurate IOP measurements. Measurements in the Gulf of Mexico revealed that the VSF increases by more than 50% from 179° to 180°. A sharp enhancement, possibly due to coherent backscattering, was also observed at 180° with an angular width of about 0.03°. Submerged source techniques were developed and conducted as experiments for testing aspects of radiative transfer theory, and are shown to be a useful and accurate means for characterizing the optical properties of ocean water and ice. The irradiance attenuation due to an isotropic light source was used to calculate the absorption coefficient from an exact equation that is essentially Gershun's famous equation transformed to spherical coordinates. A novel method for measuring the complete beam spread function (BSF) of sea ice was developed, and measurements were made of first- and multi-year ice off the shore of Barrow, Alaska. All of the measured sea ice BSF's were drastically different than the BSF of ocean water, and they strongly indicated that sea ice is a highly scattering medium, with a single scattering albedo generally greater than 0.97. At pathlengths greater than 30 cm, the BSF was found to be nearly identical to the computed asymptotic radiance distribution.

Optical Backscattering and Submerged Source Techniques for Characterizing the Optical Properties of the Ocean

by

Robert A. Maffione

A Dissertation

submitted to

Oregon State University

in partial fulfillment of
requirement for the
degree of

Doctor of Philosophy

Completed August 9, 1996
Commencement June 1997

Doctor of Philosophy thesis of Robert A. Maffione presented on August 9, 1996

APPROVED:

Redacted for privacy

Major Professor, representing Oceanography

Redacted for privacy

Dean of College of Oceanic and Atmospheric Sciences

Redacted for privacy

Dean of Graduate School

I understand that my thesis will become part of the permanent collection of Oregon State University libraries. My signature below authorizes release of my thesis to any reader upon request.

Redacted for privacy

Robert A. Maffione, Author

ACKNOWLEDGMENTS

It is with deep affection and gratitude toward my many friends and colleagues, without whom I never would have come this far, that I happily write this page. If I manage to glimpse anything in oceanography, I do so standing on the shoulders of Dick Honey, who first got me into this mess and who mentored me while I practiced optical oceanography without a license. He and many other associates at SRI International, where I cut my teeth, will always share my gratitude and affection.

Curt Mobley, whom I first met as my sponsor at ONR, later becoming my colleague and dear friend, provided much needed moral support and guidance through the mine-laden world of academic science. Without his voice of reason through my darkest days in graduate school, I surely would have left oceanography to spend the rest of my days exploring the canyons of southeastern Utah. I owe a great debt of appreciation to David Dana, engineer extraordinarie, who devoted enormous hours designing and building the ocean-optical instrumentation that made a large part of this thesis possible. His incredible ability as a sounding board for ideas, and his advice in many areas of life, have helped me to steer a steady course.

I am eternally grateful for the friendship and support shown to me by Gary Gilbert. To steal a terrestrial metaphor, he sees the ocean when looking at the water molecules, which is a rare gift. I have enjoyed and been enriched by our philosophical discussions, and can only hope that the best are still ahead. Jim Christmann, friend and captain, has kept me dry, though

sometimes seasick, over many years of fishing for knowledge in Monterey Bay. His good nature and love of life and people have been an inspiration.

Before I ever began writing, or even thinking about this thesis, many Saturday's were spent with Kieran O'Driscoll and Antonio Martinez, the three of us struggling persistently through practice comprehensive exam questions. I learned more physical oceanography during those Saturdays when we debated and worked problems than in all the courses I took at OSU combined. Saturday nights at Squirrels didn't seem to hurt either, since together we all passed the dreaded comprehensive exam. My warmest appreciation to Irma Delson, who took care of all of my administrative loose ends, which were many, and always made me feel welcome. I thank my committee for their time in struggling through this thesis, and especially Ron Zaneveld for his helpful comments and spirited debates.

No words can express the depth of my love and affection for Nancy Alimonti, who put up with me day and night during the six months I spent in Tucson writing this thesis. Without her selfless help and caring, incredible cooking, beautiful smile, and above all patience while I struggled along, I would have lost my sanity or taken years to complete my dissertation. I am forever in her debt, which at least seems to keep her smiling.

Finally, I wish to sincerely thank the Environmental Optics Program at the Office of Naval Research, in particular the program managers Rick Spinrad, Curt Mobley, Gary Gilbert, and Steve Ackleson, for their generous financial support of my research.

CONTRIBUTION OF AUTHORS

Ken Voss and Richard Honey were co-investigators in taking the oean data shown in Chapter 4, "Measurement of the spectral absorption coefficient in the ocean with an isotropic source." Richard Honey originally conceived of the isotropic light-source experiment.

TABLE OF CONTENTS

Page

1. INTRODUCTION 1

2 INSTRUMENTS AND METHODS FOR MEASURING THE BACKWARD-SCATTERING COEFFICIENT OF OCEAN WATERS. 8

2.1 ABSTRACT 9

2.2 INTRODUCTION 10

2.3 BACKGROUND 12

2.3.1 History 12

2.3.2 Optical Properties — Notation and Definitions 17

2.4 GENERAL ANALYSIS OF BACKSCATTERING SENSORS 19

2.5 DESCRIPTION AND ANALYSIS OF PARTICULAR BACKSCATTERING SENSORS 29

2.5.1 Optical Design of the BBC-4 29

2.5.2 Calibration Analysis 31

2.5.2.1 Authors' Backscattering Sensors 31
2.5.2.2 APL Backscattering Sensor 40
2.5.3 Estimation of the Backward Scattering Coefficient 43

2.6 SUMMARY AND CONCLUSIONS 49

3. *IN-SITU* CHARACTERIZATION OF OPTICAL BACKSCATTERING AND ATTENUATION FOR LIDAR APPLICATIONS 52

3.1 ABSTRACT 53

3.2 INTRODUCTION 53

3.3 LIDAR MODELS 57

3.4 *IN-SITU* INSTRUMENTATION: BETA PI 61

3.5 RESULTS FROM GULF OF MEXICO NEAR PANAMA CITY, FLORIDA 69

TABLE OF CONTENTS (CONTINUED)

Page

4. MEASUREMENT OF THE SPECTRAL ABSORPTION COEFFICIENT USING AN ISOTROPIC SOURCE IN THE OCEAN 74

4.1 ABSTRACT 75

4.2 INTRODUCTION 75

4.3 THEORETICAL DEVELOPMENT 78

4.3.1 Derivation of the Vector and Scalar Irradiance from an Isotropic Source Embedded in the Ocean 78

4.3.2 Solution for the Absorption Coefficient 86

4.4 DATA 92

4.5 SUMMARY AND CONCLUSIONS 95

5. THE AVERAGE COSINE DUE TO AN ISOTROPIC LIGHT SOURCE IN THE OCEAN 96

5.1 ABSTRACT 97

5.2 INTRODUCTION 98

5.3 APPROACH 101

5.4 THEORY 107

5.4.1 Limiting Values of the Average Cosine Due to an IPS 107

5.4.1.1 The Limit $r \rightarrow \infty$. 107
5.4.1.2 The Limit $r \rightarrow 0$. 109
5.4.1.3 Limit for a Finite Source 111

5.4.2 The Mean Light Path and the Absorption Coefficient 113

5.5 RESULTS 116

5.5.1 Comparison of Simulations with Measured PSF's 116

5.5.2 Model of the Average Cosine 120

5.5.3 Determining the Absorption Coefficient 124

TABLE OF CONTENTS (CONTINUED)

Page

5.6 CONCLUSIONS 128

6 IN-SITU MEASUREMENTS OF THE BEAM SPREAD FUNCTION OF SEA ICE 132

6.1 ABSTRACT 133

6.2 INTRODUCTION 134

6.3 INSTRUMENTS AND METHODS 138

6.4 RESULTS 143

6.5 DISCUSSION 156

6.6 CONCLUSION 163

7. CONCLUSIONS 165

7.1 SUMMARY 165

7.2 FUTURE RESEARCH 172

BIBLIOGRAPHY 175

LIST OF FIGURES

Figure		Page
2.1	SCHEMATIC LAYOUT OF THE FIRST OPTICAL BACKSCATTERING SENSOR	14
2.2	THE SECOND GENERATION BACKSCATTERING SENSOR DEVELOPED AT SRI IN 1991	16
2.3	OPTICAL GEOMETRY FOR A GENERIC FIXED-ANGLE BACKSCATTERING SENSOR	20
2.4	OPTICAL GEOMETRY FOR ANALYZING THE SENSOR RESPONSE TO A LAMBERTIAN TARGET.	25
2.5	SCHEMATIC OF THE BACKSCATTERING-SENSOR OPTICS OF THE BBC-4	30
2.6	**FIGURE 2.6** WEIGHTING FUNCTIONS OF THREE BACKSCATTERING SENSORS WITH DIFFERENT OPTICAL GEOMETRIES.	32
2.7	$W(z;c)$ FOR THE BBC-4 AND PETZOLD AVERGE PHASE FUNCTION PLOTTED AS A FUNCTION OF THE SCATTERING ANGLE Ψ.	34
2.8	AS COMPUTED FROM THE TWO CURVES IN FIGURE 2.7.	35
2.9	$W(z;c)$ FOR THREE VALUES OF c	37
2.10	THE ATTENUATION CORRECTION FACTOR $\sigma(c,c_w)$ COMPUTED FOR THE 440 NM CHANNEL OF THE BBC-4	39
2.11	WEIGHTING FUNCTION $W(z;c_w)$	41
2.12	THE ATTENUATION CORRECTION FACTOR $\sigma(c,c_w)$ FOR THE APL BACKSCATTERING SENSOR	43
2.13	VSF MEASUREMENTS BY *PETZOLD* [1972], NORMALIZED BY THE FACTOR $2\pi/b_b$.	47
3.1	SCHEMATIC LAYOUT OF "BETA PI," THE INSTRUMENT THAT MEASURES THE VOLUME SCATTERING FUNCTION AT AND NEAR 180 DEGREES	62
3.2	GEOMETRY FOR MEASURING THE VSF AT AND NEAR 180 DEGREES.	64

LIST OF FIGURES (Coninued)

Figure		Page
3.3	THE VIGNETTING CORRECTION FUNCTION, $G(\theta) = 2c\int_0^\infty f(r,\theta)e^{-2cr}dr$, FOR VALUES OF C RANGING FROM 0.1 TO 0.5 M^{-1}.	66
3.4	VARIABLE PATH-LENGTH MEASUREMENTS WITH BETA PI ATTACHMENT AT 488 NM.	70
3.5	THE SPECTRAL VOLUME SCATTERING FUNCTION $\beta(\theta)$ OVER THE ANGULAR RANGE 179 TO 180 DEGREES	73
4.1	SPHERICAL COMPONENTS OF VECTOR IRRADIANCE	83
4.2	VECTOR IRRADIANCE FROM ISOTROPIC SOUCE EMBEDDED IN A HOMOGENEOUS SCATTERING AND ABSORBING MEDIUM	87
4.3	VECTOR IRRADIANCE MEASUREMENTS FROM AN ISOTROPIC SOURCE TAKEN ON 26 AUGUST 1990, OFF THE COAST OF SOUTHERN CALIFORNIA	94
5.1	COORDINATE SYSTEM FOR THE MONTE CARLO MODEL THAT COMPUTES THE RADIANCE DISTRIBUTION DUE TO AN ISOTROPIC POINT SOURCE AT THE ORIGIN	102
5.2A	VOLUME SCATTERING FUNCTIONS FROM *PETZOLD* [1972] USED IN MONTE CARLO SIMULATIONS.	106
5.2B	SCATTERING PROBABILITY FUNCTIONS OF THE STATION 8 AND STATION 11 VSF'S.	107
5.3	ASYMPTOTIC AVERAGE COSINE FROM THE WILSON-HONEY [WILSON, 1972] AND *ZANEVELD* [1989] EQUATIONS COMPARED WITH $\bar{\mu}$ VALUES COMPUTED WITH THE *MOBLEY* [1994] EIGENMATRIX METHOD USING THE STATION 8 AND 11 VSF'S.	110
5.4	THE AVERAGE COSINE WITHIN ONE OPTICAL LENGTH OF A FINITE ISOTROPIC SOURCE WHERE THE RADIUS OF THE SOURCE IS ONE TENTH OF AN OPTICAL LENGTH	114
5.5	COMPARISONS OF THE MONTE CARLO RADIANCE DISTRIBUTIONS, OR PSF'S, AND THE MEASURED PSF'S AT LAKE PEND OREILLE DURING THE OPTICAL CLOSURE EXPERIMENT	118
5.6	COMPARISON OF PSF SLOPES FROM MEASUREMENTS AT LAKE PEND OREILLE WITH THE MONTE CARLO "COAST" RUNS.	120

LIST OF FIGURES (Continued)

Figure		Page
5.7	THE AVERAGE COSINE AS A FUNCTION OF OPTICAL PATH LENGTH FROM AN IPS COMPUTED FROM THE STATION 11 VSF SIMULATIONS	121
5.8	THE MEAN PATH-LENGTH INCREASE AS A FUNCTION OF OPTICAL PATH LENGTH FROM AN IPS COMPUTED FROM THE STATION 11 VSF SIMULATIONS	123
5.9	COMPARISON OF AVERAGE COSINES FROM MONTE CARLO SIMULATIONS AT 15 OPTICAL LENGTHS WITH ASYMPTOTIC AVERAGE COSINES FROM EIGENMATRIX COMPUTATIONS	125
5.10	COMPARISON OF NORMALIZED RADIANCE DISTRIBUTIONS FROM MONTE CARLO SIMULATIONS AT 15 OPTICAL LENGTHS WITH ASYMPTOTIC RADIANCE DISTRIBUTIONS FROM EIGENMATRIX COMPUTATIONS	126
5.11	DIFFERENCES IN THE MEAN LIGHT-PATH INCREASE FROM THE STATION 8 AND 11 VSF'S	129
6.1	GEOMETRY FOR ILLUSTRATING THE DEFINITIONS AND EQUIVALENCE OF THE BEAM SPREAD AND POINT SPREAD FUNCTIONS	140
6.2	EXPERIMENTAL SETUP FOR MEASURING THE COMPLETE BSF OF SEA ICE *IN SITU*	144
6.3	THE BSF AS A FUNCTION OF DEPTH IN FIRST-YEAR SEA ICE	145
6.4	RESULT OF FITTING A TYPICAL EXAMPLE OF THE BSF DATA TO A GAUSSIAN FUNCTION, EQ. 6.5	147
6.5	RESULT OF FITTING THE DATA IN FIGURE 6.4 TO A LORENTZIAN FUNCTION, EQ. 6.6	148
6.6	RESULT OF FITTING THE DATA IN FIGURE 6.3 TO A LORENTZIAN FUNCTION, REVEALING THAT THE WIDTHS OF THE BSF'S ARE ONLY WEAKLY AFFECTED BY ICE LAYERING	149
6.7	BSF AS A FUNCTION OF SEA ICE PATHLENGTH R	151
6.8	NORMALIZED LORENTZIAN FITS TO THE BSF DATA IN FIGURE 6.7, SHOWING THE CHANGE IN THE WIDTH OF THE BSF AS A FUNCTION OF ICE PATHLENGTH	152
6.9	LINEAR REGRESSION TO $\ln[\mathrm{BSF}(0,R)]$ FOR THE DATA IN FIGURE 6.7	153

LIST OF FIGURES (Continued)

Figure		Page
6.10	MEASUREMENT OF THE PSF OF OCEAN WATER, TAKEN IN MONTEREY BAY, CALIFORNIA.	154
6.11	BSF DATA FROM FIGURE 6.7 AND BEST FIT USING EQ. 6.6.	156
6.12	BSF DATA FROM FIGURE 6.7 AND THE ASYMPTOTIC RADIANCE DISTRIBUTION COMPUTED BY HYDROLIGHT USING THE VALUES OF *A* AND *C* FOUND FROM THE BEST FIT WITH EQ. 6.6 (SEE FIGURE 6.11).	160
6.13	SCATTERING PHASE FUNCTION ASYMMETRY PARAMETER *G*, AS A FUNCTION OF ω_0 FOR THREE VALUES OF K_∞/c.	161
6.14	ASYMMETRY PARAMETER G COMPUTED WITH EQ. 6.10 USING $G = 0.233$	163
6.15	COMPARISON OF COMPUTED ASYMPTOTIC RADIANCE DISTRIBUTION WITH THE MEASURED BSF FOR THE PATHLENGTH $R = 50$ cm	164

LIST OF TABLES

Table		Page
5.1	OPTICAL PARAMETERS FOR MONTE CARLO SIMULATIONS	104
5.2	COEFFICIENTS FOR $\bar{\mu}_\infty$ REGRESSION TO THE EQUATION (5.9)	109
5.3	COEFFICIENTS FOR $\bar{\mu}$ REGRESSION TO THE EQUATION (5.19)	122
5.4A	ESTIMATES OF ABSORPTION COEFFICIENTS AND ERRORS (*PETZOLD* [1972] STATION 8 VSF)	127
5.4B	ESTIMATES OF ABSORPTION COEFFICIENTS AND ERRORS (*PETZOLD* [1972] STATION 11 VSF)	127

DEDICATION

In memory of my brother Eddie

Who played on the mean streets of New York

And found they can be terribly unforgiving

You will be missed

Optical Backscattering and Embedded Source Techniques for Characterizing the Optical Properties of the Ocean

Chapter 1

1. INTRODUCTION

Optical oceanography, the study of how light interacts with the sea, has advanced impressively in the past few decades. Theoretical oceanic optics has probably achieved the greatest success. Since the publication of the first correct explanation of the color of the sea by Shuleikin in 1923, the application of radiative transfer theory to light propagation in the ocean has been extremely successful. Indeed, the forward problem, namely that of computing the radiance distribution given the inherent optical properties and boundary conditions, is considered solved. A recent comparison of several numerical models which solve the radiative transfer equation, showed that they all agreed to within the numerical precision of the computations [Mobley et al., 1993]. In essence, a form of closure has been achieved in oceanic numerical radiative transfer theory. Inverse problems, however, remain problematic.

Experimental optical oceanography has certainly had its share of successes too, although it has been mainly in the gathering of data on ocean optical properties rather than on the careful testing of theoretical developments. Preisendorfer, in his monumental treatise Hydrologic Optics [1976], wrote:

> As anticipated above, the denouement of this problem still stands at this late date in the history of the theory [of radiative transfer], and awaits a definitive answer from those who are the only ones who can definitively answer it: the experimenters. Theoretical reasoning ... can be carried only so far. There eventually comes a time in the construction of any physical theory when all the theorizing must momentarily stop, and the court of last appeal be faced: Nature herself.

Surprisingly, his statement is as true today as when it was written over 20 years ago. The theorizing and the development of ocean-optical models continues at a rapid pace, with scant empirical data for guidance or experimental testing of models.

Data gathering of ocean optical properties probably had its beginnings in the nineteenth century when two independent investigators, the Italian astronomer P. A. Secchi and the Russian naval officer O. E. Kotsebu, began to make what are now referred to as Secchi depth measurements. The discovery of the photoelectric effect and the invention of the photocell, and later the photodiode, in this century greatly advanced quantitative, observational oceanic optics. These new electronic detectors made it possible to directly measure submarine light-field quantities, such as irradiance and radiance. The important extensions to radiometry developed by Gershun [1936] revealed how net vertical and scalar irradiances are related to the absorption coefficient a and the diffuse attenuation coefficient K. Preisendorfer [1961] later made the distinction between inherent optical properties (IOP's), e.g. a, and apparent optical properties (AOP's), e.g. K. These developments represented important advances in connecting theory with observations.

Advances in light source technology allowed instruments to be constructed that could directly measure IOP's. Ideally, one would like to measure, as a function of wavelength λ, the two fundamental IOP's $a(\lambda)$ and the volume scattering function $\beta(\lambda,\psi)$, where ψ is the scattering angle. As Nature would have it, these are the two most difficult IOP's to measure directly. Undoubtably, the first directly measured IOP of ocean water was the beam attenuation coefficient c. Although straightforward in concept, even the measurement of c has its difficulties. To be sure, a wide variety of instruments and methods have been devised for measuring IOP's, and several are currently in routine use. But even to this day, the debate still rages on the proper calibration of IOP instruments, and many of the measurements reported in the literature have been called into question (a good, though dated review on this issue, regarding the measurement of $\beta(\psi)$, is given by Kullenberg [1974]). The measurement of radiometric quantities is, however, quite the opposite, as optical standards and calibration methods have been available for many years and are continually being improved.

Fundamental *and* urgent problems in optical oceanography are therefore in the two related areas of, 1) developing accurate instruments and methods for measuring ocean-optical properties, especially IOP's, and 2) conducting experiments that appropriately test theoretical developments. Without serious attention and advances in these two areas — given the rapid pace in the development of ocean-optical models — optical oceanography is in danger of flying too high on borrowed wings. It is the author's hope that this

thesis makes a contribution to these fundamental and urgent problems in optical oceanography. Chapters 2 and 3 primarly address the former area, namely the development of instruments and methods for accurately measuring IOP's, in this case the backward scattering coefficient and the volume scattering function at and near 180°. The latter area, namely conducting experiments that test theoretical developments in radiative transfer theory, is the subject of chapters 4, 5, and 6.

Chapter 2, "Instruments and methods for measuring the backward-scattering coefficient of ocean waters," presents a rigorous analysis of fixed-angle backscattering sensors and suggests a method for their calibration to be adopted as a standard which is partially traceable to an NIST optical standard. It is shown that the backward scattering coefficient b_b can be accurately determined with a properly designed fixed-angle backscattering sensor. A new multi-wavelength backscattering sensor was developed for this purpose and is described and analyzed in detail. It was designed to be accurate and robust, so that the routine measurement of b_b, so important to ocean remote sensing, is now possible.

Chapter 3, "*In-situ* characterization of optical backscattering and attenuation for lidar applications," follows on the heels of bi-static optical backscattering measurements to address the measurement of IOP's relevant to ocean lidar, namely $\beta(179 \text{ to } 180)$ and c. A unique instrument called Beta Pi, developed specifically for measuring these two optical parameters, is described and analyzed. It is shown that Beta Pi is the first and only in-water,

self-calibrating instrument for measuring IOP's. Beta Pi thus performs highly accurate measurements of $\beta(179 \text{ to } 180)$ and c. The concept of quasi-inherent optical properties (QOP's) is discussed in the context of lidar measurements. QOP's play the same role in lidar propagation models as IOP's do in radiative transfer models. However, the concept of QOP's deserves wider attention because, in general, any real IOP measurement actually yields a QOP. The goal is to understand how closely a QOP, which depends on the instrument's optical design, approximates the desired IOP.

Only a handful of investigators have pursued submerged source techniques for characterizing the optical properties of the ocean, including sea ice, and almost solely for the application of underwater imaging or lidar. It has not been generally appreciated that submerged source techniques offer a powerful means for characterizing the optical properties of the ocean and also for experimentally testing radiative transfer theory. Chapter 4, "Measurement of the spectral absorption coefficient in the ocean with an isotropic source," presents a derivation of a more general form of Gershun's famous equation [Gershun, 1936] that relates a, an IOP, to K, an AOP. It is shown that Gershun's equation is actually an asymptotic limit, as the distance from an isotroptic light source (ILS) goes to infinity, of the more general result derived in this chapter. As with Gershun's equation, the ILS solution can be solved for the absorption coefficient. The solution shows that the absorption coefficient can be measured exactly, with no scattering correction, from measurements of the scalar and plane irradiances due to an ILS.

Moreover, if measurements are made at two or more distances, no absolute calibration is required. Like Beta Pi, the method is self calibrating and yields accurate results with no modeling corrections.

Chapter 5, "The average cosine due to an isotropic light source in the ocean," further advances the work in Chapter 4. The problem of a finite size ILS is rigorously treated, and limiting values of the average cosine $\overline{\mu}_r$ due to an ILS are derived. The average cosine of the light field is fundamental to connecting IOP's to AOP's. For a submerged ILS, as opposed to solar illumination and plane-parallel geometry, simplifications result that allow the absorption coefficient to be determined accurately from plane irradiance measurements alone. The relatively controlled experimental conditions with the submerged ILS technique provides one of the most accurate optical-oceanographic setups for accurately testing aspects of radiative transfer theory. For example, in Chapter 5, the computations of a point source Monte Carlo model are compared with measured radiance distributions due to an ILS in the ocean. Such a comparison of a computer model with experimental data has never before been published.

Sea ice, which is, after all, ocean water in its frozen state, deserves attention in oceanic optics. It is important to understand solar propagation through sea ice to better model ice thermodynamics and primary production beneath and even within the ice. However, sea ice is a radically different optical medium than water and offers new challenges for experimentation and optical modeling. Chapter 6, "Theory and measurements of the complete

beam spread function of sea ice," describes a novel technique for measuring the complete beam spread function (BSF) within ice. Because sea ice is a highly scattering medium, it is shown that the measured BSF can be used to test predictions of asymptotic radiative transfer theory and photon diffusion theory. Connecting these two theories results in new relationships that, along with the BSF measurements, provide a nearly complete characterization of the optical properties of sea ice needed for light propagation modeling.

Chapter 2

INSTRUMENTS AND METHODS FOR MEASURING THE BACKWARD-SCATTERING COEFFICIENT OF OCEAN WATERS.

Robert A. Maffione and David R. Dana

1996, *Applied Optics* ,(to be submitted).

2.1 ABSTRACT

The backward-scattering coefficient, b_b, is an important optical property that plays a central role in studies of ocean-color remote sensing, suspended particle distributions, water clarity, and underwater visibility. In contrast to other ocean-optical properties, surprisingly little attention has been given to measuring b_b, although modeling it has been a focus of considerable research. Fixed-angle optical backscattering sensors were previously developed for application to ocean lidar and were calibrated to provide measurements of the volume scattering function (VSF) at a single backscattering angle. The fixed-angle backscattering-measurement approach is investigated for the application of measuring b_b. Analysis shows that the sensor response to volume scattering can be expressed as the integral of the VSF over the backward angles (90° to 180°) weighted by the sensor response function. A procedure is described for determining the sensor response function and it is shown that this function contains all the information necessary to fully calibrate the sensor to measure the VSF at a nominal backscattering angle. The backscattering angle, which can be computed using the sensor response function, is shown to depend mainly on the optical geometry of the sensor, but also weakly on the attenuation coefficient of the water. Building on the work of Oishi, it is found that, for fixed-angle backscattering sensors, b_b is probably most accurately estimated when the sensor response function covers the range of scattering angles from roughly 110° to 160°. In other words, instead of measuring the VSF at a discrete angle, the most accurate estimate of

b_b is obtained by measuring backscattering over the middle range of backscattering angles, where the shape of the VSF has the least variability. Analysis of published VSF's and the work of Oishi strongly suggest that measurements of the VSF at and near the extreme angles, that is 90° and 180°, will result in the largest errors in estimating b_b. Until more definitive empirical data on the shape of the VSF in the backward hemisphere are available, b_b is best estimated by $1.1 \times 2\pi\beta(110° - 160°)$, where $\beta(110° - 160°)$ denotes the calibrated measurement of the VSF using the procedure given here, and the sensor response function covers the scattering-angle range of roughly 110 - 160. The integral mean value theorem shows that, for the sensor optical geometries used in the present work, a discrete VSF measurement is obtained near the peak of the sensor response function, typically 135° to 145°, although the discrete scattering angle also depends weakly on the shape of the VSF.

2.2 INTRODUCTION

The backward scattering coefficient, b_b, is of fundamental importance to ocean-color remote sensing. Although spectral absorption by ocean water modifies the spectrum of the submarine light field, it is spectral backscattering, predominantly by suspended particles, that provides the remotely-sensed optical signal. The measured intensity of the light backscattered by the ocean, which is used to infer the concentration of ocean water constituents such as phytoplankton, is virtually useless without knowledge of b_b. Historically, a great deal of attention has been devoted to

developing instruments and methods for determining spectral absorption of ocean water and its individual constituents (see *Pegau et al.*, 1995, for a review of the many methods available). Ironically however, there has been a surprising lack of attention to directly measuring the backward scattering coefficient, particularly spectrally.

This paper describes instruments and methods for directly and routinely measuring backward light scattering by ocean water. These instruments and methods were developed over many years at SRI International, and this work is now continuing at Sequoia Scientific, Inc., by the authors. A unique calibration method, presented here, is used to convert the optical backscattering signal to a measurement of the volume scattering function (VSF) at a nominal angle between about 135° and 145°. The particular backscattering angle depends on the optical geometry of the instrument and, to a much lesser degree, the shape of the VSF in the backward hemisphere. Multiplying this measured VSF by a suitable conversion factor then converts the VSF to b_b. The shape of the VSF in the backward hemisphere, generally known from previous measurements by others [*Petzold*, 1972; *Kullenberg*, 1974], greatly constrains the values of the conversion factor so that the use of a constant value results in a likely standard error in b_b of approximately 10%. A previously published analysis by *Oishi* [1990] showed that the *maximum* likely error is about 17% of the estimated value of b_b using this method. Regardless of any error in the conversion to b_b, the measurement of the VSF at a nominal backward angle is shown to be highly accurate and is partially

traceable to an NIST standard. It is therefore recommended that the calibration method presented here be adopted as a standard protocol for measuring the VSF in the backward hemisphere, which should greatly aid in the comparison and interpretation of world-wide measurements.

2.3 BACKGROUND

2.3.1 History

Højerslev [1994] credits *Pettersson* [1934] with constructing the first *in-situ* optical backscattering sensor. Pettersson's instrument used an incandescent light bulb and two large-area photocells. The sensor did not incorporate spectral filters and was not calibrated to provide measurements in units of an optical property, such as the VSF at a nominal angle or b_b. But given the technology of the time, Pettersson's instrument was impressive and marks a milestone in the development of ocean-optical backscattering sensors.

General-angle scattering meters, sometimes referred to as nephelometers, began to be developed in the late 1950's and early 1960's for in-situ work. To the authors' knowledge, the first published paper on a submersible general-angle scattering meter was by *Tyler and Richardson* [1958]. Their instrument covered the angular range from 20° to 170° and was calibrated to give measurements in units of the VSF (m^{-1} sr^{-1}). In theory, a properly calibrated general-angle scattering meter is the most accurate way for determining b_b since it measures the VSF over a range of backscattering

angles. However, this type of instrument is notoriously difficult to calibrate accurately and is cumbersome and time-consuming to deploy. *Kullenberg* [1972] reviews the various submersible general-angle scattering meters and discusses some of the problems with their calibrations. The present work is concerned with fixed-angle optical-backscattering sensors and their calibration for determining the VSF at a nominal backscattering angle, as well as the backward scattering coefficient, spectrally.

The first fixed-angle backscattering sensors, designed and calibrated for measuring the VSF of ocean water, were developed at SRI International in the early 1980's [*Moore et al.*, 1984] under an Advanced Research Projects Agency (then DARPA) funded program called LIDEX, for LIght Detection EXperiment. These sensors used infrared light-emitting diodes (LED's) and high-frequency phase-synchronous photodetection. The major advantages in using an LED as the light source is its relatively low power consumption and ability to be modulated electronically at rapid rates. The drawback at that time was that only IR LED's were available that were bright enough for the application of measuring backscattering by ocean water. The original SRI backscattering sensors used visible-blocking filters and measured backscattering over the spectral bandwidth of the LED, centered at 880 nm. Figure 2.1 shows a schematic layout of this sensor.

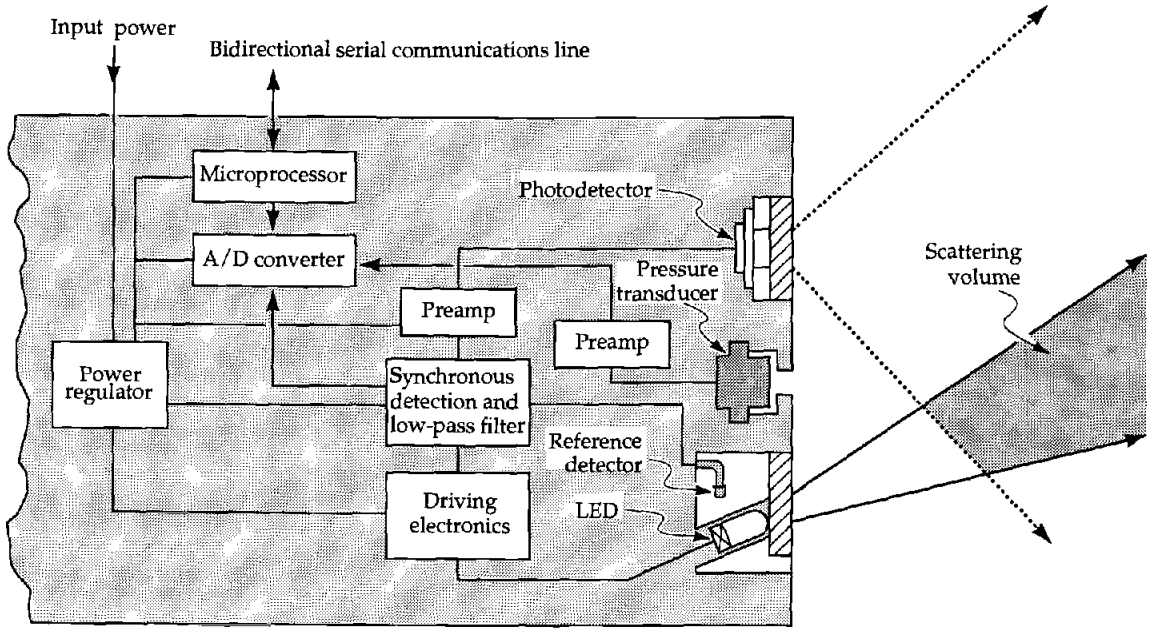

Figure 2.1 Schematic layout of the first optical backscattering sensor developed at SRI International in the early 1980's under an ARPA (then DARPA) program called LIDEX.

The absolute calibration was based on the sensor's response to a reflectance standard. This method involved measuring the response of the sensor to a Lambertian target as a function of range from the sensor. The resulting calibrated measurement provided an estimate of the VSF (m^{-1} sr^{-1}) at a nominal backscattering angle [*Moore et al.*, 1984]. A later, more thorough analysis of this calibration scheme showed that, for the original SRI sensor geometry, the backscattering angle was nominally 150° [*Maffione et al.*, 1991]. The analysis by Maffione et al. improved the accuracy of the calibration by taking into account geometrical factors that had previously been neglected.

It is possible to use other types of light sources at the expense of some of the advantages of LED's. In the late 1980's, the Johns Hopkins University

Applied Physics Laboratory (APL) developed a backscattering sensor using a bright incandescent lamp [*Smart et al.*, 1991]. The APL sensors incorporated spectral absorption filters centered at 490 nm and 532 nm., giving these sensors the distinction of being the first visible-wavelength, fixed-angle backscattering sensors. The optical geometry was designed to yield a measurement of the VSF at a centroid angle of 170°, which is desirable for lidar applications (although 170° is undesirable for estimating the backward scattering coefficient). APL used the same calibration method originally developed at SRI for the IR backscattering sensor, which did not take into account the attenuation of the water at visible wavelengths. As shown below, the variability in the attenution of ocean waters at visible wavelengths requires an attenuation correction to backscattering measurements at these wavelengths. This correction becomes more severe at larger backscattering angles, such as 170°, and as the attenuation of the water increases.

The next advance came in 1991 when the authors redesigned the optics and electronics of the SRI sensor to take advantage of visible-wavelength LED's. Figure 2.2 shows a schematic of this sensor, illustrating its more narrow optical geometry which resulted in a measurement of the VSF at a nominal angle of 135°. The lower backscattering angle was desired in order to more accurately estimate b_b from a single-angle VSF measurement (explained in detail below). The newly modified sensors were first deployed during the ONR ocean-optical closure experiment at Lake Pend Oreille, Idaho, in the spring of 1992. Only one visible wavelength, centered at 565 nm, was used in

the newly modified sensors because sufficiently bright LED's were not yet available at other visible wavelengths. When bright LED's at a variety of visible wavelengths became available, the authors developed a five-wavelength backscattering sensor which was incorporated into a remotely-operated vehicle [*Maffione et al.*, 1995]. This multi-wavelength sensor, dubbed The Slab, incorporated the same optical and electrical design as the single-wavelength visible sensor.

Recently, the authors completely redesigned both the optics and electronics of the 135° sensor, developing a compact four-wavelength backscattering sensor that could easily be used in a variety of ocean-deployable configurations. The new sensor, called the BB-4, incorporates a unique

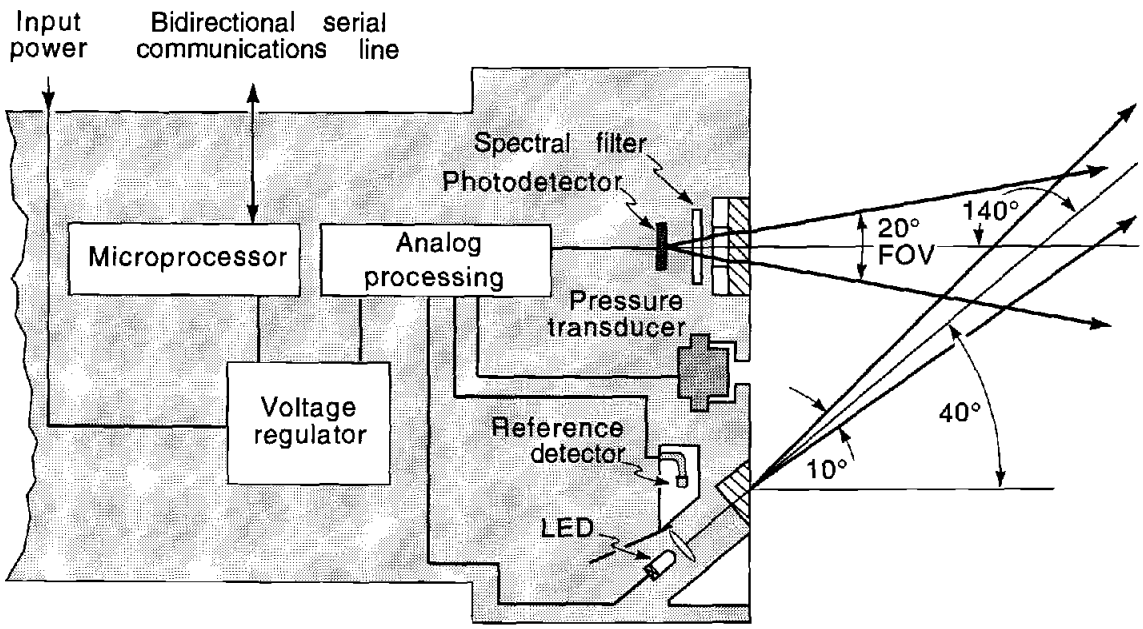

Figure 2.2 The second generation backscattering sensor developed at SRI in 1991. The major improvement was better collimating optics for application in the visible part of the spectrum.

electro-optical scheme that effectively cancels any ambient light signal. Thus, maximum signal gain can be used, even near the surface in bright sunlight. Narrow-band interference filters, appropriately matched within the broader spectral bands of the LED's, are used in the receiving optics to select the measurement wavelengths. It is shown below that the BB-4 measures the VSF at a nominal angle of 140°. A six-wavelength backscattering sensor, similar to the BB-4, called the Bscat-6, is currently being developed.

2.3.2 Notation and Definitions

The angular distribution of scattering by a small volume is described by the volume scattering function, $\beta(\psi)$, defined as the second partial derivative of the scattered flux, Φ, with respect to solid angle Ω and scattering volume V, normalized by the incident, collimated irradiance E, *viz*,

$$\beta(\psi) = \frac{\partial^2 \Phi(\psi)}{E \partial \Omega \partial V}, \tag{2.1}$$

where ψ is the polar scattering angle with respect to the collimation axis of the incident irradiance. Although not shown explicitly, $\beta(\psi)$ is a function of wavelength λ. In the ocean, $\beta(\psi)$ also varies with time and space but is usually denoted as a function of only the depth z.

Two useful optical properties can be derived from $\beta(\psi)$: the total scattering coefficient b and the backward scattering coefficent b_b. They are respectively defined by

$$b = \iint_{4\pi} \beta(\psi) d\Omega = 2\pi \int_0^{\pi} \beta(\psi) \sin\psi \, d\psi \tag{2.2}$$

and

$$b_b = 2\pi \int_{\pi/2}^{\pi} \beta(\psi) \sin\psi \, d\psi . \tag{2.3}$$

This latter optical property, b_b, finds its widest application in ocean remote sensing because it can be related in a simple, though approximate way to the amount of light that is backscattered, thus providing the light emerging from the sea. To first order, the irradiance reflectance and the remotely sensed reflectance of the oceans are directly proportional to b_b [*Gordon et al.*, 1988].

Another useful optical property is the volume absorption coefficient a. It too is a function of wavelength, space, and time. There are many methods in use for measuring a, or at least an approximation to it (for a review of these methods, see *Pegau et al.*, 1995). The sum of a and b gives c, the beam attenuation coefficient. Transmissometers, which directly measure beam attenuation, have been in routine use for many years.

As mentioned earlier, the backscattering measurement requires a correction due to the attenution of the beam over the total water pathlength from the source to the scattering volume and then to the receiver. Ideally then, it is desirable to measure the attenuation coefficient using a transmissometer with an optical design that matches the backscattering sensor. It will be shown, however, that the attenuation correction is insensitive to changes in beam optics, at least for the backscattering sensors

developed by the authors, because the total pathlength is so short. Therefore the attenuation correction can be accurately performed with measurements from any type of transmissometer provided the wavelengths are properly matched.

2.4 GENERAL ANALYSIS OF BACKSCATTERING SENSORS

A general analysis of a generic optical-backscattering sensor is developed here with two contraints: the faceplate of the sensor is assumed to be flat and the optical geometry is fixed — in other words, it is a fixed-angle sensor. The term "backscattering" implies that the sensor measures light scattered through angles greater than 90°, i.e., the backward hemisphere. It is, of course, possible to construct a backscattering sensor with a faceplate that is not flat; for example it could be concave, such as in the design of some free-angle nephelometers [*Jerlov*, 1976]. To the authors' knowledge, no fixed-angle backscattering sensors have been built that do not have a flat faceplate. Nonetheless, the analysis presented here can easily be extended to include non-flat faceplate designs should such sensors ever be built. Calibrating such sensors, using the method described in this paper, could be quite complicated however. Unless there is a compelling need for a non-flat faceplate, it is highly recommended that furture backscattering sensor designs incorporate a flat faceplate to allow for their accurate calibration.

Figure 2.3 shows a schematic of the general optical geometry for a backscattering sensor. The fixed geometrical parameters, which define the optical design of the sensor, are

H = distance between optical axes of source and detector;

θ_{0s} = in-water (i.e., refracted) angle of source optical axis;

θ_{0d} = in-water angle of detector optical axis;

α_s = full-width half-maximum (FWHM) divergence angle of source;

α_d = FWHM field-of-view (FOV) of detector.

Distinct from the fixed parameters are the geometrical variables, defined by

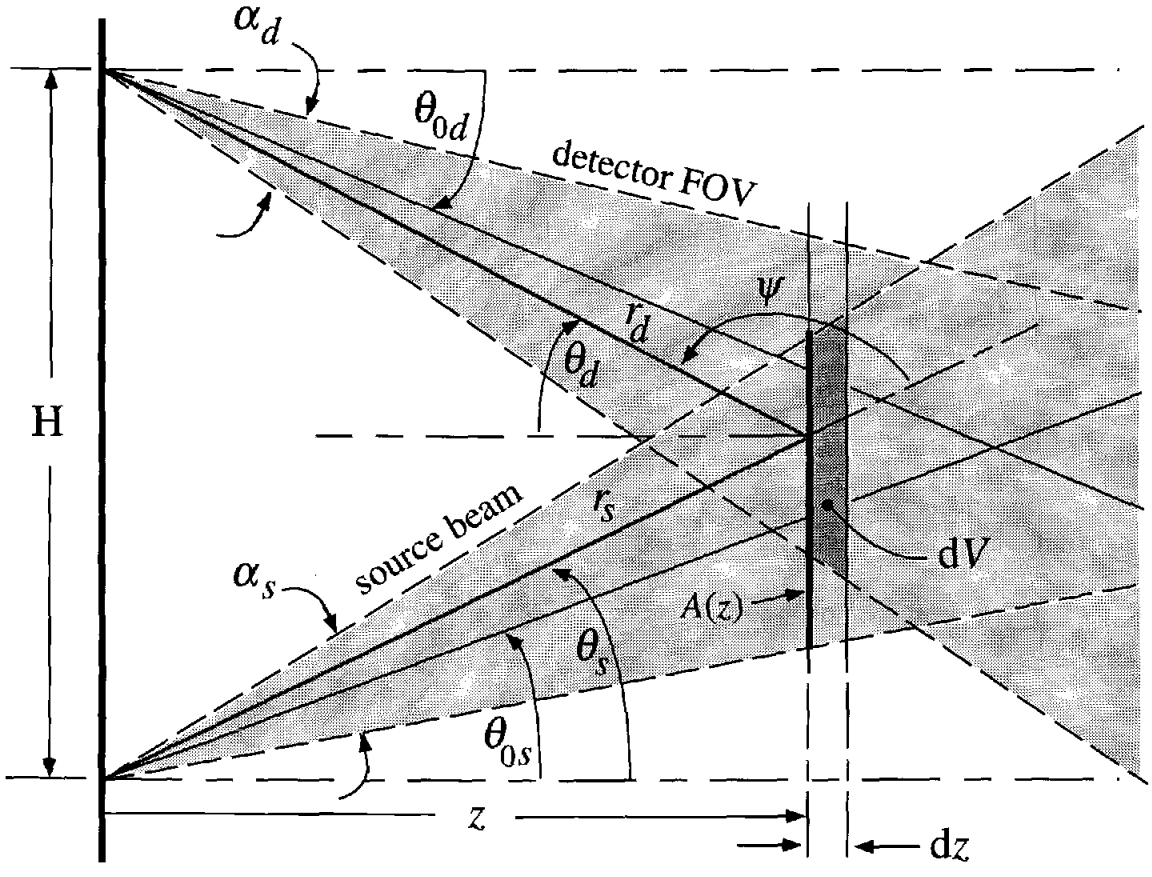

Figure 2.3 Optical geometry for a generic fixed-angle backscattering sensor.

Figure 2.3 as

z = linear distance perpendicular to faceplate;

r_s = water-path distance from source to infinitesimal scattering volume;

r_d = water-path distance from scattering volume to detector;

θ_s = centerline angle of that portion of the source beam which illuminates the scattering volume dV;

θ_d = centerline angle of that portion of the detector FOV which subtends the intersecting scattering volume dV;

ψ = scattering angle.

Note that the latter five variables can all be considered dependent variables of z. The dependent variable functions are all simple geometrical relationships involving the fixed parameters.

In general, the source beam will have a finite area where it enters the water at the pressure window, not shown in Figure 2.3. Likewise, the detector FOV has a finite area of acceptance at the water side of the window. These are omitted for simplicity and clarity in the presentation of the analysis but are easily taken into account by moving the origin of z, the axis perpendicular to the faceplate, further to the right in Figure 2.3. Simple trigonometry can then be used to correct the optical pathlengths r_s and r_d. If the areas are relatively small, it is an excellent approximation to simply assume that the source and detector cones converge to a point at the window in the manner illustrated in Figure 2.3.

The scattering volume, $dV \equiv \Delta A\, dz/\cos\theta_s$, is defined by the intersection of the source beam and FOV of the detector, and is a function of the distance z. This is illustrated by the darker shaded region in Figure 2.3. $\Delta A(z)$ is the area perpendicular to the z axis subtended by dV at the detector. Also note that the pathlengths r_s and r_d intersect at the center of dV, so that the angles that r_s and r_d make with the optical axis are likewise a function of z. At a certain distance, denoted by, say z_{mid}, the lines r_s and r_d will coincide with the source beam and detector optical axes, respectively. The scattering angle at z_{mid}, denoted ψ_{mid}, is not, however, the scattering angle at the peak response of the sensor, nor is it the centroid scattering angle. This will be made clear below.

Let Φ_0 denote the radiant flux emitted into the water by the source beam. If $A(z)$ is the total area illuminated by the beam perpendicular to the z axis, then the flux $\Delta\Phi_{dV}(z)$ incident on dV is

$$\Delta\Phi_{dV}(z) = \Phi_0 \exp(-c r_s)\Delta A(z)/A(z).$$

The irradiance E incident on dV is therefore

$$\begin{aligned} E(z) &= \frac{\Delta\Phi_{dV}(z)}{\Delta A(z)} \\ &= \Phi_0 \exp(-c r_s)/A(z). \end{aligned}$$

By the definition of the VSF, Eq. 2.1, the flux scattered into the solid angle $\Delta\Omega$, which is determined by the FOV of the detector, is given by

$$\begin{aligned} \Delta\Phi(\psi, z) &= \beta(\psi) E(z)\, \Delta\Omega(z)\, \Delta V(z) \\ &= \beta(\psi)\left[\Phi_0 \exp(-c r_s)/A(z)\right]\left[\Delta A(z)\cos\theta_d / r_d^2\right]\left[\Delta A(z)\, dz/\cos\theta_s\right] \\ &= \beta(\psi)\Phi_0\left(\cos\theta_d/\cos\theta_s\right)\left[\exp(-c r_s)/r_d^2\right]\left[\Delta A^2(z)/A(z)\right]dz, \end{aligned} \qquad (2.4)$$

where infinitesimal dependent variables are replaced by their corresponding real, finite quantities. In the second line of Eq. 2.4, the last two bracketed quantities are $\Delta\Omega(z)$ and $\Delta V(z)$, respectively, as obtained from the geometry. The expression for $\Delta\Omega(z)$ assumes no vignetting at the detector, which is always true for the small optical pathlengths involved with the types of backscattering sensors considered here. The scattered flux arriving at the detector's pressure window is then

$$\begin{aligned}\Delta\Phi_\beta(\psi,z) &= \Delta\Phi(\psi,z)\exp(-c\,r_d) \\ &= \beta(\psi)\Phi_0(\cos\theta_d/\cos\theta_s)\left\{\exp\left[-c(r_s+r_d)\right]/r_d^2\right\}\left[\Delta A^2(z)/A(z)\right]dz \\ &= \beta(\psi)\Phi_0 W(z;c)dz,\end{aligned} \tag{2.5}$$

where

$$W(z;c) \equiv (\cos\theta_d/\cos\theta_s)\left\{\exp\left[-c(r_s+r_d)\right]/r_d^2\right\}\left[\Delta A^2(z)/A(z)\right] \tag{2.6}$$

is defined as the sensor-response weighting function to scattering. The dependence of $W(z; c)$ on the parameter c is explicitly denoted to distinguish the weighting functions that result from waters with different attenuation coefficients. It should be noted that c is not the "true" beam attenuation coefficient, but here represents the attenuation coefficient for the backscattering sensor's source beam. As shown below, $W(z; c)$ is a relatively weak function of c so that even rough measurements of c are adequate for an accurate attenuation correction — which depends on $W(z; c)$.

Integration of Eq. 2.5 over all z from 0 to ∞ gives the total flux scattered into $\Delta\Omega(z)$ arriving at the detector window. The response of the detector will be proportional to this flux, as well as to an electronic gain factor. For

calibration purposes, the detection electronics are usually designed to incorporate variable gain settings. Let the gain-factor setting for the detection of volume scattering be denoted g_β. This gain factor can be thought of as incorporating all electronic and optical conversion factors such as detector efficiencies and losses through the optical train. Then the detection signal, denoted Φ_β, is given by

$$\begin{aligned} \Phi_\beta &= \Phi_0 g_\beta \int_0^\infty \beta(\psi) W(z;c) dz \\ &= \Phi_0 g_\beta \beta(\psi^*) \int_0^\infty W(z;c) dz. \end{aligned} \tag{2.7}$$

The last step is justified by the integral mean value theorem, i.e., ψ^* takes whatever value, within the limits of integration, that gives the equality in Eq. 2.7. As mentioned above, the scattering angle ψ is implicitly a function of z. The value of ψ^* depends both on $W(z; c)$ and the shape of the VSF. However, as will be shown, ψ^* is determined primarily by $W(z; c)$. The units of Φ_β are not relevant because the calibration, described below, involves a ratio of two measurements that cancels radiometric units. In other words, g_β does not need to incorporate a quantum-electronic conversion factor to convert the electronic signal to absolute radiometric units, such as watts.

The calibration method involves measuring the in-water response of the sensor to a Lambertian target as a function of z. Figure 2.4 illustrates the geometry with a Lambertian target at a distance z. The response of the sensor is similar to Eq. 2.6, but the volume scattering function is replaced by a surface scattering function, ρ/π, where ρ is the diffuse reflectivity of the Lambertian

target. Because the target is Lambertian, the surface scattering function is independent of scattering angle. Similar to the derivation for the response of the sensor to volume scattering, the surface scattering response, denoted $\Delta\Phi_\rho(z)$, to a Lambertian target at a distance z is found to be

$$\begin{aligned}\Delta\Phi_\rho(z) &= \Phi_0\, g_\rho(\rho/\pi)\cos^2\theta_d\left\{\exp\left[-c_w(r_s+r_d)\right]/r_d^2\right\}\left[\Delta A^2(z)/A(z)\right] \\ &= \Phi_0\, g_\rho(\rho/\pi)(\cos\theta_s\cos\theta_d)W(z;c_w)\end{aligned} \tag{2.8}$$

In this case the beam attenuation coefficient is denoted c_w to distinguish it from c in Eq. 2.7, which is the attenuation coefficient of the (ocean) water

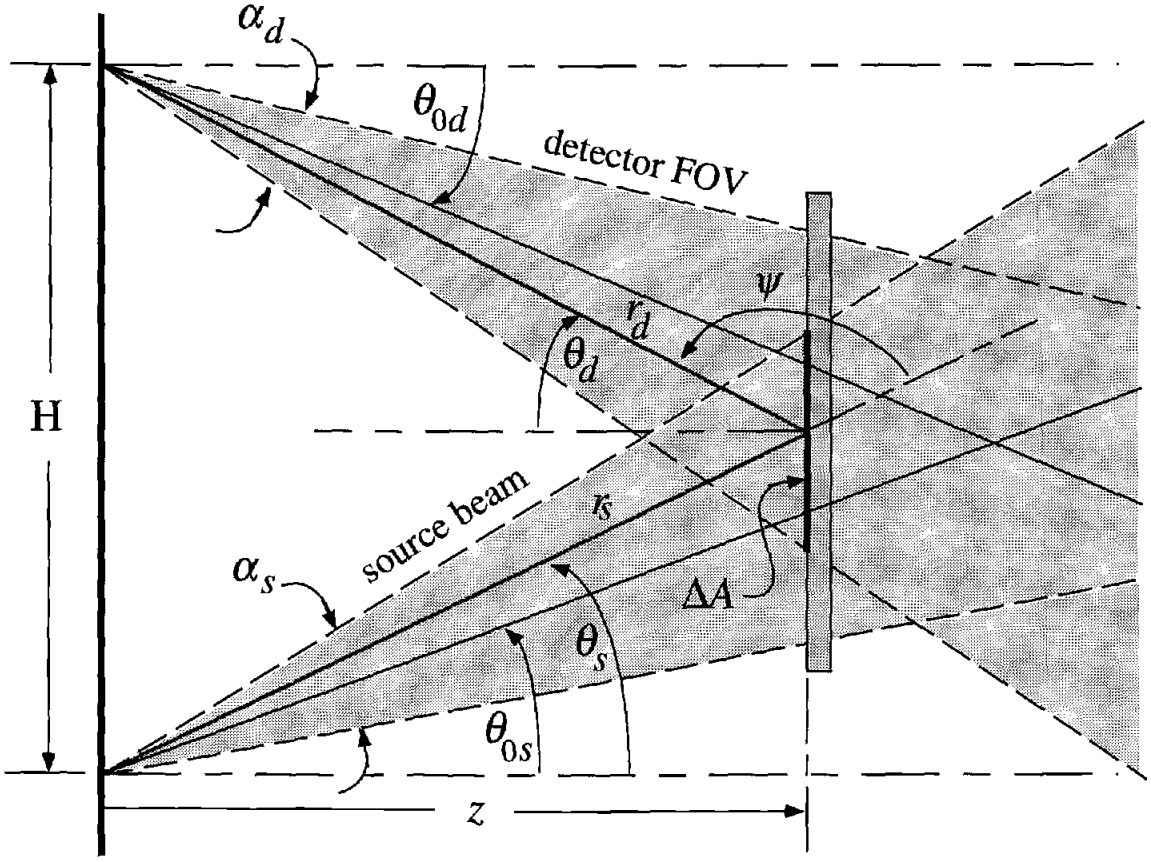

Figure 2.4 Optical geometry for analyzing the sensor response to a Lambertian target.

whose backscattering is being measured. $\Delta\Phi_\rho(z)$ is assumed to be measured in clear filtered water so that the target surface scattering greatly dominates the water volume scattering. The important difference between Eqs. 2.8 and 2.5 is the cosine factors. The $\cos\theta_s$ factor is missing in the denominator of Eq. 2.8 because there is no $dV \equiv \Delta A\, dz/\cos\theta_s$ since Eq. 2.8 deals with surface scattering. The additional $\cos\theta_d$ factor arises because the *intensity* of the scattered light from a plane Lambertian source varies as the cosine of the angle from the surface-normal direction. It is important to distinguish this from the *radiance* emitted by a Lambertian source, which is constant with direction. Multiplying Eq. 2.8 through by $dz/\cos\theta_s\cos\theta_d$ and integrating yields

$$\begin{aligned}\Phi_\rho &= \int_0^\infty \frac{\Delta\Phi_\rho(z)}{\cos\theta_s\cos\theta_d}dz \\ &= \Phi_0 g_\rho(\rho/\pi)\int_0^\infty W(z;c_w)dz\end{aligned} \tag{2.9}$$

Taking the ratio of Eqs. 2.7 and 2.9, and solving for $\beta(\psi^*)$ gives

$$\begin{aligned}\beta(\psi^*) &= \frac{\Phi_\beta}{g_\beta}\left(\frac{\rho}{\pi}\frac{g_\rho}{\Phi_\rho}\right)\frac{\int_0^\infty W(z;c_w)}{\int_0^\infty W(z;c)} \\ &= \frac{\Phi_\beta}{g_\beta}\mu\sigma(c,c_w),\end{aligned} \tag{2.10}$$

where

$$\mu \equiv \frac{\rho}{\pi}\frac{g_\rho}{\Phi_\rho} \tag{2.11}$$

and

$$\sigma(c,c_w) \equiv \frac{\int_0^\infty W(z;c_w)}{\int_0^\infty W(z;c)}. \tag{2.12}$$

Thus the direct backscattering measurement, Φ_β, is converted to $\beta(\psi^*)$ by normalizing Φ_β by the electronic gain factor g_β — which is set at the time of the measurement — and multiplying by the calibration constant μ and the attenuation correction factor $\sigma(c,c_w)$. Since Eq. 2.10 involves the ratio of the two gain factors, g_β and g_ρ, they only need to be known relative to each other. In other words, it is not necessary to know the various electronic and optical conversion factors implicitly incorporated into g_β and g_ρ. This scheme greatly improves the accuracy in the measurement of $\beta(\psi^*)$ over other calibration methods which require absolute values of various difficult-to-determine calibration factors.

The constant calibration factor μ is determined by measuring the response of the sensor, usually in a laboratory tank containing filtered water, to a Lambertian target as a function of range z. This measurement yields $\Delta\Phi_\rho(z)$ as given by Eq. 2.8. Integration of $\Delta\Phi_\rho(z)/\cos\theta_s\cos\theta_d$ then gives Φ_ρ, as in Eq. 2.9. The cosine factors $\cos\theta_s\cos\theta_d$, needed in the integration of $\Delta\Phi_\rho(z)$, can easily be computed from the geometry in Figure 2.4. Spectralon™ is recommended as the Lambertian target because its reflectivity is known to high accuracy and does not change in water when its surface is properly wetted.

The weighting function $W(z;c_w)$ is fundamental to the characterization and calibration of backscattering sensors. In theory, $W(z;c_w)$ could be calculated from first principles, but this would be extremely cumbersome because accurate analytic expressions are required for the cross-sectional profile of the beam and detector FOV. A better, and almost certainly more accurate way to determine $W(z;c_w)$ is to measure it in some fashion. This is essentially done through the measurement of $\Delta\Phi_\rho(z)$. Dividing Eq. 2.8 through by $\cos\theta_s \cos\theta_d \exp\left[-c_w(r_s+r_d)\right]/r_d^2$ gives

$$\begin{aligned}\Delta\Phi_\rho(z)\left\{r_d^2 \exp\left[c_w(r_s+r_d)\right]/\cos\theta_s\cos\theta_d\right\} &= k\left[\Delta A^2(z)/A(z)\right] \\ &\equiv kG(z),\end{aligned} \tag{2.13}$$

where $k \equiv \Phi_0 g_\rho(\rho/\pi)$ is a constant and

$$G(z) \equiv \Delta A^2(z)/A(z) \tag{2.14}$$

is strictly a function of the optical geometry of the sensor. Like $\cos\theta_s\cos\theta_d$, the factor $\exp\left[-c_w(r_s+r_d)\right]/r_d^2$ can easily be calculated from the geometry in Figure 2.4, given (or assuming) c_w of the water in which $\Delta\Phi_\rho(z)$ is measured is known. The constant k does not need to be known because only the relative shape of $W(z;c_w)$ is needed. For example, the computation of $\sigma(c,c_w)$, given by Eq. 2.12, involves the ratio of $W(z;c_w)$ and $W(z;c)$, thus cancelling k. Once G(z) is computed using Eq. 2.13, $W(z;c)$ can be computed for any value of c.

2.5 DESCRIPTION AND ANALYSIS OF PARTICULAR BACKSCATTERING SENSORS

2.5.1 Optical Design of the BB-4

As previously noted, the fixed-angle backscattering sensors originally developed at SRI went through several developmental stages. The basic geometry of the first SRI sensor, developed on the LIDEX program, is shown in Figure 2.1. The next generation of backscattering sensors, developed in 1991 by the authors, was designed to operate in the visible region of the spectrum and to measure backscattering for the purpose of estimating b_b. A schematic of this sensor is shown in Figure 2.2.

The basic optical design of the third generation backscattering sensor, the BB-4, is shown in Figure 2.5. One new feature is the collimating optics for the LED. Although LED's are designed to emit semi-collimated light, the collimation is typically much broader than the manufacturer's specifications, and the cross-section of the beam is highly non-uniform. The simpliest correction is to place a pinhole in front of the LED at the focal plane of a collimating lens. This solution, however, greatly reduces beam throughput. A standard technique to increase throughput is to first collect the light with a condenser lens which creates a real image of the LED at the focal plane of a second, collimating lens. If the LED is placed behind the focal plane of the condenser lens, the real image of the LED will be smaller than its actual extent. A pinhole could then be placed at the location of the real image,

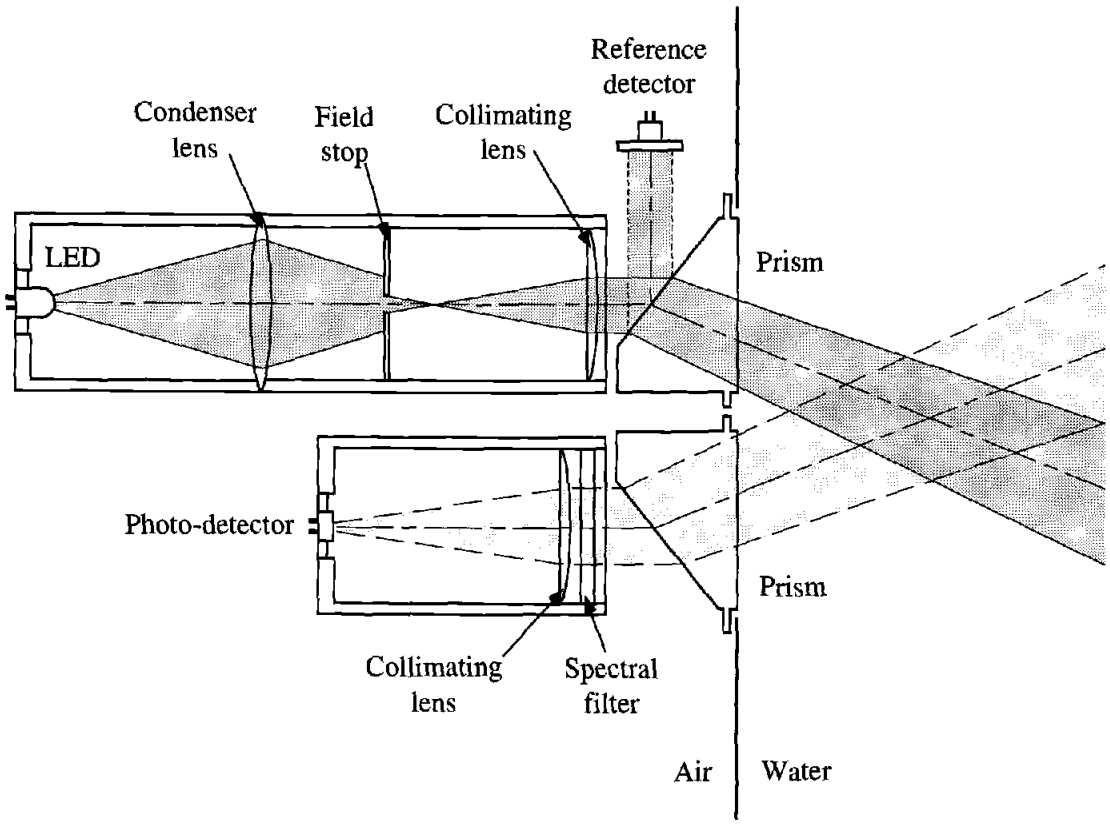

Figure 2.5 Schematic of the backscattering-sensor optics of the BB-4.

resulting in greater throughput as compared with placing a pinhole directly in front of the source.

Optica™, a ray tracing program that runs under Mathematica™, was used for the initial development of the optical design of the BB-4. Studies using Optica™ suggested that better stability and beam uniformity could be achieved by placing the field stop for the source behind the focal plane of the collimating lens. There are two reasons for this. First, a larger aperture can be used, reducing any output variations in the beam due to mechanical flexing. Second, LED's have highly irregular intrinsic collimation, and it turns out that a field stop behind the focal plane of the collimating lens better stops

aberrant rays. The precise optimal position for, and diameter of the field stop was then found through trial and error with the actual optical components and turned out to be in close agreement with the ray tracing results.

2.5.2 Calibration Analysis

2.5.2.1 Authors' Backscattering Sensors

The in-water response of the backscattering sensors to a Lambertian target was measured using a motor-drive system which moves the target in a continuous fashion and digitally records its distance, simultaneous with the backscattering measurement, with an optical encoder. The tank water was filtered with a series of filters from 2 μm down to 0.2 μm pore diameter. From the measured response function $\Delta\Phi_p(z)$, expressed by Eq. 2.8, the corresponding weighting function, $W(z;c_w)$ as given by Eq. 2.6, was computed using the method described above.

Examples of $W(z;c_w)$ for all three generations of backscattering sensors are shown in Figure 2.6. The curves in this figure clearly illustrate the evolution in the optical design of the backscattering sensors. For example, the first generation sensor used no collimating optics and thus has the broad weighting function shown in Figure 2.6. The second generation sensor, which incorporates crude collimating optics, has a more narrow weighting function. Finally, the third generation sensor, the BB-4, which is designed with more-highly collimating optics, yields the most narrow weighting function.

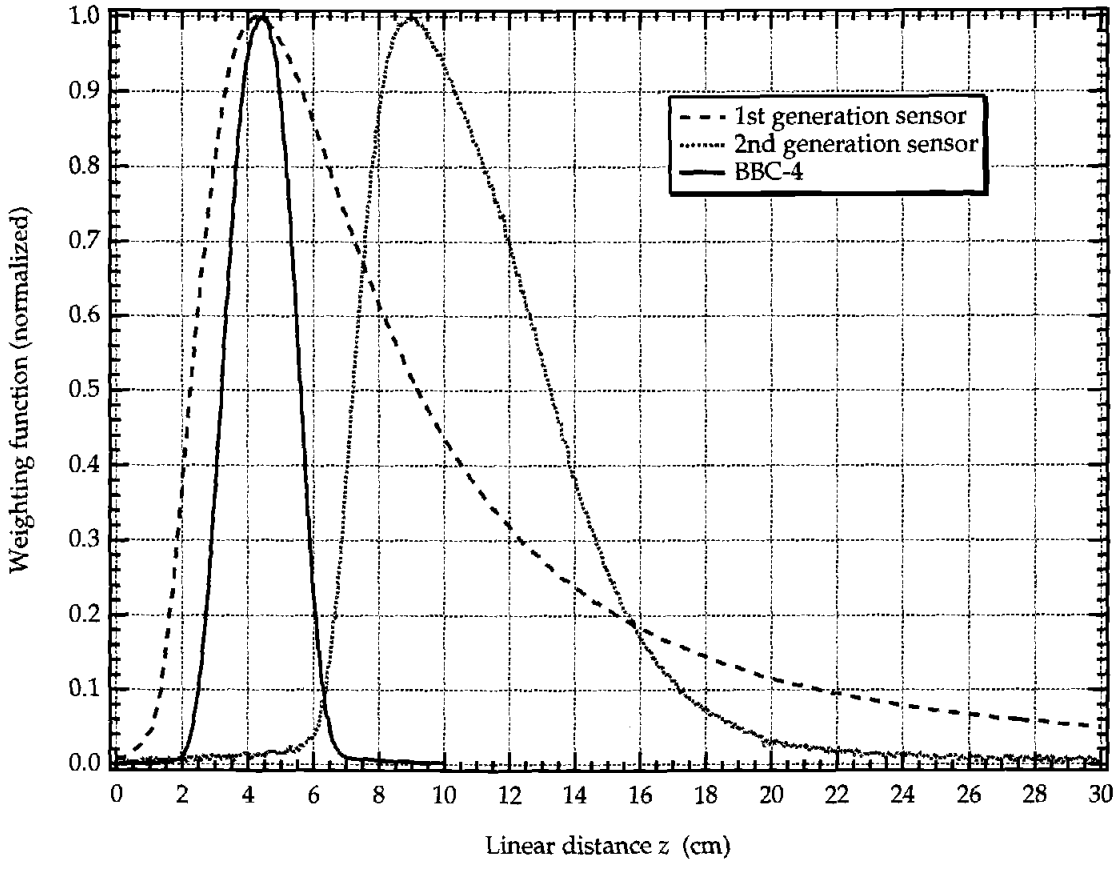

Figure 2.6 Weighting functions of three backscattering sensors with different optical geometries. The most narrow curve (solid line), from the BB-4, illustrates the result of highly collimating optics.

Recall Eq. 2.7, which shows that the detected scattered light is given by the integral of $\beta(\psi)$ weighted by $W(z;c)$. A perfect sensor with infinitesimal divergence angles would yield a delta function for $W(z;c)$, in which case $\beta(\psi)$ would be picked out at a discrete scattering angle given by the complement of the crossing angle of the (perfect) beam and receiver FOV. All real sensors must yield a $W(z;c)$ with a finite width, although the higher the collimation of the sensor optics, the smaller the width of $W(z;c)$, as shown above. In this case, the value of $\beta(\psi)$ that results from the calibrated measurement will

depend on the shapes of both $W(z;c)$ and $\beta(\psi)$ over the limits of integration, as required by the integral mean value theorem. Sensor-response weighting functions tend to look like skewed bell curves, as shown in Figure 2.6, whereas the shape of $\beta(\psi)$ in the backward hemisphere is generally a very gradual "U" shape, with a minimum somewhere between 100° and 140°. It should be expected then, that the value of $\beta(\psi)$, or $\beta(\psi^*)$, that is picked out will tend to be near $\psi^*(z = z_{peak})$, where z_{peak} is the distance z at which the peak of $W(z;c)$ occurs.

Figure 2.7 illustrates these comments with a BB-4 weighting function and a scattering phase function created by averaging the VSF measurements reported by *Petzold* [1972], which is probably indicative of the shapes of most, if not all, real ocean-water phase functions. The phase function shown in Figure 2.7 was normalized by b_b, not b, so that its solid angle integration from 90 to 180 is unity. Both $W(z;c)$ and $\beta(\psi)$ are plotted as functions of ψ over the range z from about 1 to 10 cm (as shown in Figure 2.6, there is no sensor response below 1 cm or above 10 cm). Clearly, the multiplication of these two functions will yield a curve that still looks very much like $W(z;c)$, so that the value of ψ^* is almost entirely determined by $W(z;c)$. Figure 2.8 shows $\beta[\psi(z)]W[\psi(z);c]$, which looks almost exactly like $W(z;c)$ in Figure 2.7. It is therefore an excellent approximation to assume that ψ^* is given by $\psi^* = \psi(z^*)$, where

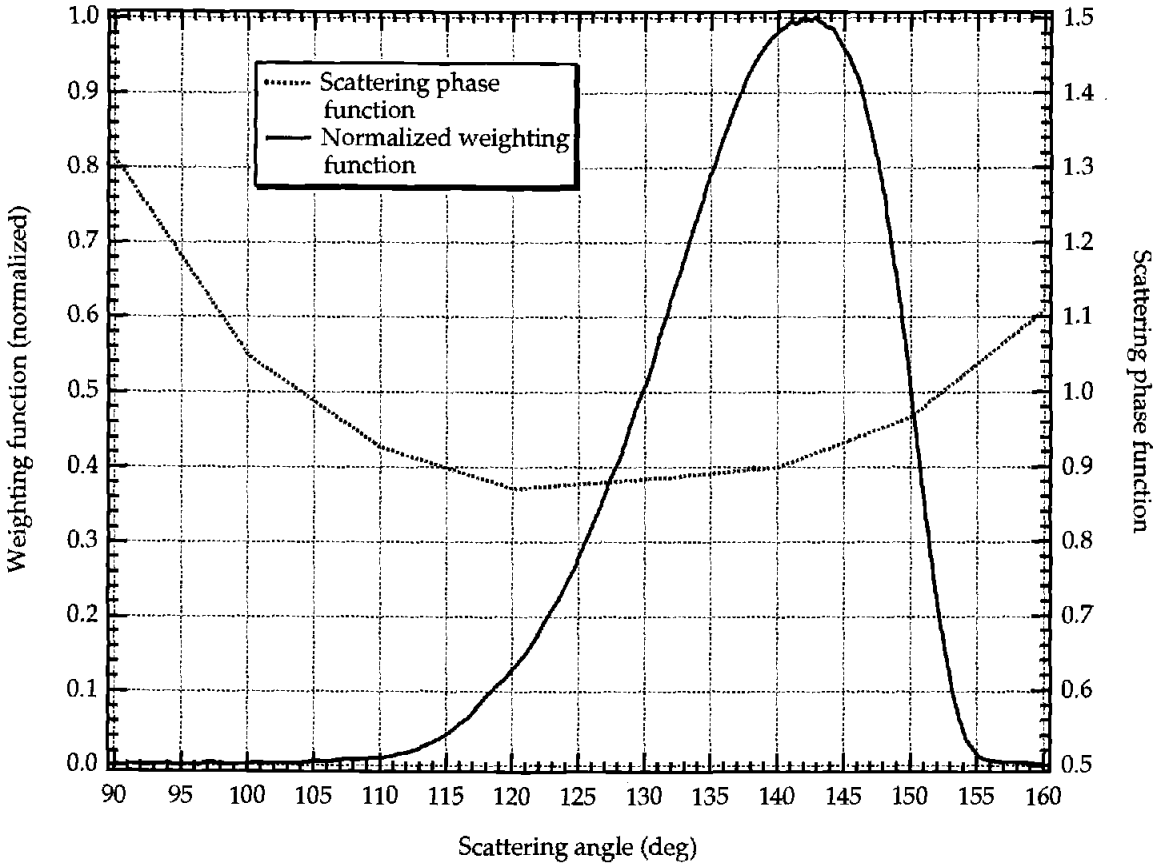

Figure 2.7 $W(z;c)$ for the BB-4 and Petzold averge phase function plotted as a function of the scattering angle

$$z^* \equiv \frac{\int_0^\infty zW(z;c)dz}{\int_0^\infty W(z;c)dz} \tag{2.15}$$

is defined as the centroid of $W(z;c)$. If $W(z;c)$ is a symmetric function (such as a Gaussian), then $z^* = z_{peak}$. For the BB-4 weighting function, $z^* = 4.21$ cm and $z_{peak} = 4.30$ cm. These correspond to scattering angles $\psi(z^*) = 141.2°$ and $\psi(z_{peak}) = 142.0°$. Numerically computing ψ^* by finding that value of ψ for which

$$\beta(\psi^*) = \frac{\int_0^\infty \beta[\psi(z)]W(z;c)dz}{\int_0^\infty W(z;c)dz}, \tag{2.16}$$

gave $\psi^* = 141.3°$ when the Petzold average phase function was used. This value differs insignificantly from $\psi(z^*)$, demonstrating that Eq. 2.15, which is independent of $\beta(\psi)$, is an excellent way of computing ψ^*. It is recommended that ψ^* be computed in this manner for all backscattering sensors and reported along with their backscattering measurements.

There remains the question of the dependence of $W(z;c)$ on the

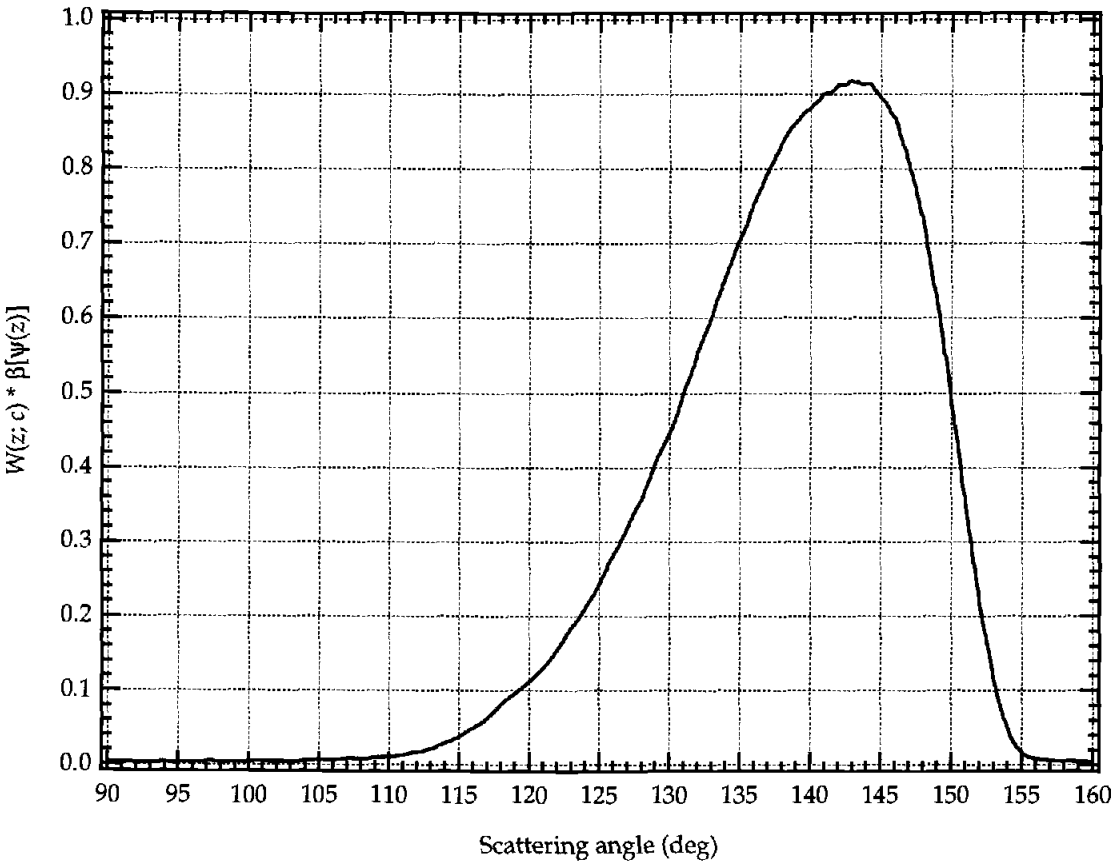

Figure 2.8 $W[\psi(z);c_w]\beta[\psi(z)]$ as computed from the two curves in Figure 2.7.

parameter c, which could in turn affect z^* or ψ^* since they are implicit functions of c by virtue of Eqs. 2.15 and 2.16, respectively. $W(z;c)$ given by Eq. 2.6 can be expressed in the form

$$W(z;c) \equiv \exp\left[-c(r_s + r_d)\right]\left[\frac{G(z)\cos\theta_d}{r_d^2 \cos\theta_s}\right]$$

where G(z) is given by Eq. 2.14. The dependence of $W(z;c)$ on c is therefore seen to be only a function of the factor $\exp(-cr) = \exp(-\tau)$, where $r \equiv r_s + r_d$ and $\tau \equiv cr$. For the BB-4, r ranges from about 4 to 15 cm in the non-zero region of $W(z;c)$. If c is on the order of, for example, 0.1 m^{-1}, then τ ranges from 0.004 to 0.015, and $\exp(-\tau)$ changes in an approximate linear fashion from about 1.00 to 0.98. If c is on the order of 1 m^{-1}, then τ ranges from 0.04 to 0.15, and $\exp(-\tau)$ again changes in a linear fashion from 0.96 to 0.86. So $W(z;c)$ is not expected to be a strong function of c for the BB-4 optical geometry.

Figure 2.9 shows $W(z;c)$ for three different values of c. The three $W(z;c)$'s were normalized to unity to better illustrate the effect on the shapes of the curves and their centroid values, which is relevant to ψ^*. Although all three curves are approximately the same shape, there is a small but noticable shift along the z axis, which corresponds to a shift in ψ^*. The shift in ψ^* is not large: a change in c by a factor of 25, from 0.02 to 0.50 m^{-1}, changed ψ^* by only 7°, from 141° to 134°. Nonetheless, this effect should be kept in mind, especially for measurements in coastal waters where drastic spatial variability

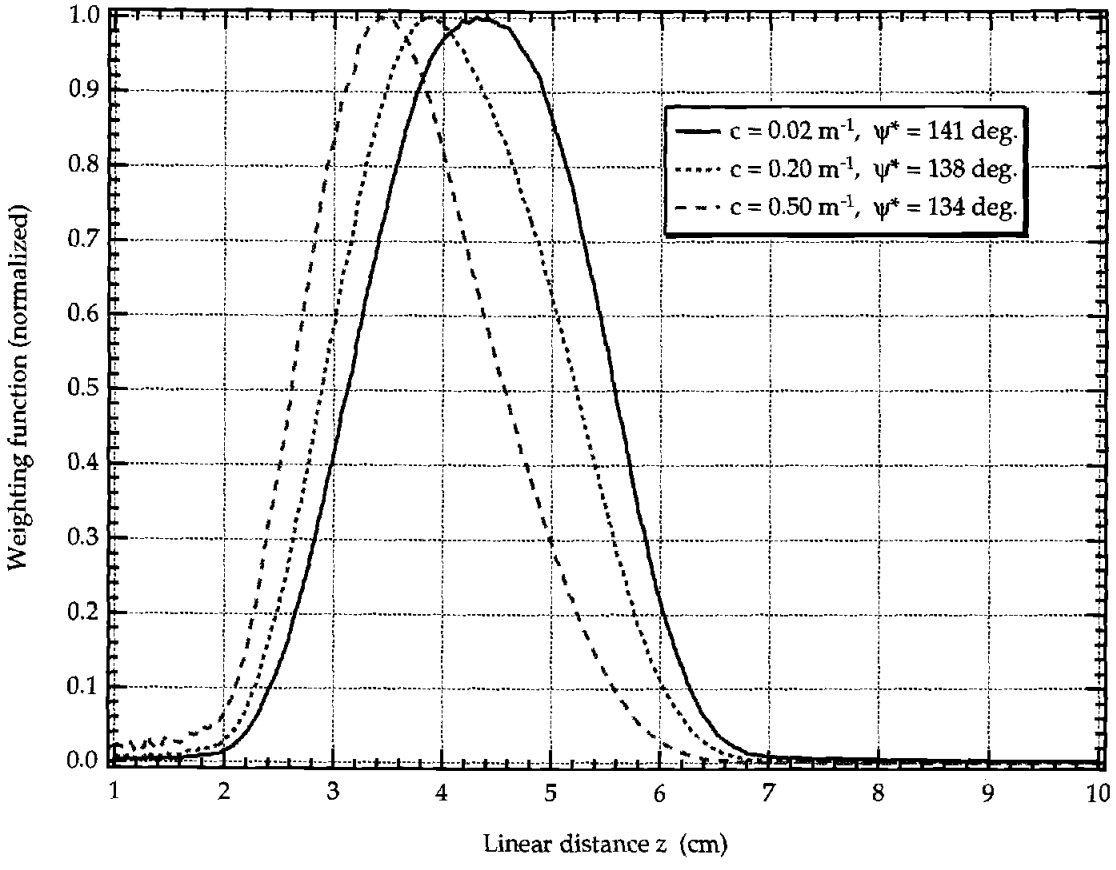

Figure 2.9 $W(z;c)$ for three values of c. An increase in c by a factor of 25 changed ψ^* by 7°.

in optical properties is often found. Moreover, this effect can be much greater for backscattering sensors with longer pathlengths or wider optical geometries. Also, as explained in Section 2.5.3, this effect may be significant for general-angle scattering meters, which are designed to characterize the shape of the VSF.

The change in ψ^* due to a change in c can be understood by referring to optical geometry in Figure 2.3. The total scattering volume is given by the intersection of the beam and detector FOV. However, the response of the sensor to each infinitesimal volume dV within the total scattering volume is weighted by $W(z;c)$. In air, where there is no attenuation of the light, the maximum response will be at the distance z_{peak} where dV is a maximum, since $W(z;c)$ is now a function only of the geometry. In water, the exponential attenuation of the light with distance shifts the maximum response closer to the sensor faceplate. As the attenuation increases, z_{peak} will decrease.

The spectral correction factor, $\sigma(c,c_w)$, given by Eq. 2.12, can be computed for any backscattering sensor using the procedure described above for computing $W(z;c)$. The $W(z;c_w)$ from the filtered water calibration needs only to be computed once and integrated. $W(z;c)$ is repeatedly computed for a range of c's and integrated. Taking the ratio of $\int W(z;c_w)dz$ and $\int W(z;c)dz$ for each value of c yields a curve for $\sigma(c,c_w)$. Figure 2.10 shows the result for the 440 nm channel of the BB-4. The initial c value on the horizontal axis is

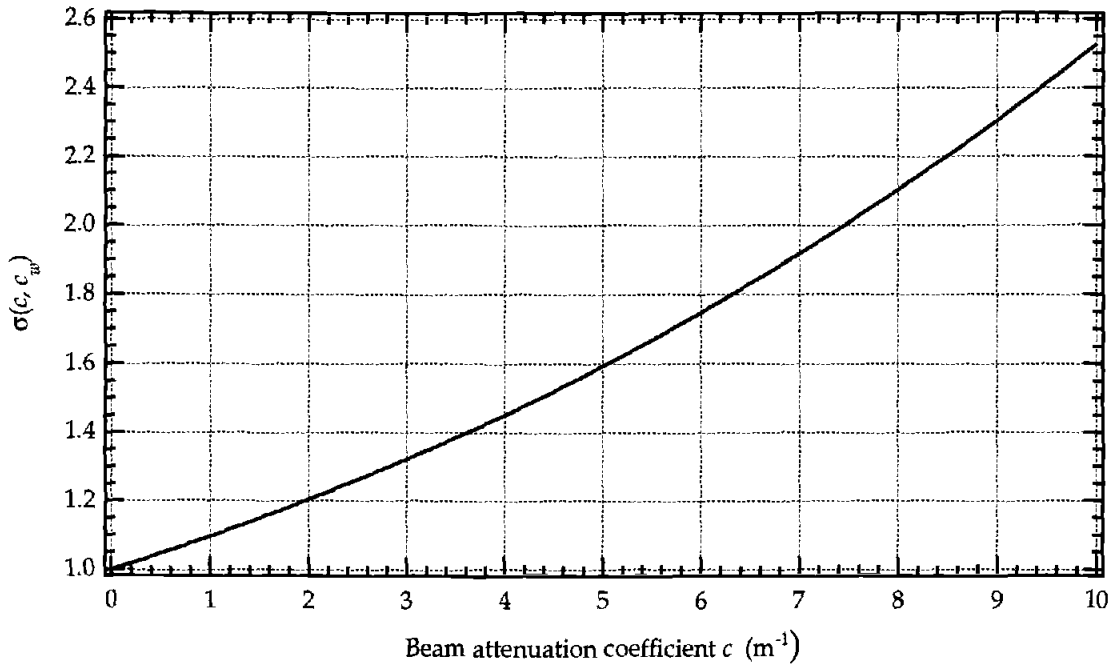

Figure 2.10 The attenuation correction factor $\sigma(c,c_w)$ computed for the 440 nm channel of the BB-4. The attenuation coefficient of the filtered water, c_w = 0.02 m^{-1} at 440 nm, was measured with the BB-4 transmissometer.

c_w = 0.02 m^{-1}, which was measured with the BB-4 transmissometer. This point corresponds to $\sigma(c,c_w)=\sigma(c_w,c_w)=1$. Values below this are not computed because the ocean water in which backscattering is measured should not be clearer than the filtered laboratory water.

As expected from the foregoing discussion, $\sigma(c,c_w)$ is a small correction factor for relatively low values of c. Even a value of c = 1 m^{-1} requires only about a 10% correction in $\beta(\psi^*)$. But a value of, say, c = 4 m^{-1} requires almost a 50% correction in $\beta(\psi^*)$, which is significant. Such high values of c(440 nm) are often found in coastal and productive open ocean waters. Moreover, in these regions, vertical variability can be extreme, giving large changes in c, as

well as $\beta(\psi^*)$, in a single profile. It is therefore important that all backscattering measurements be corrected for the attenuation of the water, so that measurements can be properly interpreted and compared. Although $\sigma(c,c_w)$ is a significant correction factor for high values of c, $\sigma(c,c_w)$ itself is a relatively weak function of c, at least for the optical geometry of the BB-4, and is therefore insensitive to changes, or errors, in the measurement of c. For example, a change in c from 0.02 to 1 m^{-1}, which is a change by a factor of 50, results in about a 10% change in $\sigma(c,c_w)$. This is why it is not mandatory for a transmissometer to have optics that match those of the backscattering sensor. For this particular application, almost any transmissometer is adequate, as long as the wavelengths match.

2.5.2.2 APL Backscattering Sensor

It is of interest to apply the above analysis to a backscattering sensor with an optical design that is significantly different than the BB-4. As noted earlier, the APL sensor was designed to measure the VSF at an angle as close to 180° as practical because the application was to use the measurements to calibrate the 180° backscattering received by a lidar system. The APL sensor response function, $\Delta\Phi_\rho(z)$ given by Eq. 2.8, was measured by APL personnel and kindly supplied to the authors [*Smart*, 1995]. The measured $\Delta\Phi_\rho(z)$ yielded the weighting function $W(z;c_w)$ shown in Figure 2.11.

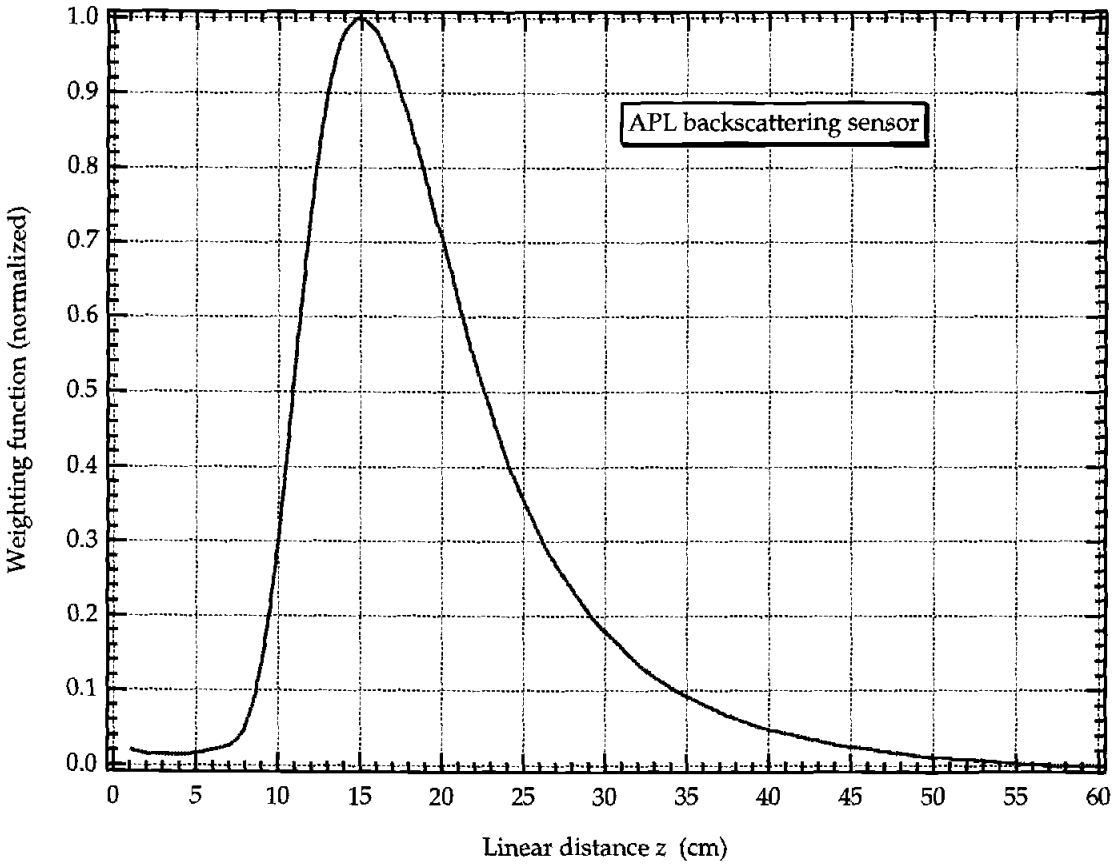

Figure 2.11 Weighting function $W(z;c_w)$.

Although the APL weighting function is qualitatively similar in shape to those seen in Figure 2.6 — especially to that of the 2nd generation sensor — there is an important difference. Because the APL sensor is designed to detect backscattering at very large scattering angles, the linear distance z over which the sensor responds is relatively large, as seen in Figure 2.11. For example, the APL sensor response falls below 10% of its peak at about 35 cm, as compared with 17 cm for the 2nd generation sensor and 7 cm for the BB-4. This is due to the low crossing angle of the beam and detector FOV, as is required to detect scattering at large angles. Referring back to Figure 2.3, the

angles θ_{0s} and θ_{0d} for the APL sensor are both 6°. For the BB-4, these angles are both approximately 19°.

The important consequence of the long linear extent of a backscattering sensor's response, or its weighting function, is the greater effect the attenuation of the water will have on the backscattering measurement. The higher the backscattering angle, the greater will be the effect of beam attenuation by the water. Indeed, the calibration of another backscattering sensor, called Beta Pi, which was developed by the authors and which measures backscattering at exactly 180°, depends directly on the beam attenuation coefficient [*Maffione and Dana*, 1996].

The centroid scattering angle of the APL sensor was calculated in the manner described above. At c_w = 0.03 m^{-1} (filtered water at λ = 490 nm), ψ^*=168.0°, which is impressively close to 180° for a bi-static backscattering sensor. At c_w = 0.75 m^{-1}, however, ψ^* = 157.0°, which is about the minimum ψ^* for the APL sensor, because its response function is essentially zero below this angle. The attenuation correction factor $\sigma(c,c_w)$ for the APL sensor, which is shown in Figure 2.12, is even more revealing. The correction factor is nearly twice as great as for the BB-4. But again, this is not a significant correction for measurements in clear ocean water, where c(490 nm) < 0.5 m^{-1}, which, without a correction, results in an error in β of less than 10%. For productive or coastal waters, however, where c(490 nm) can often be greater than 1 or even 2 m^{-1}, the attenuation correction can be quite significant.

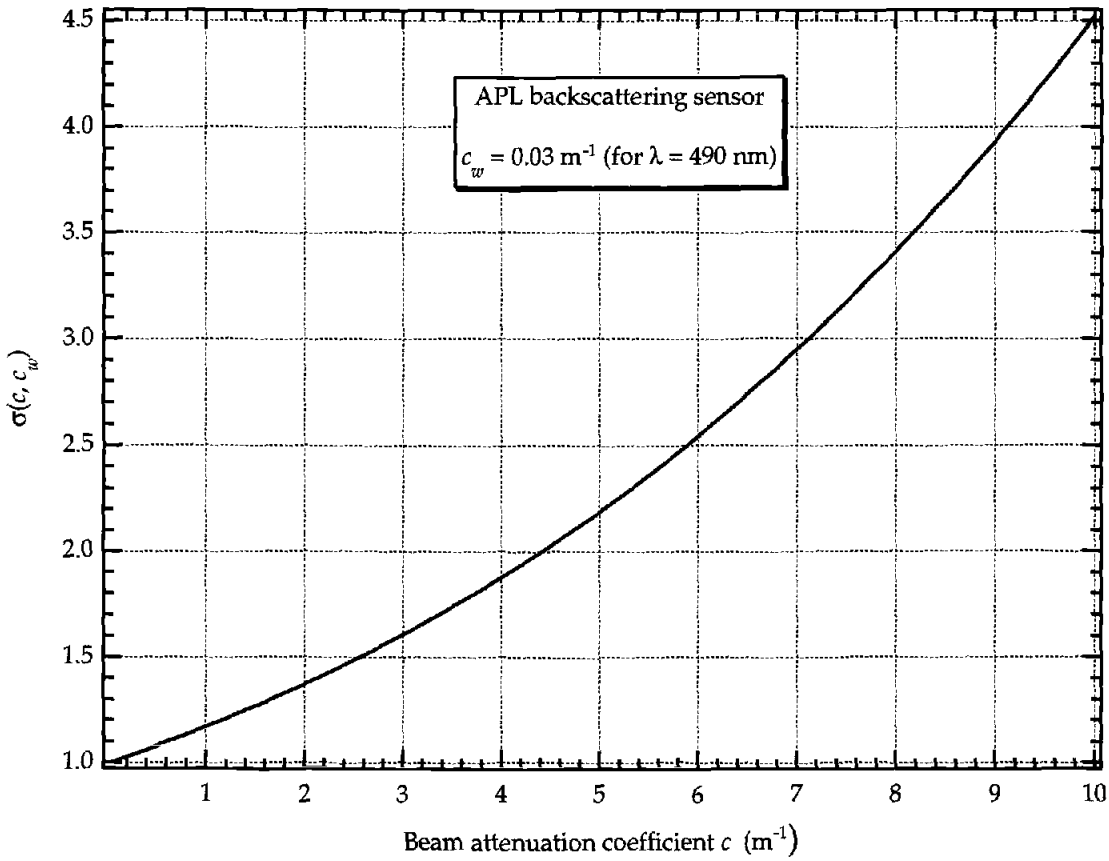

Figure 2.12 The attenuation correction factor $\sigma(c,c_w)$ for the APL backscattering sensor. The attenuation coefficient of the filtered water was estimated to be c_w = 0.03 m^{-1} at 490 nm.

2.5.3 Estimation of the Backward Scattering Coefficient

In principle, the backward scattering coefficient b_b is determined by measuring $\beta(\psi)$ over the range 90° to 180° and then calculating its solid angle integral over the backward hemisphere. For the routine measurement of b_b in the ocean, this is clearly impractical. Following the long tradition of searching for a simple means to measure b, the total scattering coefficient,

researchers have wondered if there is a "magic" angle, ψ_χ, in the backward hemisphere such that

$$b_b = \chi 2\pi \beta(\psi_\chi), \tag{2.17}$$

where χ is either assumed constant or can be parameterized in some simple fashion. An analysis of this conjecture is given next.

There is some justification for the form of Eq. 2.17. For instance, the integral mean value theorem can be applied to the definition of the backward scattering coefficient b_b, Eq. 2.3, so that,

$$\begin{aligned} b_b &= 2\pi \int_{\pi/2}^{\pi} \beta(\psi) \sin\psi \, d\psi \\ &= 2\pi \beta(\psi^*) \int_{\pi/2}^{\pi} \sin\psi \, d\psi \\ &= 2\pi \beta(\psi^*) \end{aligned} \tag{2.18}$$

where once again ψ^* takes on whatever value, within the limits of integration, that makes $\beta(\psi^*)$ give the last equality in Eq. 2.18. Clearly, ψ^* will depend on the shape of $\beta(\psi)$. But ψ^* also depends on $\sin\psi$, analogous to the discussion above involving the product $\beta[\psi(z)]W(z;c)$. In the latter case $W(z;c)$ is the dominant function in determining ψ^*. If, then, $\beta(\psi)$ is a weak function of ψ as compared with $\sin\psi$ over the limits of integration, then $\sin\psi$ will predominately determine ψ^*. For example, consider $\beta(\psi)$ to be relatively constant in the range $\pi/2 \le \psi \le \pi$. Then ψ^* is mainly determined by

$$\int_{\pi/2}^{\pi} \sin\psi \, d\psi = \sin\psi^* \int_{\pi/2}^{\pi} d\psi,$$

giving

$$\sin\psi^* \pi/2 = 1,$$

or $\psi^* = 140°$. In other words, this suggests that b_b can be estimated by

$$b_b \cong 2\pi\beta(140°).$$

Oishi [1990] published an analysis on estimating b_b from a single measurement of $\beta(\psi)$ in the backward hemisphere. His work mainly focused on Mie scattering functions for a polydisperse system of particles assumed to obey a Junge, or hyperbolic size distribution, although he also included some empirical VSF data published by others. Oishi's conclusion was that $\beta(120°)$ gave the highest correlation to a linear expression for estimating b_b. For this angle, he reports $\chi = 1.14$ with an additive constant of $-0.43\times10^{-4}\,\mathrm{m}^{-1}$. The results he presents for other angles, however, show no statistically significant difference in using $\beta(120°)$, $\beta(130°)$, or $\beta(140°)$. Indeed, Oishi reports that the regression for $\beta(140°)$ gave a maximum prediction error that was *less* than that for $\beta(120°)$. Considering all of the uncertainties in his analysis, such as the calculations using Mie theory and the meager empirical data set that was available, it might seem that the wiser choice is the angle that gives the lowest *maximum* prediction error. For 140°, Oishi reports $\chi = 1.08$ with an additive constant of $-1.62\times10^{-4}\,\mathrm{m}^{-1}$.

An analysis of one of the most well-documented empirical data sets of the VSF, namely that of *Petzold* [1972], further sheds light on this issue. Petzold's ocean measurements falls into three categories: 1) clear ocean water,

measured in Tongue-of-the-Ocean (TOTO), Bahamas, 2) coastal water, measured off the coast of southern California, and 3) murky water, measured in San Diego Harbor. His results are presented in Figure 2.13 for the range 90° to 180°, although $\beta(180°)$ was not actually measured and is an extrapolation by Petzold (which is not relevant to this discussion since these values are multiplied by $\sin\pi = 0$). Each curve represents an average of all of the data reported by Petzold for its particular category. The VSF's are normalized by the factor $2\pi/b_b$ for better comparison— in other words the curves are actually $\tilde{\beta}(\psi) \equiv 2\pi\beta(\psi)/b_b$, so that where $\tilde{\beta}(\psi) = 1$, $b_b = 2\pi\beta(\psi)$.

At first glance, it appears that Petzold's data confirm Oishi's conclusion. The three curves for the three different water types have the smallest spread at about 120°. Note, however, that if the harbor water data are excluded, the two remaining curves remain fairly close together throughout the angular range from 100° to 160°. The differences between the two curves at 120° and 140° are nearly equal, although the percentage difference is slightly less at 140°. Also note that the TOTO and coastal water curves cross the value of 1 near 140°, which lends support to Oishi's value of $\chi = 1.08$ for 140°.

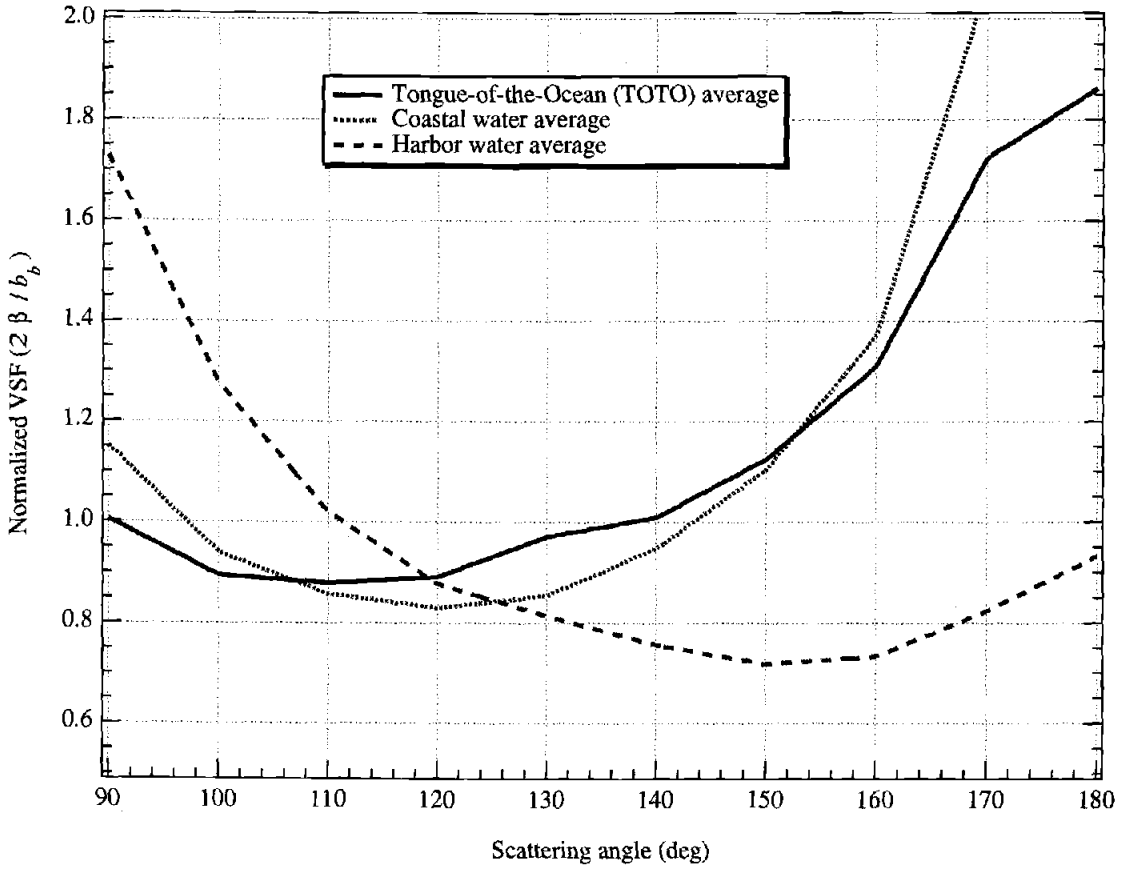

Figure 2.13. VSF measurements by *Petzold* [1972], normalized by the factor $2\pi/b_b$. Each curve is an average of all of the data reported by Petzold for that water type.

There are compelling reasons to question the accuracy of Petzold's harbor water data. The harbor water had a relatively high attenuation coefficient, averaging about $c = 2$ m^{-1} at 530 nm, the wavelength at which the VSF's were measured. It is known that Petzold did not properly correct for the water attenuation, and that the greatest errors were expected for measurements of turbid water [*Smith*, 1996]. Moreoever, a published analysis of general-angle scattering meters of the type used by Petzold also showed that for scattering angles in the backward hemisphere, systematic errors, which depend on the

light attenuation of the water, occur in the VSF measurements [*Jonasz*, 1990]. As shown above, the attenuation correction factor, $\sigma(c,c_w)$ increases with increasing c. In other words, without applying the correction factor, the measurement will underestimate $\beta(\psi > 90\,\text{deg})$ and the error will increase as c increases. When properly normalized for comparison, Petzold's harbor data are much lower than his measurements in clearer water at angles greater than 120°, suggesting these measurements suffer from errors due to light attenuation, which Figure 2.13 illustrates rather dramatically.

Given all the uncertainties in the VSF measurements published by Petzold and others, and given the uncertainty of using Mie theory to compute ocean water VSF's, the foregoing discussion strongly suggests that 140° is statistically as good an angle as 120°, and perhaps even better, for measuring $\beta(\psi)$ in order to estimate b_b. The data of Petzold, excluding the harbor water curve in Figure 2.13, and the analysis by Oishi both indicate that the best estimate of χ near 140° is $\chi = 1.1$, in which case,

$$b_b \cong 1.1 \times 2\pi\,\beta(140\,\text{deg}). \tag{2.19}$$

Until more accurate and comprehensive data on ocean-water VSF's in the backward hemisphere are available, Eq. 2.19 is probably just as accurate as using Oishi's results for 120° or any other method. From a statistical analysis of Petzold's measurements, excluding the harbor water data, the percent standard error in using Eq. 2.19 to estimate b_b was 5%, and the maximum error was about 10%.

2.6 SUMMARY AND CONCLUSIONS

A general analysis of fixed-angle backscattering sensors showed that their total response to volume scattering was given by Eq. 2.7, which is essentially a weighted integral of the VSF. The weighting function $W(z;c)$, Eq. 2.6, was shown to be a function of both the geometry of the sensor, which is fixed, and the beam attenuation coefficient c of the water, which is variable. However, the derivation of $W(z;c)$ showed that it could be analytically separated into two factors, one solely a function of the sensor optical geometry, $G(z)$ given by Eq. 2.14, and the other a simple exponential function of c.

The weighting function is fundamental to calibrating backscattering sensors and properly interpreting their measurements. A procedure was given for accurately determing a sensor's weighting function. This procedure involves first measuring the in-water response of the sensor to a Lambertian target as a function of distance z. Dividing this measured response function, $\Delta\Phi_\rho(z)$ given by Eq. 2.8, then yields $W(z;c_w)$ to within a multiplicative constant that does not need to be known. $G(z)$ can also be calculated from $\Delta\Phi_\rho(z)$, as shown by Eq. 2.13. Once $G(z)$ is known, $W(z;c)$ can be calculated for any value of c.

When $W(z;c)$ for a particular backscattering sensor is known, the sensor can be accurately calibrated to yield measurements of $\beta(\psi^*)$ in absolute units, where ψ^* was shown to be a very close approximation to the centroid angle of $W(z;c)$. Because $W(z;c)$ depends on c, so does ψ^*, although it was shown to

be only a weak function of c. In the worse case, ψ^* changed by about 10° when c changed by a factor of 25.

A correction factor, $\sigma(c,c_w)$ given by Eq. 2.12, was derived that corrects the backscattering measurement for the light attenuation by the water. $\sigma(c,c_w)$, like ψ^*, was also shown to be a weak function of c. However, for coastal and productive open-ocean waters, where c can often be large as well as highly variable, neglecting the $\sigma(c,c_w)$ correction can result in significant errors in backscattering measurements.

An analysis of a recently developed four-wavelength sensor, the BB-4, gave $\psi^* = 141°$ at $c_w = 0.02\,\mathrm{m}^{-1}$ (440 nm). For all backscattering sensors, ψ^* decreases with increasing c and asymptotes to some minimum value that depends on the sensors optical geometry. For the BB-4, this mimimum value was found to be $\psi^* = 134$ at $c(440\text{ nm}) = 0.5\,\mathrm{m}^{-1}$. An analysis of the APL sensor showed that, at 490 nm, $\psi^* = 168°$ at $c_w = 0.03\,\mathrm{m}^{-1}$, and the minimum was $\psi^* = 157$ at $c = 0.75\,\mathrm{m}^{-1}$. Thus measurements by the APL sensor can be relatively sensitive to changes in c as a consequence of the low crossing angle of the beam and detector FOV. The attenuation correction factor $\sigma(c,c_w)$ for the APL sensor was found to be nearly twice as large as $\sigma(c,c_w)$ for the BB-4. However, the correction is significant only when the attenuation of the water is relatively high. Since $\sigma(c,c_w)$ can be determined, it should, nonetheless, always be applied.

The conjecture that the backward scattering coefficient b_b can be estimated with a measurement of the VSF at a single angle in the backward hemisphere was examined. Oishi's analysis [1990] concluded that $1.14 \times 2\pi\beta(120°) - 0.43 \times 10^{-4}\,\mathrm{m}^{-1}$ provides the best estimate of b_b for the computed and observed scattering functions he considered. However, he also reported that $1.08 \times 2\pi\beta(140°) - 1.62 \times 10^{-4}\,\mathrm{m}^{-1}$ gives the least maximum likely error in estimating b_b. VSF measurements by *Petzold* [1972] were examined in the present paper, where it was argued that his turbid water measurements were probably systematically low in the backward hemisphere because they were not properly corrected for light attenuation by the water. An analysis of general-angle scattering meters by *Jonasz* [1990] arrived at a similar conclusion. When the turbid water measurements were excluded in the type of analysis performed by Oishi, it was found that estimating b_b from $\chi 2\pi\beta(\psi_\chi)$, where χ is a constant for the particular angle ψ_χ, there was no statisically significant difference between using $\beta(120°)$ or $\beta(140°)$, or even VSF values between these angles. The expression $b_b \cong 1.1 \times 2\pi\beta(140\ \mathrm{deg})$ was suggested as providing the best estimate of b_b from measurements of $\beta(\psi^*)$ using the BB-4, where ψ^* is nominally 140°.

Chapter 3

IN-SITU CHARACTERIZATION OF OPTICAL BACKSCATTERING AND ATTENUATION FOR LIDAR APPLICATIONS

Robert A. Maffione and David R. Dana

1996, SPIE (in press).

3.1 ABSTRACT

Measurements of ocean-water optical properties that are directly relevant to airborne oceanographic lidar (AOL) systems are rare. The two most important water optical properties to AOL systems are the volume scattering function (VSF) at 180° and the lidar beam attenuation coefficient. An instrument has been developed, called Beta Pi, which measures, *in situ*, these two optical parameters. It is a self-calibrating instrument that provides an accurate measurement of both the VSF at 180° and the lidar attenuation coefficient. Results from a deployment in the Gulf of Mexico near Panama City, Florida, during a Navy lidar test, are given. It was found that the VSF increases by more than 50% from 179° to 180°. A sharp enhancement, possibly due to coherent backscattering, was also observed at 180° with an angular width of about 0.03°. Measurements made at six discrete wavelengths from 457 to 532 nm revealed that the spectral dispersion of backscattering at and near 180° was substantially greater than the dispersion at 135° measured with multispectral bi-static backscattering sensors. All of these results have important implications to the sea truth calibration of AOL systems.

3.2 INTRODUCTION

Ocean remote sensing using airborne lidar is a powerful method for investigating the near-surface water column. NASA's airborne oceanographic lidar (AOL), for example, is well documented [*Hoge et al.*, 1986a; *Hoge et al.*, 1986b] and has been in use for many years. Most airborne lidars use a narrow,

collimated pulsed beam to illuminate the upper water column and a range-gated receiver to measure the backscattered return from a selected depth. Varying the range gate of the receiver produces a measured profile of the backscattering and attenuation properties of the upper water column. Some systems can penetrate as far as four to five attenuation lengths which, at 532 nm in clear oligotrophic waters, can be deeper than 50 m.

The real utility of airborne oceanographic lidar is its rapid surveillance capability compared with shipborne surveys. Unlike shipborne measurements, however, interpreting lidar measurements is far more difficult. First, a forward model is required that describes, 1) the propagation of the beam through the water column, 2) the backscattering at the range-gated depth, and 3) the propagation of the backscattered light to the receiver. The model must then be inverted to obtain the in-water parameters of interest. Single-scattering (SS) models are the simplest and they permit inversion so that profiles of the backscattering and attenuation properties of the water column can be obtained. The inversion of an SS model can provide the volume scattering function (VSF) in the backward direction, $\beta(180)$, and the beam attenuation coefficient, c. The next level of sophistication are quasi-multiple-scattering (QMS) models such as the one described by *Gordon*. [1982]. The mathematical forms of QMS models are the same as SS models, but the inherent optical properties (IOP's) $\beta(180)$ and c are replaced by quasi-inherent optical properties (QOP's), usually denoted with a prime, i.e., $\beta'(180)$ and c'. These QOP's are considered to take on whatever values that will force the

QMS model to accurately describe the propagation of the beam through the water. Typically, the farther the beam propagates, the more it is modified by multiple scattering, and the further the QOP's will diverge from their corresponding IOP's.

Experimental verification of ocean lidar models requires sea truth — that is, the direct measurement of the relevant optical parameters. Historically this is rarely done, so that lidar model testing is usually a bootstrap procedure where the accuracy of the model is judged by how reasonable or self-consistent the results look. Models are even tested (and developed) with other models. For example, the QOP's have been investigated using the Monte Carlo method [*Gordon*, 1982]. Even when sea truth is performed, it is exceedingly rare for all of the appropriate IOP's to be measured. The beam attenuation coefficient is unquestionably the most commonly measured IOP relevant to lidar, but rarely is the optical design of the transmissometer matched with the optical parameters of the lidar system, such as beam divergence and receiver FOV. This is important because drastically different values of "*c*" can be obtained when measured by two transmissometers with different receiver acceptance angles due to the extremely large slope of the VSF in the near forward direction. Transmissometer path-length can have a significant effect on the accuracy of the measurement of c as well. The downwelling irradiance attenuation coefficient, K_d, is also routinely measured and is believed to approximate the total round-trip attenuation of the lidar beam, especially for long path-

lengths. In other words, K_d, an apparent optical property (AOP), is thought to approximate c', a QOP, for long path-lengths. This connection, however, is by no means firmly established in a quantitative way. Moreover, K_d, by its very definition as an AOP, can change with changes in boundary conditions such as sun angle and cloud cover, although methods have been proposed to correct for this [*Gordon et al.*, 1975; *Gordon*, 1980]. Another problem is that K_d is difficult to accurately measure near the surface due to ship shadow and wave motion effects.

Until the development of the instrument described in this paper, called Beta Pi [*Maffione and Honey*, 1992], the one optical parameter that had never been measured was $\beta(180)$. On rare occasions, mainly during the testing of Navy lidar systems, optical backscattering was measured with bi-static sensors [*Dana and Honey*, 1990; *Maffione et al.*, 1991]. These backscattering sensors, originally developed at SRI International, measure a weighted angular average of the VSF at a centroid angle between 135° and 150° depending on the design of the sensor optics. The Johns Hopkins University Applied Physics Laboratory has developed a backscattering sensor with a centroid angle approaching 170° [*Smart*, 1991]. When these sensors are used for lidar sea truthing, it is assumed that the VSF is fairly flat over the backward angles so that the bi-static measurements are a good approximation to $\beta(180)$. There is evidence to suggest, however, from VSF measurements that were made over a range of discrete angles up to 170° and from Mie scattering computations, that the VSF sharply increases from 170° to 180° [*Kullenberg*,

1974; *Petzold*, 1972]. Also, questions have been raised about the possibility of enhanced backscattering [*Kuga and Ishimaru*, 1984; 1989; *Tsang and Ishimaru*, 1984; *Ishimaru and Tsang*, 1988] by ocean water [*Maffione and Honey*, 1992].

Thus, despite all of the modeling that has been done on beam propagation in the ocean, there is still little firm knowledge of ocean optical properties relevant to lidar applications. This is mainly because these properties need to be measured directly, and rarely is there instrumentation developed for this purpose. Until the relevant optical properties are definitively measured, we are only guessing at their values and behavior. Beta Pi, described in the present paper and in greater detail elsewhere [*Maffione and Honey*, 1992] was designed specifically to address this issue. This instrument was recently modified to include a new type of variable path-length beam transmissometer for measuring the lidar attenuation coefficient. Preliminary results are presented from a deployment in the Gulf of Mexico near Panama City, Florida, during a Navy test in the summer of 1994.

3.3 LIDAR MODELS

An elastic single-scattering model that describes the returned power $d\Phi$ at the lidar receiver in the time interval $t + dt$ due to a short laser pulse is straightforward to derive and can be expressed in the form

$$d\Phi = \frac{T^2 \Phi_0 A \beta(180) \exp\left[-cv(t-t_0)/n\right] v dt/2n}{\left[nH + v(t-t_0)/2n\right]^2}. \tag{3.1}$$

The lidar receiver, which is at a height H above the water, has an effective receiving area A. Φ_0 is the laser power at the sea surface and T is the Fresnel

transmittance of the air-sea interface. The quantity $v(t-t_0)/2n$ is the penetration depth at which the light received by the lidar was scattered, where v is the speed of light *in vacuo*, t - t_0 is the total round-trip travel time of the beam in the water, and n is the refractive index of the water. Two inherent water optical properties, discussed previously, appear in Eq. 3.1: $\beta(180)$ and c.

Equation 3.1 can be simplified, following *Gordon* [1982], by defining the normalized returned power

$$\left[d\Phi(t)/dt\right]_{\text{norm}} \equiv \left[2n/\Phi_0 AvT^2\right]\left[nH + v(t-t_0)/2n\right]^2 d\Phi(t)/dt$$

so that

$$\begin{aligned}\left[d\Phi(t)/dt\right]_{\text{norm}} &= \beta(180)\exp\left[-cv(t-t_0)/n\right] \\ &= \beta(180)\exp\left[-2cz\right]\end{aligned}, \tag{3.2}$$

where $z = v(t-t_0)/2n$ is the penetration depth as noted above. The utility of Eq. 3.2 lies in its easy inversion to obtain IOP profiles of $\beta(180)$ and c simply by fitting $\left[d\Phi(t)/dt\right]_{\text{norm}}$ to an exponential.

Strictly speaking, Eq. 3.2 is valid only for a perfectly collimated beam and a receiver with an infinitesimal area and FOV. Anything less than this ideal situation will inevitably involve multiple scattering effects. Probably the simplest, and most common way to deal with this is to retain the form of Eq. 3.2, but modify the IOP's. These are the QOP's referred to earlier. A more accurate model is then expressed by

$$\left[d\Phi(t)/dt\right]_{\text{norm}} = \beta'(180)\exp\left[-2c'z\right]. \tag{3.3}$$

The problem now is to understand these QOP's and their relationships to both the IOP's and the lidar system parameters.

Consider, for example, multiple scattering effects on the attenuation coefficient. As the beam propagates through the water, multiple scattering of light back into the beam will decrease its attenuation. Thus the actual attenuation of the beam power from source to receiver should be described by an attenuation coefficient that is less than c. The receiver FOV can also greatly affect the received power, altering the measured beam attenuation. The larger the FOV, the more power received due to multiple scattering by the water, and therefore the lower the computed value of the attenuation coefficient. Because the computed lidar attenuation coefficient is a function of the lidar system parameters as well as the IOP's, it is often denoted K_{sys} (= c' in Eq. 3.3). It should be clear that $a \leq K_{sys} \leq c$, where a is the absorption coefficient. Intuition suggests that a single scattering approximation is accurate for propagation through two, and probably three attenuation lengths (an attenuation length is defined as $1/c$) provided the receiver FOV is narrow. Monte Carlo studies of the point spread function, which is mathematically equivalent to the beam spread function [*Mertens and Replogle*, 1977], by *Maffione and Jaffe* [1995] found that the asymptotic state of beam spreading is not attained after 20 attenuation lengths, even in a highly scattering medium, suggesting that multiple scattering does not appreciably alter the beam attenuation coefficient when measured with a narrow FOV receiver. The greatest effects of multiple scattering have been shown to depend on cR,

where R is the radius of the spot on the sea surface that is seen by the lidar receiver [*Gordon*, 1982]. So it is not just the receiver FOV that matters, but also the height of the lidar above the water. The most useful measurement of an attenuation parameter for lidar sea truth, then, is the round-trip attenuation coefficient for the case of a narrow beam and small spot size seen by the receiver. Changes in actual spot size, or cR, can then be correlated with differences in K_{sys} (or c' in Eq. 3.3) as determined by the lidar and the sea truth measurement of c.

Equation 3.3 reveals that the easiest and most accurate water optical property that a lidar system can determine is K_{sys}, provided that the water column is homogeneous in the depth interval where the exponential fit is made to the received signal. In this case K_{sys} is simply given by the slope of the natural log of $[d\Phi(t)/dt]_{norm}$, which does not have to be known in absolute units. Neither does $\beta(180)$ have to be known, except for the required assumption that it is constant over the depth interval used in the log-linear regression to obtain K_{sys}. On the other hand, to determine $\beta(180)$ from the regression, $[d\Phi(t)/dt]_{norm}$ has to be known in absolute units. This can be exceedingly error prone since some of the parameters in $[d\Phi(t)/dt]_{norm}$ are not accurately known. For example, the (average) Fresnel reflection coefficient T will depend on the wave spectrum of the sea surface, which can be highly variable and is usually unknown. Clearly then, to accurately calibrate an ocean lidar system, both c and $\beta(180)$ must be measured *in situ*. It is also important to note that the assumption of vertical homogeneity is not always

valid, and in fact is usually wrong for coastal waters, especially when they are productive. Moreover, c and $\beta(180)$ can not be expected to covary in a regular, predictable manner. The proper *in-situ* characterization of water optical properties relevant to lidar is thus critical to accurately calibrating these systems and interpreting their signals.

3.4 *IN-SITU* INSTRUMENTATION: BETA PI

Beta Pi, shown schematically in Figure 3.1, was developed specifically to measure, *in situ*, $\beta(180)$ and the VSF near 180°. This instrument is well documented by *Maffione and Honey* [1992], although a brief overview is given here for completeness. Beta Pi was recently modified to include an attachment that converts the instrument to a unique, variable path-length beam transmissometer. The variable path-length attachment also makes Beta Pi a highly accurate, self-calibrating instrument. An updated analysis of the calibration of Beta Pi is thus presented.

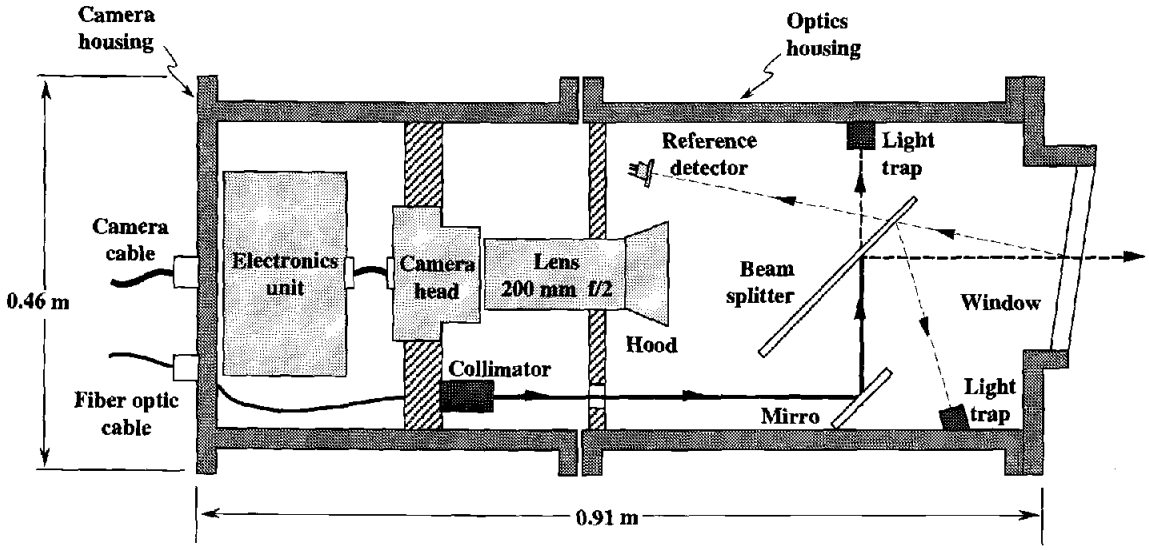

Figure 3.1 Schematic layout of "Beta Pi," the instrument that measures the volume scattering function at and near 180°. Not all light traps are shown. The attachment for performing variable path-length beam transmission measurements is also not shown. This attachment fits over the pressure window housing and extends out 1.2 m. A motor drive system, controlled at the surface, moves a Spectralon target along the length of the attachment. An optical encoder records the range of the target.

The monostatic geometry necessary for measuring $\beta(180)$ is achieved with a beam splitter as shown in Figure 3.1. A laser beam is bounced off of the beam splitter where half its power is sent out into the water. The other half of the beam power that is transmitted through the splitter is efficiently dumped with a novel light trap arrangement (see *Maffione and Honey* for further details). It is vital that all specular reflections of the beam off of the optical surfaces be accounted for and removed with light traps, so that only the light scattered backward by the water is seen by the detector. A Photometrics cooled integrating CCD camera is the detector. A 516 x 516 pixel array sits at the focal plane of a 200 mm, f/2 lens that looks down the axis of the beam that is sent out into the water. Pixel size is 20 μm so that the

angular resolution of the camera *in water* is 0.0750 mrad = 0.00430°; the useful range of scattering angles is about 178.6° to 180°. An underwater multi-mode fiber optic cable, with a core diameter of 50 μm, is used to send the laser power from the surface to Beta Pi, an arrangement which allows for the tuning or interchange of lasers to measure multispectral backscattering. A beam expander collimates the laser power exiting the optical fiber and an aperture reduces the beam diameter to 1 cm. The focal length of the expander is 80 mm which works out to a half-angle beam divergence in water of 0.23 mrad = 0.013°. Since this is greater than the angular resolution of the CCD camera, the actual resolution of the VSF measurement is 0.013°, which is still more than sufficient for resolving phenomena such as enhanced backscattering.

Figure 3.2 shows the geometry for measuring the VSF over a small range of angles in the backward direction. The incremental backscattered energy dQ incident on a pixel that views a scattering angle θ is given by

$$\begin{aligned} dQ(r,\theta) &= \beta(\theta)\tau s \Phi_0 \Delta\Omega\, T f(r,\theta) e^{-2cr} dr \\ &= \beta(\theta)\tau s \eta f(r,\theta) e^{-2cr} dr \end{aligned} \qquad (3.4)$$

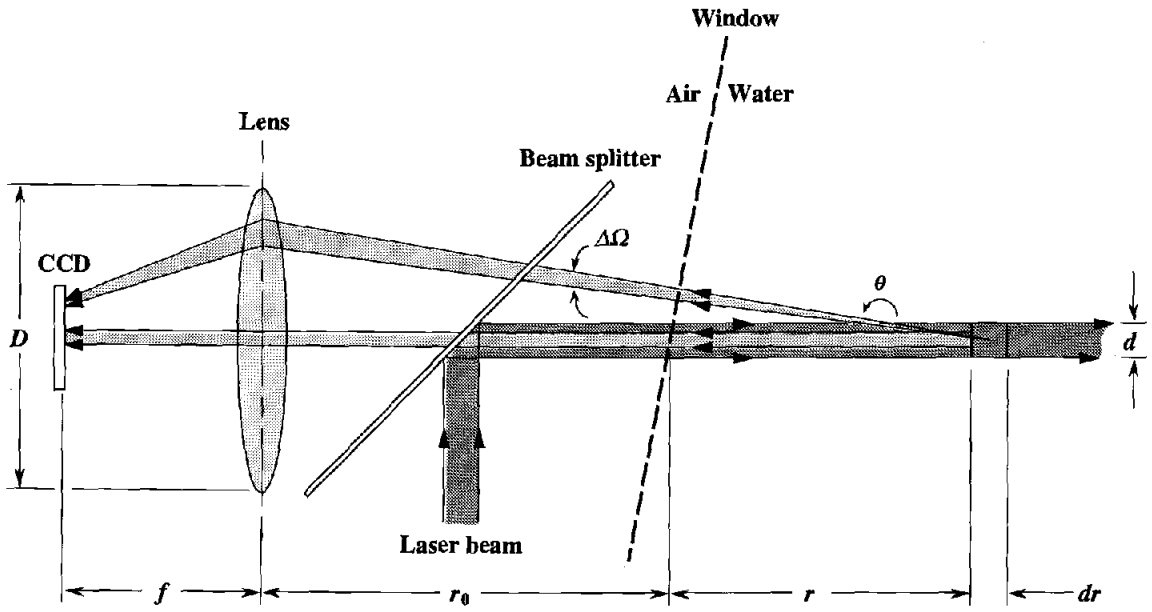

Figure 3.2 Geometry for measuring the VSF at and near 180°.

In this expression, $\tau\, s \Phi_0$ represents the total laser energy emitted into the water over the integration time τ; s is a reference detector signal which monitors the output of the laser and is normalized to a reference power Φ_0. $\Delta\Omega$ is the solid angle FOV of a pixel and T is the transmission loss factor for the backscattered flux in traveling through the optical train to the detector pixel. The quantity $\eta = \Phi_0 \Delta\Omega\, T$ is constant and, as shown below, does not need to be known because the calibration to obtain the VSF divides it out. The factor $\exp(-2cr)$ takes into account the round-trip attenuation of the forward beam and the backscattered flux. The function $f(r,\theta)$ in Eq. 3.4 represents the vignetting of the backscattered flux at the detector due to the finite size of the lens. For example, $f(r,180) = 1$ for all r, and $f(r,\theta > \theta_{\min}) = 0$, where $\theta_{\min}$ is the minimum scattering angle the detector can see ($\cong 178.9°$).

Between θ_{min} and 180°, $f(r,\theta)$ falls between 0 and 1 depending on the distance r and geometric parameters such as the diameter of the lens and the beam [*Maffione and Honey*, 1992].

The total backscattered energy incident on a pixel during the integration time τ is then

$$\begin{aligned} Q(\theta) &= \beta(\theta)\tau s\eta \int_0^\infty f(r,\theta)e^{-2cr}dr \\ &= \beta(\theta)\tau s\eta G(\theta)/2c \end{aligned}, \tag{3.5}$$

where $G(\theta) \equiv 2c\int_0^\infty f(r,\theta)e^{-2cr}dr$ is the vignetting correction function. The purpose of the factor $2c$ is to normalize $G(\theta)$ to unity at 180°; that is, $f(r,180)=1$ so that $G(180)=2c\int_0^\infty e^{-2cr}dr=1$. Note that in general $G(\theta)$ is a function of the parameter c. $G(\theta)$ can be accurately determined through a geometric analysis and surface backscattering measurements using a Lambertian target set at various distances r. Since, by definition, the surface scattering function of a Lambertian target is constant, roll-off in the angular response of the CCD quantifies the vignetting. Examples of $G(\theta)$ for values of c ranging from 0.1 to 0.5 m^{-1} are shown in Figure 3.3. Because of the large

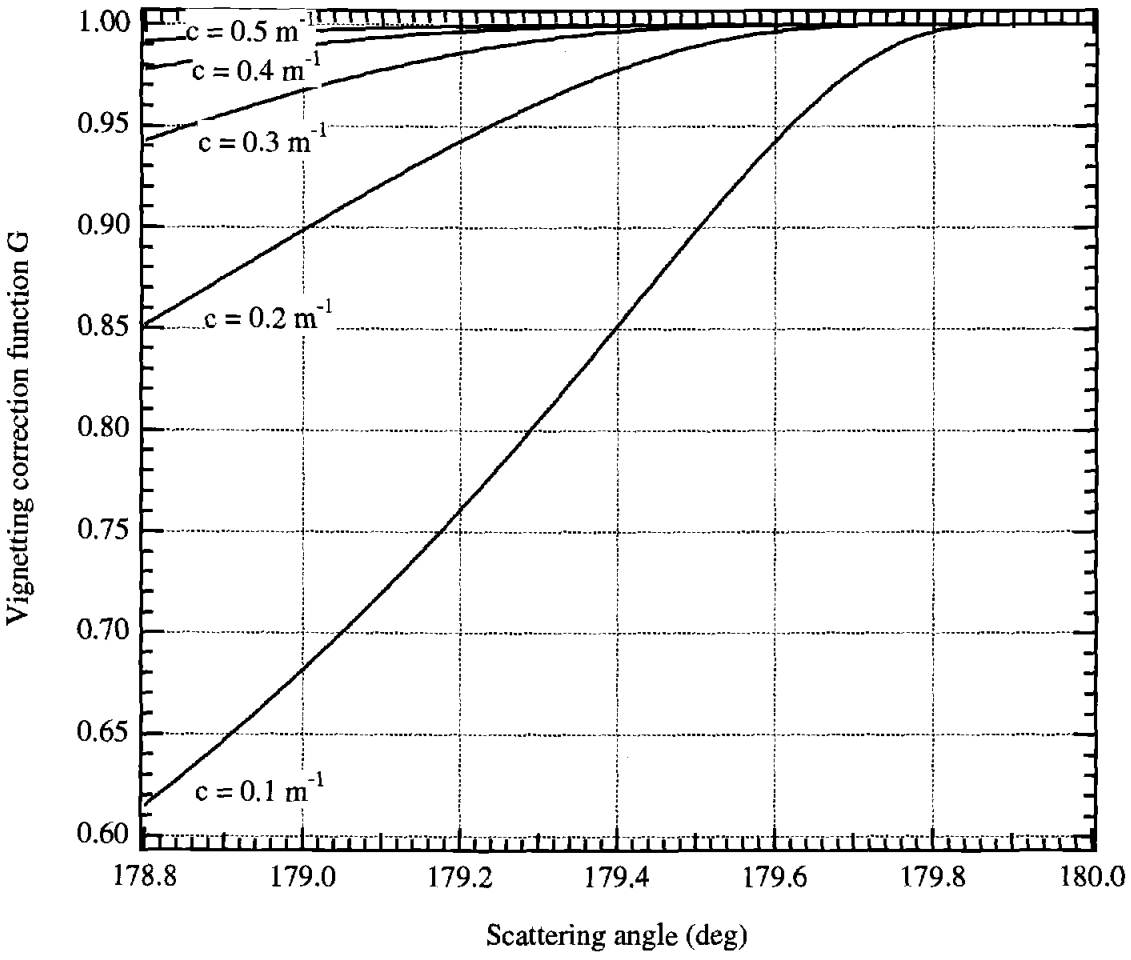

Figure 3.3 The vignetting correction function, $G(\theta) = 2c\int_0^\infty f(r,\theta)e^{-2cr}dr$, for values of c ranging from 0.1 to 0.5 m^{-1}. Because of the large diameter lens (10 cm) and long focal length, vignetting does not have a strong effect on the results, especially when $c > 0.5$ m^{-1}. Vignetting is also negligible from 179.8° to 180°, as expected.

diameter lens (10 cm) and its long focal length, as well as the exponential attenuation of light with distance, the total vignetting is not that severe. In fact it is virtually negligible for $c > 0.5$ m^{-1}. Analogous to Eq. 3.5, the radiant energy $Q_L(r,\theta)$ incident on a pixel due to backscattering by a Lambertian target placed a distance r in the path of the beam is

$$\begin{aligned} Q_L(r,\theta) &= \frac{\rho}{\pi}\tau_L s_L \eta f(r,\theta) e^{-2cr} + \varepsilon_w \\ &\cong \frac{\rho}{\pi}\tau_L s_L \eta f(r,\theta) e^{-2cr} \end{aligned}, \qquad (3.6)$$

where ρ is the diffuse reflectivity of the target and the quantity ρ/π — the surface scattering function (which is constant) — replaces the volume scattering function $\beta(\theta)$ in Eq. 3.5. ε_w represents the backscattering by the water in the volume between the window and the target. If ρ is close to 1 and $r < 1/2b$, where $b = c - a$ is the total scattering coefficient of the water, then ε_w is completely negligible compared with the first term. Since (ρ/π), τ_L, and s_L are known and η is constant, $f(r,\theta)$ can be obtained from measurements of $Q_L(r,\theta)$ assuming c is known. c can be obtained from the slope of a log-linear regression to $Q_L(r,\theta)$ as a function of r, analogous to the discussion in the previous section on obtaining K_{sys} from pulsed lidar measurements. This is best performed using measurements of $Q_L(r,\theta)$ in the range of r and θ for which $f(r,\theta)=1$. Letting $Q_L(r,\bar{\theta})$ denote the average of $Q_L(r,\theta)$ over a range of angles for which $f(r,\theta)=1$ at the range r, and multiplying $Q_L(r,\bar{\theta})$ by $\exp(2cr)$ yields

$$Q_L(r,\bar{\theta})\exp(2cr) = \frac{\rho}{\pi}\tau_L s_L \eta \equiv \hat{Q}_L(r) \quad (3.7)$$

where $\hat{Q}_L(r)$ is constant and therefore independent of r. Measurements of $\hat{Q}_L(r)$ can be obtained, however, over a range of distances r, and averaged to obtain the best estimate of $\hat{Q}_L$, i.e., $\hat{Q}_L \equiv \sum \hat{Q}_L(r_i)/N$ where N is the number of measurements.

Dividing $Q(\theta)$ by $\hat{Q}_L$, the average of $\hat{Q}_L(r)$, and solving for $\beta(\theta)$ gives

$$\beta(\theta) = \left[\frac{Q(\theta)}{ts}\right]\left[\frac{t_L s_L}{\hat{Q}_L}\right]\left[\frac{\rho}{\pi}\right]\left[\frac{2c}{G(\theta)}\right]. \quad (3.8)$$

The quantity in the first bracket represents the measurement of backward light scattering by the ocean water. The quantity in the second bracket represents the inverse of the measurement of surface backscattering by a Lambertian target. The multiplication of these two terms is thus a unitless number, so that only relative measurements of Q, τ, and s need to be made. Spectralon is used as the Lambertian target, so ρ = 0.99 is known to at least within 1% error. The beam attenuation coefficient c is measured directly with the variable path-length transmissometer attachment. Because the same beam source and receiver are used to measure both $\beta(\theta)$ and c, the measured value of c is the most appropriate c for Eq. 3.8. This c is, essentially, the multiple-scattering equivalent c', or K_{sys}, for the Beta Pi system, analogous to the lidar model discussion in Section 3.3. The vignetting correction function, $G(\theta)$, is likewise accurately determined from the variable path-length, surface-

scattering measurements with the Lambertian target. Thus Beta Pi is a fully self-calibrating instrument that accurately measures the VSF at and near 180° as well as the beam attenuation coefficient most appropriate to lidar.

3.5 RESULTS FROM GULF OF MEXICO NEAR PANAMA CITY, FLORIDA

Beta Pi was deployed in the Gulf of Mexico during the early summer of 1994 in support of Navy lidar tests. The research vessel was Mr. Offshore, which was anchored about 7 miles south of Panama City, Florida, where the bottom depth was approximately 30 m. The data reported here are for a deployment on the evening of August 2, 1994. These data are fairly representative of the measurements taken during the two-month test period. Throughout the test period, the water column showed little change in its optical properties. On the evening of August 2, the water column was homogeneous down to about 12 m, with a gradual increase in the IOP's, specifically backscattering and beam attenuation, down to about 26 m. In the last 4 m to the bottom, the IOP's sharply increased due to bottom turbidity caused by resuspended sediments. The Beta Pi measurements reported here were taken at 8 m.

Two lasers were used during this measurement series to obtain multispectral measurements of $\beta(\theta)$. A doubled Nd:YAG laser was used for the 532 nm measurements, and a tunable Argon ion laser was used for measurements at 457, 476, 488, 496, and 514 nm. At each selected wavelength, variable path-length measurements with the movable Lambertian target were first made to self-calibrate Beta Pi. Following the calibration measurements at

the selected wavelength, a series of water backscattering measurements was performed. Then another wavelength was selected and the procedure repeated. The entire series at six wavelengths took about 3 hours to complete. Vertical profiles both before and after the Beta Pi deployment, using our bi-static backscattering sensors [*Maffione et al.*, 1991], showed no changes in the optical properties of the water column.

The results of the self-calibration measurements at 488 nm, which are similar to the other five wavelengths, are shown in Figure 3.4. The movable Lambertian target, remotely controlled at the surface, was moved in 10 cm increments (20 cm total path-length increments). At each position a

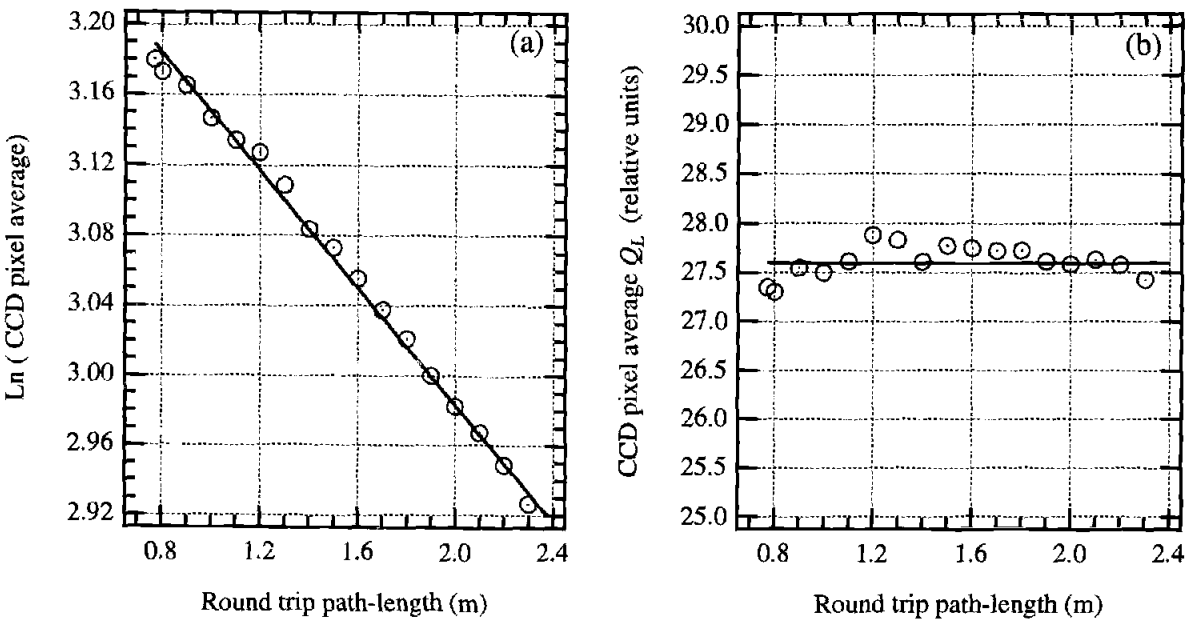

Figure 3.4 Variable path-length measurements with Beta Pi attachment at 488 nm. The left panel is the natural log of $Q_L(r,\bar{\theta})$ vs. round trip path-length. The negative of the slope of the regression yields the beam attenuation coefficient which in this case was $c = 0.167 \pm 0.003$ m^{-1}. The right panel shows $\hat{Q}_L(r)$ vs. total path-length. The average was $\hat{Q}_L = 27.6 \pm 0.2$.

measurement was made of the backscattered light by the target. At a 1.2 m distance from the window (total round trip path = 2.4 m), the target flips out of the path of the laser beam so that measurements of water backscattering can be made. Many prior tests have been performed with and without the attachment to insure that it has no affect on the measurement of the backscattering by the water alone. The regression to obtain c was extremely good, as shown in the left panel of Figure 3.4. The slope yielded a beam attenuation coefficient of $c = 0.167$ m^{-1} with a standard deviation of 0.003 m^{-1}, or an error of less than 2%. The right panel shows the $\hat{Q}_L(r)$ calculations which yielded an average value of $\hat{Q}_L = 27.6 \pm 0.2$, or a 0.7% error. Thus, the self calibration is quite good and accurate measurements of $\beta(\theta)$, with an estimated error of about 3%, were obtained.

Figure 3.5 shows the measured $\beta(\theta)$ at the six wavelengths over the angular range from 179° to 180°. The spectral dispersion in the backscattering follows a wavelength power law, with a negative exponent, as might be expected. In other words, backward light scattering increases with decreasing wavelength. The wavelength exponent was found to be -4.1, which is quite surprising since an exponent of -4.3 is expected for pure sea-water backscattering [*Morel*, 1974]. Although the water was fairly clear at 8 m, it was by no means pure sea water, which is expected to have a value of c around 0.22 m^{-1}. The spectral measurements with bi-static backscattering sensors, which measure the VSF at around 135°, yielded an exponent of about -2.2 at 8

m, indicating a significant change in the spectral dispersion of $\beta(\theta)$ in going from lower backscattering angles to 180°.

There are two more interesting features of $\beta(\theta)$ as it approaches 180° shown in Fig. 3.5. One is the large change in $\beta(\theta)$ over the one degree angle from 179° to 180°. The average change is over 50%. Considering that this large change occurs over only one degree, there is reason to suspect that $\beta(\theta)$ increases substantially from 170° to 180°, perhaps more than a factor of two. This has important implications to lidar sea truth when $\beta(180)$ is estimated from bi-static backscattering measurements. The other interesting feature is the apparent enhanced peak at 180°. Whether this is due to coherent enhanced backscattering is an open question, but the width of the peak, which is about 0.03°, suggests that it just might be.

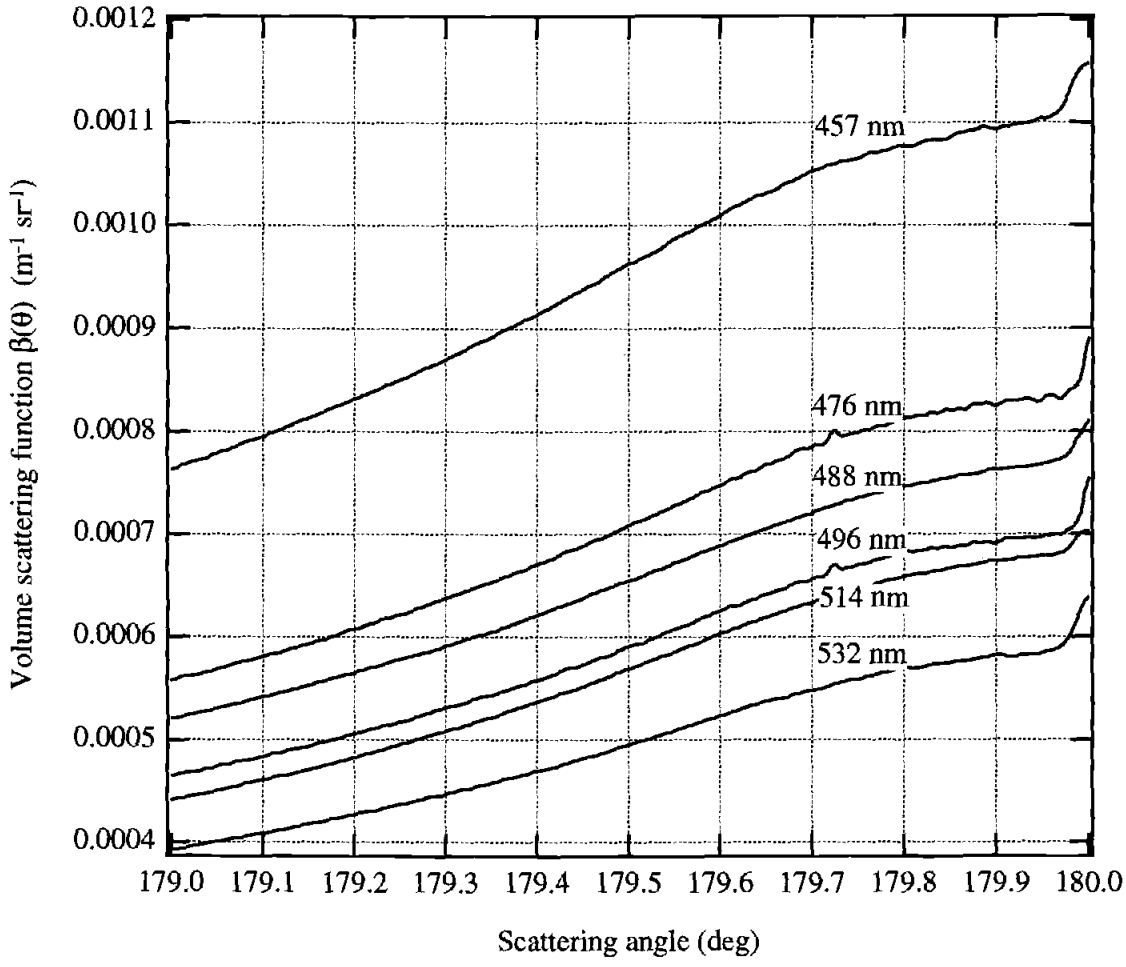

Figure 3.5 The spectral volume scattering function $\beta(\theta)$ over the angular range 179° to 180°. The average change in $\beta(\theta)$ over this one degree angular range was about 50%. The shapes of the VSF's did not appear to vary with wavelength in any significant fashion. $\beta(\theta)$ at all six wavelengths revealed a small but sharp enhancement at 180° with an angular width of approximately 0.03°.

Chapter 4

MEASUREMENT OF THE SPECTRAL ABSORPTION COEFFICIENT USING AN ISOTROPIC SOURCE IN THE OCEAN

Robert A. Maffione, Kenneth J. Voss, and Richard C. Honey

Published in *Applied Optics*, **32**, 3273-3279, June 20, 1993.

4.1 ABSTRACT

Closed-form equations that describe the vector irradiance from an isotropic source embedded in the ocean are rigorously derived from the steady-state radiative transfer equation. The equations are exact for a homogeneous medium and are believed to be an excellent approximation along the vertical axis for a plane-parallel ocean. The equations are solved for the absorption coefficient as a function of distance from the source. For clear ocean water, it is shown that vector irradiance measurements alone provide sufficient information for an accurate calculation of the absorption coefficient. Measurements in Pacific water of the vector irradiance from an isotropic source are presented and the absorption coefficient computed. The estimated value of the absorption coefficient from a linear least-squares fit to the data has a standard percent error of about 1%.

4.2 INTRODUCTION

Knowledge of the spectral absorption coefficient of oceanic waters is important to many areas of oceanography and ocean remote sensing. Yet it is still a difficult ocean-optical parameter to measure accurately and routinely. The difficulty is fundamentally due to scattering, which may cause significant errors in measurements of light attenuation from pure absorption (that is, energy conversion) processes. Nonetheless, several diverse approaches have been developed for measuring the absorption coefficient, either *in situ* or on-board ship. Some of the more notable are the reflective-tube absorption meter [*Zaneveld et al.,*, 1990] , the integrating cavity absorption meter [*Fry et*

al., 1992], photoacoustic and photothermal techniques [*Bennett et al.*, 1986; *Trees and Voss*, 1990], and *in-situ* irradiance [*Højerslev*, 1975; *Spitzer and Wernand*, 1980] and radiance [*Voss*, 1989b; *Doss and Wells*, 1992] meters which rely on Gershun's law [*Gershun*, 1939] to determine the absorption coefficient.

Gershun's law relates the divergence of vector irradiance to the product of the absorption coefficient and the scalar irradiance at a point in an absorbing and scattering medium. *Preisendorfer* [1961] independently derived Gershun's law from the steady-state radiative transfer equation (RTE) and showed that the absorption coefficient could be determined by measuring the scalar irradiance and the change with depth of the net downward (vector) irradiance. He arrived at this result by considering the ocean as a medium with negligible horizontal gradients compared with its vertical structure. Experimental methods [*Højerslev*, 1975; *Sptizer and Wernand*, 1980; *Voss*, 1989b; *Doss and Wells*, 1992] that use this result, however, depend on the temporal invariance of the submarine daylight field and are limited to the photic zone. Furthermore, the measurements can be complicated by ship shadowing [*Gordon*, 1985; *Helliwell et al.*, 1990].

Artificial light sources obviate these problems and offer several other advantages. *Duntley* [1971] used an isotropic source to measure both the absorption and attenuation coefficients of water in Lake Winnipesaukee, New Hampshire. By illuminating the rear (relative to the detector) of a table-tennis ball with a laser beam, he was able to create a spectral underwater

isotropic source. Duntley obtained the absorption coefficient by measuring the hemispherical scalar irradiance and the outward flowing irradiance from the source at long ranges. The decay of the outward irradiance provided what Duntley called a spherical diffuse attenuation coefficient that was expected to be constant at long ranges [*Preisendorfer*, 1959]. By an approximation to Gershun's law for the asymptotic region, he obtained a simple equation relating the hemispherical scalar irradiance, outward irradiance, and the spherical diffuse attenuation coefficient to the absorption coefficient.

Sorenson and Honey [1968a, 1968b] designed an absorption meter based on a different approximation from Duntley's for the decay of irradiance from an isotropic source. Whereas Duntley used an approximation valid for the asymptotic region, Sorenson and Honey used a different approximation for the decay of irradiance within a few attenuation lengths of the source. Both approximations may be obtained from the general solution derived in this paper. Sorenson and Honey argued that within a few mean free paths, the outward irradiance would decay geometrically as $1/r^2$ and exponentially as $\exp(-ar)$, where a is the absorption coefficient and r the distance from the source. Their instrument measured the outward irradiance at two separate distances from an isotropic source. Because the ratio of the two measurements cancels the radiometric units, their instrument did not require any absolute radiometric calibration. The construction and the testing of this device are described in detail by *Gilbert, et al.*, [1969].

The technique of Sorenson and Honey was recently used to measure the absorption coefficient in an experiment to test the closure property in ocean optics [*Maffione et al.*, 1991]. In this experiment, two spectral irradiance detectors looked down at an isotropic source and two looked up, away from the source. The distance between the source and detectors was varied, and measurements were taken over a range of separations from approximately 2 to 40 m. Whereas the Sorenson and Honey instrument measured the irradiance at only two distances from the source, the closure experiment provided a series of measurements of vector irradiance as a function of range. A least-squares fit of the measurements to the appropriate equation, derived in this paper, yields the absorption coefficient with an accurately quantified error. Measurements of the variation of the absorption coefficient with depth were obtained by changing the depth of the light source and detectors.

4.3 THEORETICAL DEVELOPMENT

4.3.1 Derivation of the Vector and Scalar Irradiance from an Isotropic Source Embedded in the Ocean

Nearly all techniques developed for solving the RTE treat the ocean as a horizontally homogeneous, vertically inhomogeneous optical medium. If the only source for the submarine light field is the penetration of solar radiation, then the spatial distribution of radiance in the ocean will be a function of depth only. The reduction to one spatial coordinate greatly simplifies manipulation of the RTE. For an isotropic source embedded in the ocean, however, the radiance will clearly depend on all three spatial

coordinates. It is for this reason that the most difficult standard problems encountered in radiative transfer theory are point-source problems. Aside from the approximate solutions already mentioned, some general formulations have been attempted, such as Preisendorfer's discrete-space method [*Preisendorfer*, 1965] and results from diffusion theory (see, for example,*Elliott*, [1955]).

A general, closed-form solution for the vector and scalar irradiance distribution from an isotropic source in the ocean is now derived from the RTE. It is valid at any depth, z, on axis with the source for a plane-parallel ocean and is exact everywhere for a homogeneous medium. This solution lends itself quite readily to approximations for off-axis irradiance distributions in a plane-parallel medium and to the irradiance distribution from a Lambertian (cosine) source. It is therefore applicable not only to measurements of the absorption coefficient, but also to bio-optical modeling of the irradiance distribution from bioluminescent organisms [*Gordon*, 1987].

Let $L = L\left(\mathbf{r},\hat{\xi}\right)$ denote the radiance at a point $\mathbf{r} = (x, y, z)$ in the unit vector direction $\hat{\xi}$ in a Cartesian coordinate system. Assuming no internal sources and no cross-wavelength effects, i.e., fluorescence and Raman emission, the steady-state RTE may be expressed as

$$\left(\hat{\xi}\bullet\nabla\right)L\left(\mathbf{r},\hat{\xi}\right) = -c(\mathbf{r})\,L\left(\mathbf{r},\hat{\xi}\right) + L^{*}\left(\mathbf{r},\hat{\xi}\right), \tag{4.1}$$

where the operator

$$\left(\hat{\xi}\bullet\nabla\right)=\left(\cos\theta_x,\cos\theta_y,\cos\theta_z\right)\bullet\left(\frac{\partial}{\partial x},\frac{\partial}{\partial y},\frac{\partial}{\partial z}\right) \tag{4.2}$$

takes the derivative of $L\left(\mathbf{r},\hat{\xi}\right)$ in the direction $\hat{\xi}$. The first term on the right represents the loss of radiance along an infinitesimal path length in the direction $\hat{\xi}$, and $c(\mathbf{r})$ is the beam attenuation coefficient at point $\mathbf{r}$. The last term on the right is the so-called path function, which gives the increase in radiance per unit path length that is due to scattering into the direction $\hat{\xi}$ from all other directions $\left\{\hat{\xi}'\right\}$. If $\beta\left(\mathbf{r},\hat{\xi}\bullet\hat{\xi}'\right)$ denotes the volume scattering function and $d\Omega\left(\hat{\xi}'\right)$ denotes the infinitesimal solid angle in the direction $\hat{\xi}'$, then the path function is given explicitly by

$$L^*\left(\mathbf{r},\hat{\xi}\right)=\int_{4\pi}L\left(\mathbf{r},\hat{\xi}'\right)\beta\left(\mathbf{r},\hat{\xi}\bullet\hat{\xi}'\right)d\Omega\left(\hat{\xi}'\right). \tag{4.3}$$

The quantities L, c, and β are assumed to be spectral, although their explicit dependence on wavelength is not shown.

Integrating Eq. 4.1 over 4π sr gives the general form of Gershun's equation:

$$-\nabla\bullet\mathbf{E}(\mathbf{r})=a(\mathbf{r})E_0(\mathbf{r}), \tag{4.4}$$

Here a is the spectral absorption coefficient and E_0 is the scalar irradiance, given by

$$E_0(\mathbf{r})=\int_{4\pi}L\left(\mathbf{r},\hat{\xi}\right)d\Omega\left(\hat{\xi}\right). \tag{4.5}$$

Note that, in general, the vector irradiance $\mathbf{E}$ has three components: E_x, E_y, E_z, where

$$
\begin{aligned}
E_x &= 2\pi \int_0^{\pi} L\left(\mathbf{r},\hat{\xi}\right)\cos\theta_x \sin\theta_x d\theta_x \\
&= 2\pi\left[\int_0^{\pi/2} L\left(\mathbf{r},\hat{\xi}\right)\cos\theta_x \sin\theta_x d\theta_x - \int_{\pi/2}^{\pi} L\left(\mathbf{r},\hat{\xi}\right)\left|\cos\theta_x\right|\sin\theta_x d\theta_x\right] \\
&= E_{+x} - E_{-x},
\end{aligned}
\tag{4.6}
$$

etc.

Thus E_x represents the difference between the irradiance that flows in the positive x direction and the irradiance that flows in the negative x direction.

Under the assumption of a horizontally homogeneous ocean illuminated by solar radiation, the partial derivatives $\partial E_x/\partial x$ and $\partial E_y/\partial y$ in Eq. 4.4 will be zero, and Gershun's equation simplifies to

$$
-\frac{\partial E_z(z)}{\partial z} = a E_0(z), \tag{4.7}
$$

which is the result used most often in ocean optics. In principle then, the absorption coefficient can be determined by measuring the change in the vector irradiance with depth and the scalar irradiance. In practice it is quite difficult, and very little data have been published on the measured spectral absorption coefficient using Gershun's law [Eq. 4.7]. Significant errors can be introduced in computing the derivative of E_z, especially in regions where the water is not vertically homogeneous. Measurements are restricted to the daytime and to depths where the ambient light is strong enough for the sensors to detect. Ship shadowing is another problem that has already been mentioned. But a major reason why researchers do not routinely apply Gershun's law is that the scalar irradiance is rarely measured. Sometimes,

however, the scattering properties of the water are estimated, which then allows one to estimate the absorption coefficient from Gershun's law.

For an isotropic source embedded in the ocean, the divergence of the vector irradiance **E** will be a function of all three spatial coordinates. Assuming that the isotropic source is the only source for the light field, a natural coordinate system for its description are spherical coordinates. The three components of the vector irradiance are then E_r, E_θ, and E_ϕ, which correspond to the respective unit orthogonal directions, $\hat{\mathbf{r}}$,$\hat{\theta}$, and $\hat{\phi}$, shown in Fig. 4.1. The source is taken to be at the origin, and the z axis is the vertical direction in the ocean. In this coordinate system, Gershun's law (Eq. 4.4) appears as

$$-aE_0 = \frac{1}{r^2}\frac{\partial\left(r^2E_r\right)}{\partial r} + \frac{1}{r\sin\theta}\frac{\partial\left(\sin\theta E_\theta\right)}{\partial\theta} + \frac{1}{r\sin\theta}\frac{\partial E\varphi}{\partial\varphi}. \tag{4.8}$$

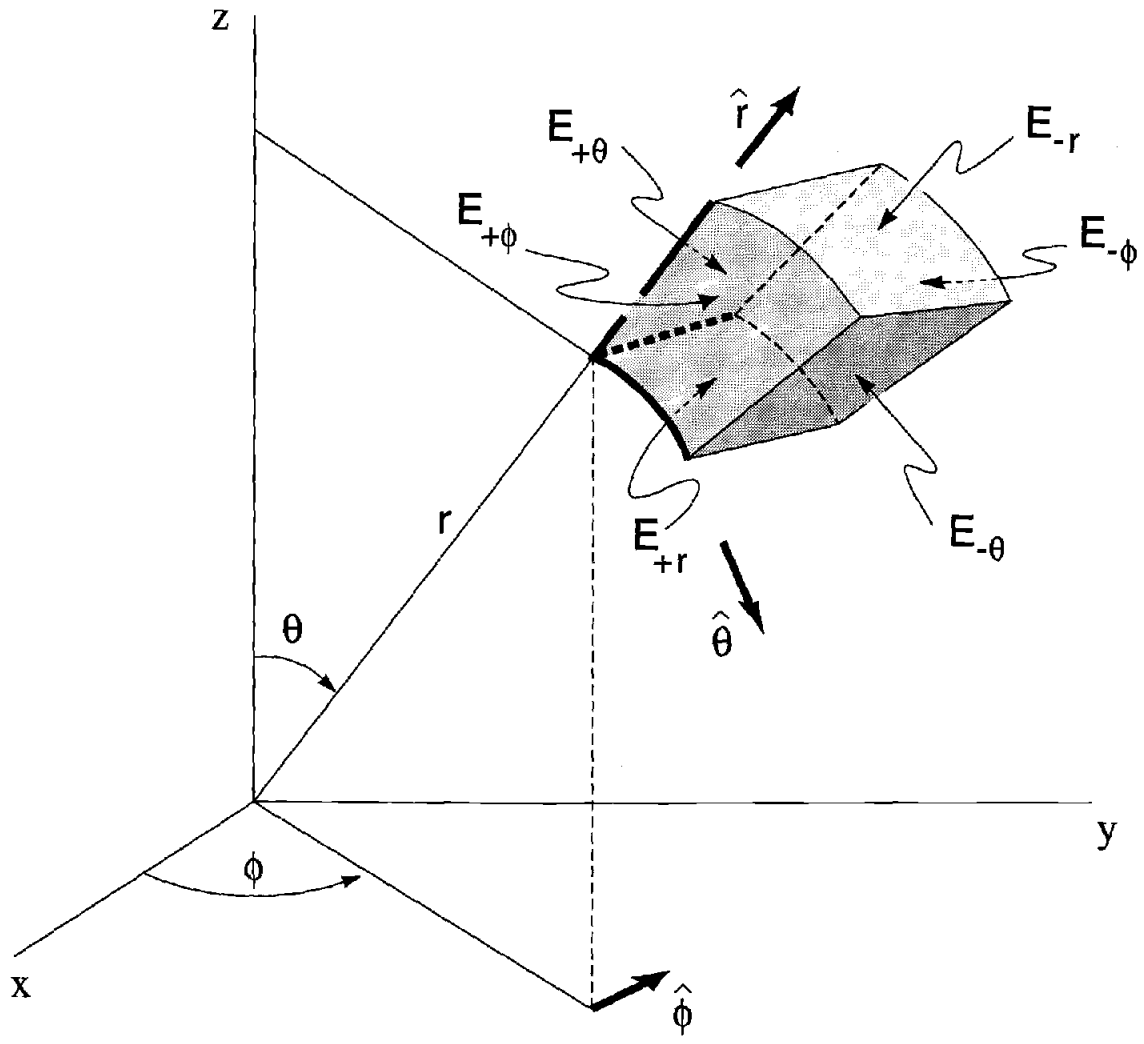

Figure 4.1 Spherical components of vector irradiance. The three components of the vector irradiance are the differences of the irradiances incident on the opposing faces

Clearly, for a plane-parallel medium in which the planes are oriented perpendicular to the z axis, E_φ and $\partial E_\varphi / \partial \varphi$ must be zero for all r, θ, and φ. Along the z axis ($\theta = 0$), it should also be clear that $E_\theta = 0$. Eq. 4.8 then simplifies to

$$-aE_0 = \frac{1}{r^2}\frac{\partial\left(r^2E_r\right)}{\partial r} + \frac{1}{r}\frac{\partial E_\theta}{\partial \theta} = \frac{\partial E_r}{\partial r} + \frac{1}{r}\left(2E_r + \frac{\partial E_\theta}{\partial \theta}\right). \tag{4.9}$$

In all practical cases of interest, $\partial E_\theta/\partial\theta$ will be negligible compared to E_r, and thus

$$-aE_0 = \frac{\partial E_r}{\partial r} + \frac{2E_r}{r}, \tag{4.10}$$

which is everywhere exact for a homogeneous medium and an excellent approximation along the vertical axis for a plane-parallel ocean.

With the introduction of the radial average cosine,

$$\bar{\mu}_r(r) = \frac{E_r(r)}{E_0(r)}, \tag{4.11}$$

which is similar to the commonly used "vertical" average cosine, Eq. 4.10 may be expressed in the form

$$\frac{dE_r(r)}{E_r(r)} = -\frac{a(r)}{\bar{\mu}_r(r)}dr - \frac{2}{r}dr. \tag{4.12}$$

Integrating from r_0 to r and solving for $E_r(r)$ gives

$$E_r(r) = E_r(r_0)\frac{\exp\left[-\int_{r_0}^{r}\frac{a(r)}{\bar{\mu}_r}dr\right]}{\left(r/r_0\right)^2}. \tag{4.13}$$

If $R \le r_0 << 1/c$, where R is the radius of the source, then the initial condition, $E_r(r_0)$, is

$$E_r(r_0) = \frac{\Phi_{r_0}}{4\pi r_0^2}, \tag{4.14}$$

where Φ_{r0} is the total radiant power at r_0. Thus, for $r = z$, i.e., $\theta = 0$, the solution for the vector irradiance from an isotropic source embedded in a plane-parallel ocean is

$$E_r(z) = \frac{\Phi_{z_0}}{4\pi z^2} \exp\left[-\int_{z_0}^{z} \frac{a(z)}{\overline{\mu}_r(z)} dz\right]. \tag{4.15}$$

Consider now a homogeneous, *nonscattering* medium. Then a is constant, and Eq. 4.15 simplifies to

$$E_r(z) = \frac{\Phi_{z_0}}{4\pi z^2} \exp(-a\Delta z) \tag{4.16}$$

where $\Delta z = z - z_0$. The inclusion of scattering gives

$$\begin{aligned} E_r(z) &= \frac{\Phi_{z_0}}{4\pi z^2} \exp\left[-a\int_{z_0}^{z} \frac{dz}{\overline{\mu}_r(z)}\right] \\ &= \frac{\Phi_{z_0}}{4\pi z^2} \exp(-a\bar{z}) \end{aligned} \tag{4.17}$$

where $\bar{z}$ is Schellenberger's mean light path [*Schellenberger*, 1965], viz.,

$$\bar{z} = \int_{z_0}^{z} \frac{dz}{\overline{\mu}(z)}, \tag{4.18}$$

which appears in Stavn's three-parameter model [*Stavn*, 1982] and is a similarly useful concept in the present context. A comparison of Eqs. 4.17 and 4.18 shows that the net effect of scattering on the irradiance is completely described by the mean light path $\bar{z}$. For any scattering medium, $\overline{\mu}_r < 1$ and thus $\bar{z} > \Delta z$, which means that there will be a decrease in the net irradiance at z by a factor $\exp[-a(\bar{z} - \Delta z)]$. Another way of expressing this is to rewrite Eq. 4.17 as

$$E_r(z) = \frac{\Phi_{z_0}}{4\pi z^2} \exp\left[-a(\Delta z + \delta z)\right], \tag{4.19}$$

where $\delta z = \bar{z} - \Delta z$ is defined as the mean increase in the light path due to scattering (see Figure 4.2).

4.3.2 Solution for the Absorption Coefficient

Equation 4.12 is easily solved for $a(z)$, giving

$$\begin{aligned} a(z) &= \bar{\mu}_r(z)\left[-\frac{1}{E_r(z)}\frac{dE_r(z)}{dz} - \frac{2}{z}\right] \\ &= \bar{\mu}_r(z)\left[K_{E_r}(z) - \frac{2}{z}\right], \end{aligned} \tag{4.20}$$

where K_{Er} is defined as the diffuse attenuation coefficient for vector irradiance from an isotropic source. This follows the usual convention for defining irradiance attenuation coefficients, viz,

$$K_{E_r}(z) \equiv \frac{-1}{E_r(z)}\frac{dE_r(z)}{dz}.$$

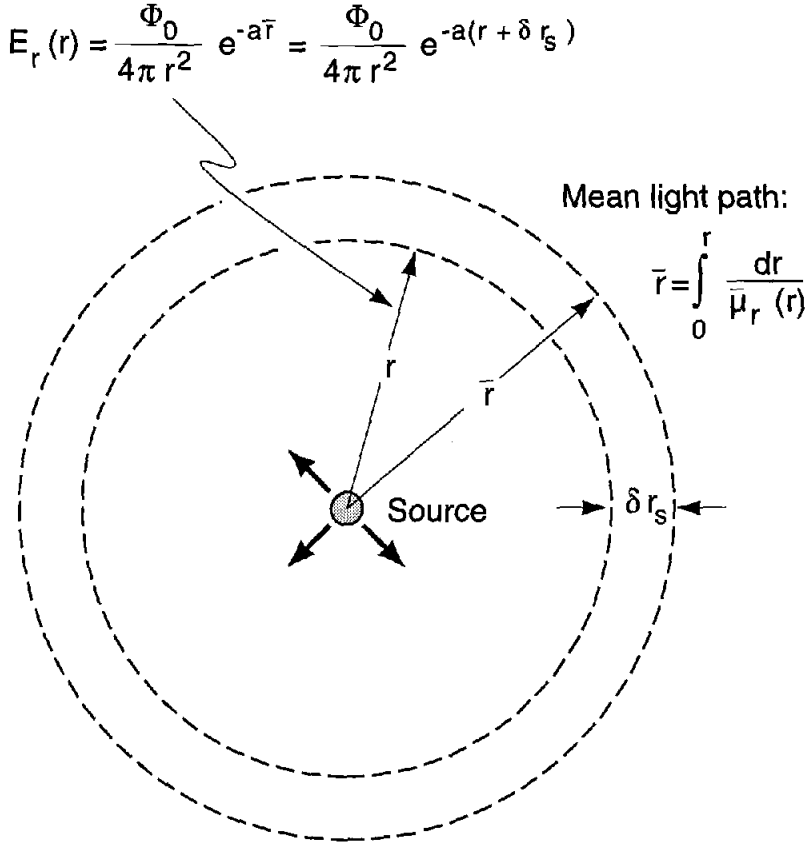

Figure 4.2 Vector irradiance from isotropic souce embedded in a homogeneous scattering and absorbing medium.

From the definition of the irradiance attenuation coefficient, the vector irradiance may be expressed as

$$E_r(z) = E_r(z_0)\exp\left[-\int_{z_0}^{z} K_{E_r}(z)dz\right]. \tag{4.21}$$

Solving Eq. 4.20 for K_{E_r} gives

$$K_{E_r} = \frac{a(z)}{\bar{\mu}_r(z)} + \frac{2}{z}. \tag{4.22}$$

Substituting this expression into Eq. 4.21 gives the same result as Eq. 4.13 for the vector irradiance, as it should. Note that for a homogeneous ocean, as $z \to \infty$, $K_{E_r} \to K_E = a/\bar{\mu}$ where K_E is the well-known diffuse attenuation

coefficient for vector irradiance defined for solar, i.e. plane wave, illumination.

Since the light field from an isotropic source approaches a plane wave in the far field, all the results derived here must approach, at large distances from the source, the well-known relations in ocean optics that are derived for plane waves incident upon the water's surface. Consider again Eq. 4.20. As z increases, the second term on the right eventually becomes negligible compared to K_{E_r}, resulting in the approximation

$$a(z) \cong \overline{\mu}_r(z) K_{E_r}(z), \tag{4.23}$$

which is identical to Preisendorfer's solution [*Preisendorfer*, 1961] for a plane-parallel ocean illuminated by solar radiation. Again for a homogeneous ocean, $K_{E_r} \to K_E \to K_\infty$, where K_∞ is the asymptotic diffuse attenuation coefficient. Because the equivalencies are achieved at large distances from the source, theoretical proofs [*Preisendorfer*, 1959; *Højerslev and Zaneveld*,, 1977] of the existence of a submarine asymptotic daylight field apply just as well to an isotropic source embedded in the ocean. From Eq. 4.20 it is seen that the condition for the asymptotic field from an isotropic source in the ocean is $2/K_{Er} << z$. This condition will always be met for large enough values of z, since K_{Er} is bounded and, for homogeneous water at least, eventually approaches a constant. Because the light field from an isotropic source is truly axially symmetric, Zaneveld and Pak's derivation [*Zaneveld and Pak*, 1972], which relates the asymptotic radiance distribution and its derivative to the beam attenuation coefficient and the volume scattering function, also applies.

This opens up the possibility for testing these theories. Furthermore, measurements in homogeneous water can more easily be made since the source-receiver system can be lowered to depths where the water column between the source and receiver is found to be homogeneous.

Experimentally, measurements are taken at discrete points z_n, so that $K_{Er}(z_n)$ would be calculated from

$$K_{E_r}(z_n) = \frac{\ln\left[\frac{E_r(z_{n-1})}{E_r(z_{n+1})}\right]}{z_{n+1} - z_{n-1}}, \tag{4.24}$$

where $z_{n+1} > z_n > z_{n-1}$. The operational form of Eq. 4.20 is then

$$a(z_n) = \overline{\mu}_r(z_n)\left\{\frac{\ln\left[\frac{E_r(z_{n-1})}{E_r(z_{n+1})}\right]}{z_{n+1} - z_{n-1}} - \frac{2}{z_n}\right\}. \tag{4.25}$$

To determine the absorption coefficient at a point z_n, three physical quantities must be measured: the vector irradiance E_r, the average cosine $\overline{\mu}_r$, and the distance z between the source and detectors. Measuring vector irradiance and distance are straightforward and can be performed accurately [*Maffione et al.*, 1991]. One way to determine $\overline{\mu}_r$ is to measure the scalar irradiance E_0 and compute the ratio E_r/E_0. Scalar irradiance meters, however, are much more difficult to construct and use [*Højerslev*, 1975; *Spitzer and Wernand*, 1980] and are subject to various sources of error. The average cosine could be estimated from measurements of the point spread function [*Voss and Chapin*, 1990] (PSF) from the isotropic source. Since the PSF is the

radiance distribution, $L(z, \theta)$, normalized to the source power, $\bar{\mu}_r$ is estimated from

$$\bar{\mu}_r(z) \cong \frac{\int_{\varepsilon \to 0}^{\theta_{max}} L(z,\theta)\cos\theta \sin\theta \, d\theta}{\int_{\varepsilon \to 0}^{\theta_{max}} L(z,\theta)\sin\theta \, d\theta}. \tag{4.26}$$

The ratio cancels the radiometric units, so that no absolute calibration of the camera and source is necessary. Measurements by *Voss and Chapin* [1990] and *Maffione et al.*, [1991] of the PSF in ocean waters show that the PSF falls off by more than 3 orders of magnitude within the first 10°, which is expected since scattering in the ocean is highly peaked in the forward direction [*Kullenberg*, 1974]. Measurements by *Wilson* [1979] of the radiance distribution from a point source in an aluminum hydroxide suspension show that the PSF continues to drop off by another 2 orders of magnitude from 10 to ~ 50°. Thus an accurate estimate of $\bar{\mu}_r$ can be obtained by measuring the PSF over forward angles, i.e., $\theta_{max} \leq 90°$, except perhaps in murky water or at asymptotic distances where a larger fraction of the scattered light is contained at larger angles. Underwater camera systems have become a well-developed technology [*Voss*, 1989b; *Maffione et al.*, 1991; *Voss and Chapin*, 1990; *Voss*, 1989a] which in many circumstances makes their use preferable to that of scalar irradiance meters because the measurement of the radiance distribution provides additional information about the optical properties of the water.

To the authors' knowledge, no data have been published on $\bar{\mu}_r(z)$, as a function of the distance z from the source. Nonetheless, its limiting values

can be inferred. From its definition, it is clear that $\bar{\mu}_r(z) \to 1$ as $z \to z_0$. In clear homogeneous water, $\bar{\mu}_r(z)$ should gradually and monotonically decrease and must eventually approach its asymptotic value as $z \to \infty$. In the asymptotic limit, K_{Er} must approach K_∞, the asymptotic diffuse attenuation coefficient. With the Wilson-Honey relationship [*Wilson*, 1979] for the asymptotic diffuse attenuation coefficient, $K_\infty = c - \frac{5}{6}b$, where b and c are the total scattering and the beam attenuation coefficients, respectively, the following equation is easily derived from Eq. 4.23:

$$\bar{\mu}_\infty = \frac{1-\omega_0}{1-\frac{5}{6}\omega_0}, \tag{4.27}$$

where $\omega_0 = b/c$ is the single scattering albedo. Measurements of the optical properties of ocean waters at 530 nm by *Petzold* [1972] show that ω_0 varies from ~ 0.3 in the clearest waters to ~ 0.9 in murky (e.g., harbor) waters. $\bar{\mu}_\infty$ is thus bounded approximately by $0.4 < \bar{\mu}_\infty < 0.9$, with the lower value for murky waters and the upper value for the clearest waters.

Since, for clear ocean water, $\bar{\mu}_\infty$ is ~ 0.9, then it should be expected that $\bar{\mu}(z)$, which starts out at 1 at z_0, will remain close to 1 for at least several attenuation lengths. Clear ocean water measurements of the vector irradiance from an isotropic source will therefore decay, according to Eq. 4.16, to a good approximation over distances extending to several attenuation lengths, assuming the water column is relatively homogeneous, i.e., a is constant.

Let $\tilde{E} = k_e E$ denote the signal from the irradiance detector in, say, digital counts or volts, where k_e determines the response to the irradiance E at the detector. For all practical purposes, z_0 may be taken to be at the origin, and Eq. 4.16 may then be expressed in the form

$$\tilde{E} = \frac{k_e \Phi_0 \exp(-az)}{4\pi z^2}, \tag{4.28}$$

where Φ_0 is now the total power emitted by the source. Multiplying through by z^2 and taking the natural logarithm gives

$$\ln\left[z^2 \tilde{E}(z)\right] = \ln\left(\frac{k_e \Phi_0}{4\pi}\right) - az. \tag{4.29}$$

A plot of the left-hand side versus z yields a line whose slope is the negative of the absorption coefficient. Because the offset, $\ln(k_e \Phi_0 / 4\pi)$, is not needed to determine the slope, no absolute calibration is necessary.

At large distances from the source or in water where scattering is high, z in Eq. 4.29 should be replaced by $\bar{z}$, Schellenberger's mean light path (Eq. 4.18).But, this requires knowing $\bar{\mu}_r(z)$. In many situations, however, the error in using z instead of $\bar{z}$ in estimating a with Eq. 4.29 will be small since $\bar{z} = z + \delta z = z(1 + \delta z / z)$. That is, even though δz increases as z increases, the ratio $\delta z / z$ remains small.

4.4 DATA

Measurements of the vector irradiance $E_r(z)$ from an isotropic source were made in waters off the coast of southern California during the Ocean

Optics cruise in August 1990, sponsored by the Office of Naval Research. The experimental technique and instrumentation are described in *Maffione et al.* [1991] and *Brown et al.* [1991]. In addition to the vector irradiance measurements, simultaneous measurements of the apparent radiance of the source and the PSF were made. The decay of the apparent radiance of the source provided the beam attenuation coefficient, and the PSF gave information on the forward-scattering properties of the water.

Measurements were made at a wavelength of 465 ± 15 nm. The data presented here contain the largest source-to-detector separation profile, which is from the last run on August 26. In this run, the detectors and cameras were held at a depth of approximately 72 m and the distance to the isotropic source was varied by lowering the source from ~ 78 to 140 m. Measurements were taken at approximately 5 m increments.

Figure 4.3 shows a log-linear profile of the vector irradiance. The bottom abscissa is the distance between the source and detectors, and the top abscissa shows the depth of the source. The units for the irradiance are in digital counts. The absorption coefficient a and the offset term $\ln(k_e\Phi_0/4\pi)$ were calculated from a linear least-squares fit to the data using Eq. 4.29. The curve in the plot was computed from Eq. 4.16, with the values of the linear fit for a and $k_e\Phi_0/4\pi$. The absorption coefficient, which is given by the absolute value of the slope, was computed to be 0.0337 m^{-1}. The standard error of the slope was 0.0003 m^{-1}. This gives a percentage error in a of ~ 1%.

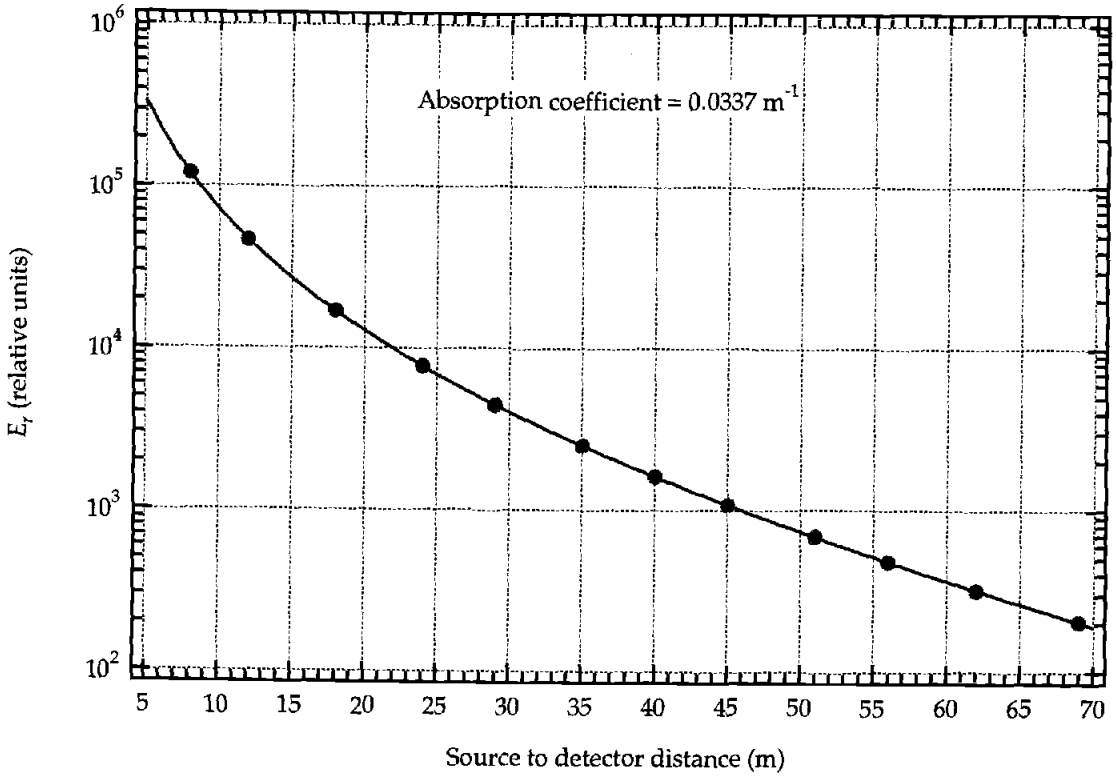

Figure 4.3 Vector irradiance measurements from an isotropic source taken on 26 August 1990, off the coast of southern California.

From measurements of the apparent radiance of the source, which were made with a CCD camera [*Maffione et al.*, 1991], the beam attenuation coefficient was found to be $c = 0.077$ m^{-1}. Therefore $b = c - a = 0.043$ m^{-1}, and thus the single scattering albedo, $\omega_0 = b/c$, was 0.56, which gives $\bar{\mu}_\infty \cong 0.8$ from Eq. 4.27. The change in $\bar{\mu}_r(z)$ from its value of 1 at the source was therefore probably small, which is one reason why there was such a good fit to the data. Nonetheless, it would be quite interesting, in future experiments, to determine $\bar{\mu}_r(z)$ and its effect on the computation of a.

4.5 SUMMARY AND CONCLUSIONS

Closed-form solutions for the vector irradiance from an isotropic source embedded in the ocean were derived from the RTE. The solutions are exact everywhere for a homogeneous optical medium and are believed to be an excellent approximation along the vertical axis in a plane-parallel ocean, although this has yet to be rigorously demonstrated. The vector irradiance equations were solved for the absorption coefficient. Operational equations for the absorption coefficient were also given. The appropriate solution depends on the experimental setup and assumptions about the clarity and homogeneity of the water column.

Measurements of the vector irradiance from an isotropic source were performed off the coast of southern California, and some of the data were presented. The instrumentation used to carry out the measurements consisted of upward- and downward-facing irradiance detectors, a CCD camera system, and an isotropic source. Neither an absolute radiometric calibration nor an intercalibration between the detectors and camera were needed. For clear, homogeneous water, it was shown that irradiance measurements only are required to determine the absorption coefficient accurately. The absorption coefficient was computed from a profile of the vector irradiance. The percent error of the estimate was less than 1%.

Chapter 5

THE AVERAGE COSINE DUE TO AN ISOTROPIC LIGHT SOURCE IN THE OCEAN

Robert A. Maffione and Jules. S. Jaffe

Journal of Geophysical Research, **100**, 13,179-13,192, 1995.

5.1 ABSTRACT

The average cosine, $\overline{\mu}$, of the light field created by an isotropic point source (IPS) embedded in a homogeneous ocean is investigated with a Monte Carlo model. Two volume scattering functions (VSF's) are used in the model, taken from *Petzold* [1972] to compute the radiance distributions at various distances from the source. The simulated radiance distributions are compared with measurements of the point spread function made at Lake Pend Oreille, Idaho, during the 1992 optical closure experiment. An analytic model is presented for $\overline{\mu}$ which is valid to at least 15 optical lengths from the source. The model shows that the mean light path, derived from $\overline{\mu}$, is a strong function of the single scattering albedo and the VSF. We found that errors in estimating the absorption coefficient by neglecting the increase in the mean light path, which is due to scattering, vary between 5% and 12% for nearly all natural waters. A mathematical proof is given that $\overline{\mu} \to 1$ as the distance to the IPS goes to zero. An analytic expression is derived for $\overline{\mu}$ close to a finite diffuse-isotropic source which shows that $\overline{\mu}$ approaches one as the distance decreases, but at extremely close distances, $\overline{\mu} \to 1/2$ as the distance to the surface of the source goes to zero. At distances beyond one attenuation length, for finite sources small compared to an attenuation length, $\overline{\mu}$ behaves essentially as it would for a point source. An asymptotic model for $\overline{\mu}$ as a function of the single scattering albedo is given with coefficients that depend on the VSF. Model results and comparisons with measured PSF's, reveal the surprising result that the light field from an

embedded isotropic point source in the ocean does not exhibit asymptotic behavior as far as 15 attenuation lengths from the source.

5.2 INTRODUCTION

The light field due to an isotropic point source (IPS) embedded in the ocean is interesting to study because this light field, under suitable mathematical transformations, provides a wealth of information about the optical properties of the water. To the extent that the ocean may be thought of as a linear optical medium, the radiance distribution at each point in the water due to an embedded IPS is the optical impulse response (OIR) of the medium. The OIR is commonly referred to as the point spread function (PSF), although the PSF for imaging systems is usually defined as the (output) radiance distribution due to a point Lambertian source. In this case, the transformation of any input light field by the optical system is given by the spatial convolution of the input light field with the OIR. The ocean laser community defines the PSF similarly because of its equivalence to the beam spread function (BSF), which is the angular irradiance distribution due to a unidirectional light beam [*Mertens and Replogle*, 1977]. In the small-angle range (less than 10 °), both the isotropic- and Lambertian-source defined PSF's are empirically nearly equal. In general, however, they should be distinguished.

Aside from its powerful use as the OIR of an optical medium, the light field due to an IPS embedded in the ocean can, in principle, be mathematically transformed to yield all of the inherent optical properties (IOP's) of the medium. *Sorenson and Honey* [1968], for example, conjectured that the beam attenuation,

volume absorption, and backward scattering coefficients can all be determined from radiance and irradiance measurements of an IPS. Sorenson and Honey's conjectures were experimentally verified as good approximations [*Honey and Maffione*, 1992; *Maffione*, 1993; *Maffione and Honey*, 1991; *Maffione et al.*, 1991, 1993]. *Wells* [1969] first presented the transformation of the PSF to the volume scattering function (VSF) in the small-angle approximation. Although Wells' transformation to the VSF has yet to be experimentally tested in the sense of closure, it was recently numerically tested and found to be accurate within the small-angle scattering limit up to about six attenuation lengths [*Jaffe*, 1995].

To the authors' knowledge, the only known exact transformation to an inherent optical property from an IPS light field was presented by *Maffione et al.* [1993]. They showed that the absorption coefficient a could be obtained exactly from the scalar irradiance and divergence of the vector irradiance by simply transforming *Gershun's* [1936] Equation to spherical coordinates. For homogeneous water the problem reduces to one spatial coordinate, the radial distance r from the source, and the resulting solution is given by

$$a = \bar{\mu}_r(r)\left[K_r(r) - \frac{2}{r}\right], \tag{5.1}$$

where

$$K_r(r) = \frac{-1}{E_r(r)}\frac{dE_r(r)}{dr} \tag{5.2}$$

is defined as the radial attenuation coefficient for net radial irradiance E_r and

$$\bar{\mu}_r(r) = \frac{E_r(r)}{E_0(r)} \tag{5.3}$$

is defined as the radial average cosine. The net radial irradiance is the difference between the irradiance flowing away from the source and the irradiance flowing in toward the source due to scattering. E_r is analogous to the vertical component of the vector irradiance in a Cartesian coordinate system; E_0 is the scalar irradiance. It is understood that all quantities are spectral. Henceforth, the subscript r and the adjective radial will be omitted. Comparing Eq. 5.1 to the analogous form of Gershun's Equation,

$$a = \bar{\mu}(r)K(r) \tag{5.4}$$

reveals that Gershun's Equation is actually a special case of the more general form Eq. 5.1 when $r \to \infty$. In other words, Gershun's Equation is the far-field approximation where the electromagnetic waves are considered plane waves and horizontal gradients in the electromagnetic field are neglected.

The average cosine, $\bar{\mu}$, is an apparent optical property (AOP) since it depends on the structure of the light field. The importance of Gershun's Equation 5.4 is that the product of the average cosine with another AOP, the irradiance attenuation coefficient K, yields the absorption coefficient, an IOP which depends only on the physical properties of the water. In the more general case Eq. 5.1, the absorption coefficient is given by the product $\bar{\mu}K$ minus the geometric reduction due to the spherically expanding light field of an IPS, but this geometric term also contains $\bar{\mu}$. Thus, the average cosine is fundamental to understanding how the ocean transforms the light field and how that transformation is related to the absorption of light by the water.

In this paper we investigate the behavior of $\bar{\mu}$ from the radiance distribution due to an IPS embedded in the ocean using a Monte Carlo (MC) model. The computed radiance distributions are compared with PSF's that were measured in Lake Pend Oreille during the Office of Naval Research (ONR) sponsored optical closure experiment in April-May, 1992 [*Maffione*, 1993; *Zaneveld and Pegau*, 1993]. Analytical results are derived on the limiting values of $\bar{\mu}$ both for the case when $r \to 0$ and when $r \to \infty$. We also discuss the case of a finite source. A simple exponential equation is presented as a model for $\bar{\mu}$ which is valid to at least 15 optical lengths from the source. The $\bar{\mu}$ model is used to compute the mean light path, defined by Eq. 5.17, which is then used to accurately calculate the absorption coefficient. Errors in neglecting the increase in the mean light path are investigated.

5.3 APPROACH

The MC model uses standard Monte Carlo techniques for computing photon propagation in an absorbing and scattering medium (see, for example, *Mobley* [1994, Chapter 6]). Spherical polar coordinates are most appropriate for describing the radiance distribution L due to an IPS situated at the origin, as shown in Figure 5.1. In homogeneous water, the symmetry of the radiance distribution at all points in space allows L to be specified as a function of one independent angular variable, θ', (ref. Figure 5.1). Along any radial path from the point source, θ' is defined as the angle that the radiance direction vector, $\hat{\xi}$, makes with the radial line from the IPS to the point where the radiance is

specified. If, for example, a radiometer is pointing directly at the source, it is measuring the radiance in the direction $\theta' = 0$. The symmetry of the problem also allows L to be specified as a function of the distance r from the source; the radial direction from the origin is irrelevant.

Making use of these symmetry properties in the Monte Carlo simulations greatly reduces computation time. Computing the radiance distribution at a point in space does not require counting only those photons which cross that point (strictly speaking, a small area). All of the photons which cross an imaginary sphere of radius r are tallied according to the direction θ' that they are heading when they cross the sphere to compute the radiance distribution $L(r,\theta')$. Because it does not matter where on the sphere the photons cross, by reciprocity

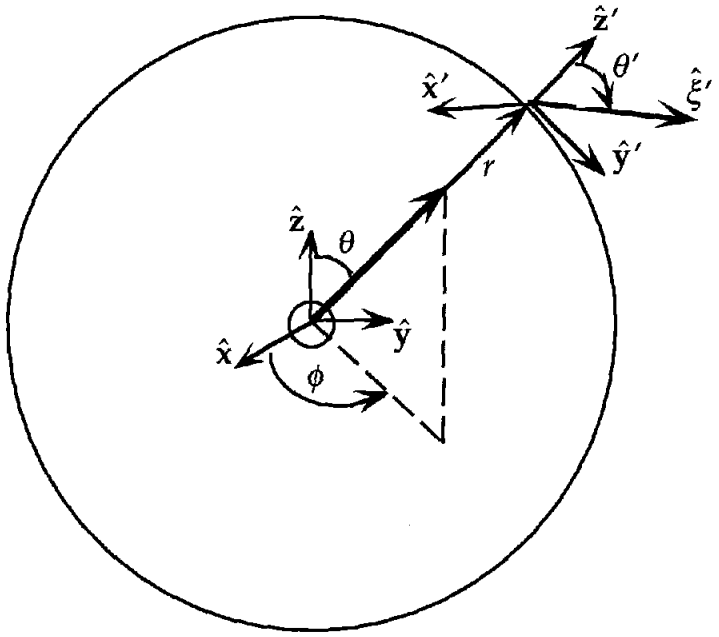

Figure 5.1 Coordinate system for the Monte Carlo model that computes the radiance distribution due to an isotropic point source at the origin.

it does not matter in which direction the photons are initially launched. A computational step is saved by launching all of the photons in one direction. This simulation is thus analogous to an experiment where the radiance distribution at all points a distance r from a collimated source is measured and then summed or integrated to produce the radiance distribution that would have been measured at a single point a distance r from an isotropic source. The results are identical because an isotropic source is equivalent to a collimated source being pointed in all directions at once.

To simplify the notation, we will henceforth drop the prime on the angular variable θ., keeping in mind that we are referring to the polar angle in the prime coordinate system shown in Figure 5.1. Then $\overline{\mu}$ is given by

$$\begin{aligned}\overline{\mu}(r) &= \frac{\int_0^{\pi} L(r,\theta)\cos\theta\sin\theta d\theta}{\int_0^{\pi} L(r,\theta)\sin\theta d\theta} \\ &= \frac{\int_0^{\pi/2} L(r,\theta)\cos\theta\sin\theta d\theta - \int_{\pi/2}^{\pi} L(r,\theta)|\cos\theta|\sin\theta d\theta}{\int_0^{\pi/2} L(r,\theta)\sin\theta d\theta + \int_{\pi/2}^{\pi} L(r,\theta)\sin\theta d\theta} \\ &= \frac{E_+(r) - E_-(r)}{E_{0+}(r) + E_{0-}(r)}\end{aligned} \tag{5.5}$$

where the plus and minus subscripts denote the forward and backward hemisphere irradiances, respectively, defined by the limits of integration of the separate terms in the second equation. Because the reduction in computation time by excluding the calculation of the radiance distribution in the backward hemisphere is significant, we chose to compute the radiance distribution only from 0 to $\pi/2$. Our estimation of $\overline{\mu}$,

$$\overline{\mu} \equiv \frac{\int_0^{\pi/2} L(\theta)\cos\theta\sin\theta d\theta}{\int_0^{\pi/2} L(\theta)\sin\theta d\theta} = \frac{E_+}{E_{0+}} \tag{5.6}$$

therefore assumes that $E_+ >> E_-$ and $E_{0+} >> E_{0-}$. The fact that the VSF's of ocean water are highly peaked in the forward direction indicates that this ought to be an excellent approximation. Furthermore, measurements [*Honey and Maffione*, 1992; *Maffione*, 1993; *Maffione et al.*, 1991, 1993] show that $E_-/E_+ < 0.01$ for various natural waters. Bear in mind that this is an excellent approximation for irradiances due to an IPS and is not meant to apply to comparisons of downwelling with upwelling irradiances due to solar illumination of the ocean.

For the present study we define four cases which we refer to as deep, coast, bay, and milk. The associated volume absorption, total scattering, and beam attenuation coefficients are listed in Table 5.1. These values for a, b, and c, respectively, were chosen to represent what could be considered typical, at a wavelength of 530 nm, for clear ocean water, coastal water, bay or harbor water,

Table 5.1 Optical Parameters for Monte Carlo Simulations

Type	a m^{-1}	b m^{-1}	c m^{-1}	ω_0 b/c
Deep	0.08	0.08	0.16	0.5
Coast	0.10	0.15	0.25	0.6
Bay	0.30	1.20	1.50	0.8
Milk	0.06	1.14	1.20	0.95

and extremely turbid water dominated by scattering. The single scattering albedo, $\omega_0 = b/c$, for these four cases range from 0.5 to 0.95, which encompasses nearly all natural water.

Two different volume scattering functions were used to investigate the dependence of the radiance distribution and $\bar{\mu}$ on the VSF. Both VSF's are from *Petzold* [1972], which were measured at 530 nm with a bandwidth of 100 nm; one is referred to as station 8 (AUTEC - test 161, July 13, 1971) and the other as station 11 (HAOCE, August 5, 1971). These two VSF's were chosen because they yield significantly different scattering phase functions for the natural waters measured by Petzold. Figure 5.2a shows the VSFs, and Figure 5.2b shows the cumulative scattering probability functions for these two stations. The derivative of the scattering probability function is the scattering phase function. Note that the station 11 VSF has a higher slope than the station 8 VSF, and this higher slope results in a higher photon scattering probability function over all angles.

For each of the four water types given in Table 5.1, radiance distributions were computed at seven discrete distances from the source corresponding to optical lengths of 0.1, 0.5, 1, 3, 6, 10, and 15. Since the attenuation coefficient c is constant, the optical path length τ is defined as

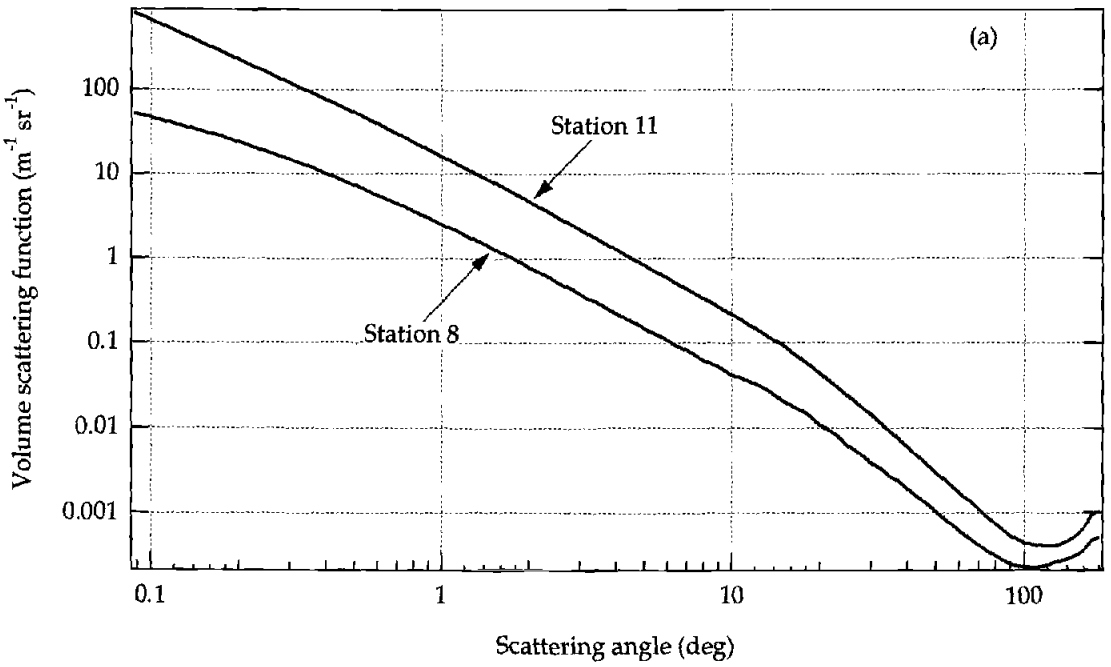

Figure 5.2a Volume scattering functions from *Petzold* [1972] used in Monte Carlo simulations. Station 8 is AUTEC test 161, July 13, 1971; station 11 is HAOCE,August 5, 1971.

$$\tau = cr,$$

which is dimensionless. One optical length, $\tau = 1$, represents the distance that a pencil beam of radiance is reduced by a factor e^{-1} due to absorption and scattering of light out of the beam. Throughout this paper, numerical results are given in terms of the optical path length τ, but in the proofs and some discussions we use the radial distance r for clarity. It should be clear that the two variables are easily interchanged.

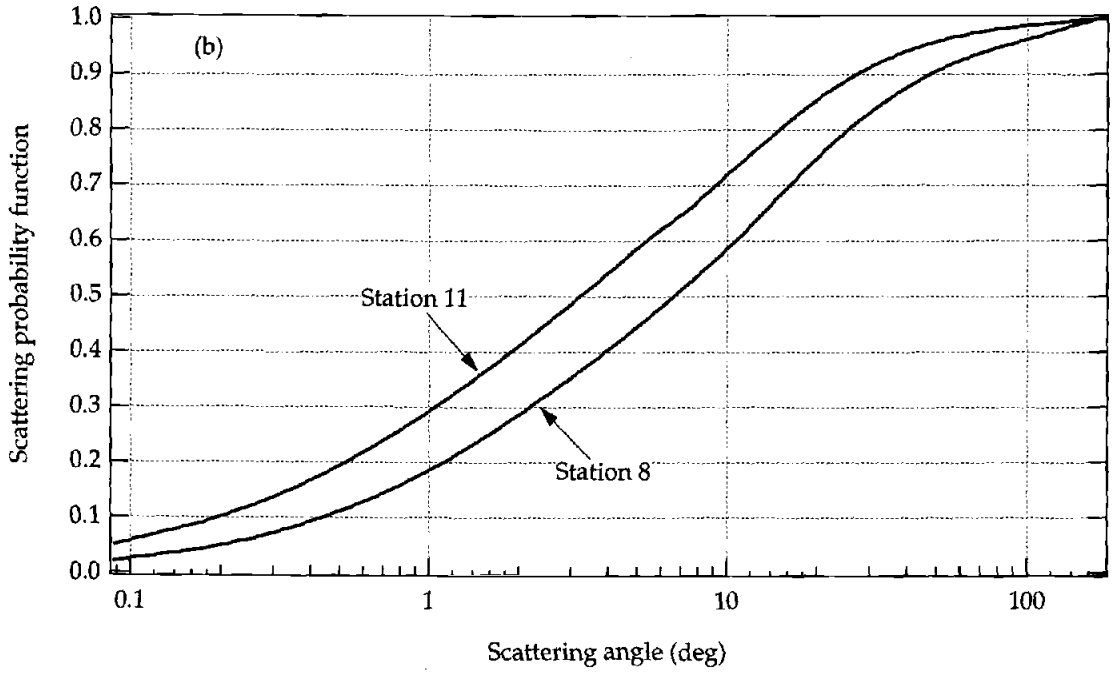

Figure 5.2b Scattering probability functions of the station 8 and station 11 VSF's.

5.4 THEORY

5.4.1 Limiting Values of the Average Cosine Due to an IPS

5.4.1.1 The Limit $r \rightarrow \infty$.

The existence of an asymptotic light field in a homogeneous ocean was first explored mathematically by *Preisendorfer* [1959] and was rigorously proven to exist by *Højerslev and Zaneveld* [1977]. By its definition the asymptotic light field is independent of boundary conditions and is determined solely by the IOP's of the water. Therefore relationships derived for the asymptotic light field apply equally well for an IPS boundary condition as they do for solar, plane-wave illumination. For example, Eq. 5.1 was derived for an IPS boundary condition and becomes Eq. 5.4, derived for the daylight illumination boundary condition,

as $r \to \infty$. Without the existence of an asymptotic light field, the equality of Eq. 5.1 and Eq. 5.4 really only proves that

$$\bar{\mu}_{r\infty}/\bar{\mu}_{\infty} = K_{\infty}/K_{r\infty}$$

This ratio is unity because all diffuse attenuation coefficients become equal in the asymptotic limit. Therefore, in the asymptotic limit, the average cosines for a homogeneous ocean illuminated by the Sun and embedded with an IPS are equal.

That the asymptotic average cosines are equal allows us to use equations for $\bar{\mu}$ that were derived for the submarine daylight field. For example, the so-called Wilson-Honey relationship [*Wilson*, 1979] for K_{∞}/c, namely,

$$K_{\infty}/c = 1 - \tfrac{5}{6}\omega_0$$

can be manipulated using Eq. 5.4 to give

$$\bar{\mu}_{\infty} = \frac{1-\omega_0}{1-\frac{5}{6}\omega_0}. \tag{5.7}$$

Zaneveld [1989] used a second order expansion

$$K_{\infty}/c = 1 - \gamma_1\omega_0 - \gamma_2\omega_0^2 \tag{5.8}$$

to fit data from *Prieur and Morel* [1971] and *Timofeeva* [1971] using the coefficients $\alpha_1 = 0.52$ and $\alpha_2 = 0.44$. The expression for $\bar{\mu}_{\infty}$ using Eq. 5.4 and Eq. 5.8 is

$$\bar{\mu}_{\infty} = \frac{1-\omega_0}{1-\gamma_1\omega_0 - \gamma_2\omega_0^2}. \tag{5.9}$$

It is interesting to note that although K_{∞}/c does not depend strongly on the second-order term, $\bar{\mu}_{\infty}$ does. We performed a least-squares regression using Eq. 5.9 with data from C.D. Mobley (private communication, 1994) that he computed

with an eigenmatrix method [*Mobley*, 1994; *Mobley et al.*, 1993]. Mobley ran the same cases (ref. Table 5.1) with the two *Petzold* [1972] VSF's used in our simulations. Table 5.2 gives the coefficients and Figure 5.3 shows the resulting $\overline{\mu}_\infty$ curves for Wilson-Honey, [*Wilson*, 1979], *Zaneveld* [1989], and *Mobley* [1994].

5.4.1.2 The Limit $r \to 0$.

To derive this limit of $\overline{\mu}$, we must be able to specify the radiance distribution as $r \to 0$. Since the area of a point source is zero, its radiance is undefined. This does not, however, prevent us from considering the radiance distribution due to a point source or the radiance at $\theta = 0$. Conceptually, we may think of the area of the source to be the area that an infinitesimal solid angle subtends at r. As $r \to 0$, the area decreases as r^2 and likewise goes to zero. The radiance distribution must become more and more sharply peaked since the fraction of photons heading in the direction $\theta = 0$ must greatly increase over the fraction that are scattered into other angles as $r \to 0$. This distribution will approach a delta function because the radiance at $r = 0$ becomes infinite since the subtended area goes to zero. For the same reason, the radiance at all other angles

Table 5.2 Coefficients for $\overline{\mu}_\infty$ Regression to the Equation (5.9)

	Empirical	Eigenmatrix Method[a]	
Coefficients	Zaneveld[b]	Station 8	Station 11
γ_1	0.52	0.532	0.666
γ_2	0.44	0.379	0.280

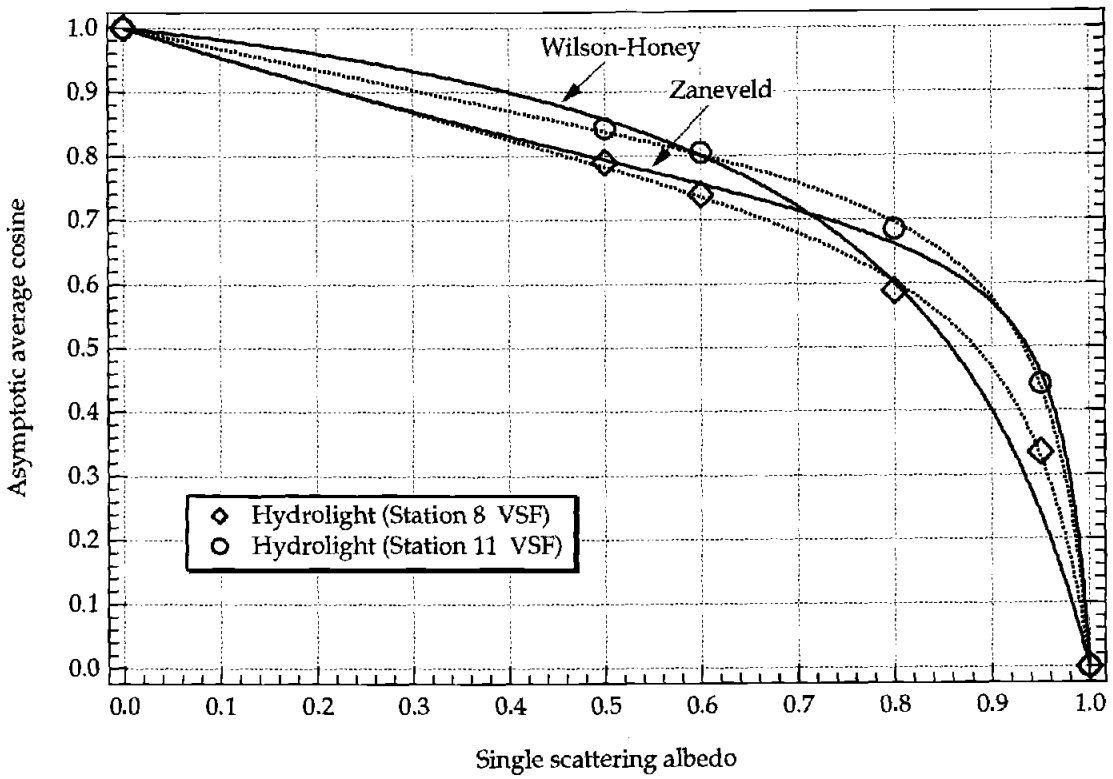

Figure 5.3 Asymptotic average cosine from the Wilson-Honey [Wilson, 1972] and *Zaneveld* [1989] equations compared with $\bar{\mu}$ values computed with the *Mobley* [1994] eigenmatrix method using the station 8 and 11 VSF's. The dotted lines were computed from a regression using (5.9).

goes to zero. Therefore we postulate or assert that the radiance distribution approaches some delta sequence $\delta_n(\theta)$ such that as $r \to 0$, $n \to \infty$, and $\delta_n(\theta) \to \delta(\theta)$, the Dirac delta function. Specifically,

$$\begin{aligned} \lim_{r\to 0} L(r,\theta) &= \lim_{n\to\infty} \frac{I_s}{r^2}\delta_n(\theta) \\ &= \frac{I_s}{r^2}\delta(\theta) \end{aligned} \tag{5.10}$$

where I_s is the (finite) radiant intensity of the IPS.

Starting with the definition of $\bar{\mu}$ as given by Eq. 5.5 and applying Eq. 5.10 we see that

$$\begin{aligned}\lim_{r\to 0}\bar{\mu}(r) &= \lim_{r\to 0}\frac{\int_0^{\pi} L(r,\theta)\cos\theta\sin\theta d\theta}{\int_0^{\pi} L(r,\theta)\sin\theta d\theta} \\ &= \frac{\int_0^{\pi}\left[\lim_{r\to 0} L(r,\theta)\right]\cos\theta\sin\theta d\theta}{\int_0^{\pi}\left[\lim_{r\to 0} L(r,\theta)\right]\sin\theta d\theta} \\ &= \frac{\int_0^{\pi}\delta(\theta)\cos\theta\sin\theta d\theta}{\int_0^{\pi}\delta(\theta)\sin\theta d\theta} \\ &= \frac{\cos(0)\sin(0)}{\sin(0)}\end{aligned} \tag{5.11}$$

Since this limit evaluates to 0/0, we may apply l' Hôspital's rule, which gives

$$\begin{aligned}\lim_{\theta\to 0}\frac{\cos(\theta)\sin(\theta)}{\sin(\theta)} &= \lim_{\theta\to 0}\frac{\cos^2(\theta)-\sin^2(\theta)}{\cos(\theta)} \\ &= 1.\end{aligned}$$

Therefore $\bar{\mu}(0) = 1$ for an isotropic point source.

5.4.1.3 Limit for a Finite Source

In practice, isotropic point sources are approximated by finite diffuse (quasi) isotropic sources [*Brown et al.*, 1991]. If the radius of the source is R, then the question to be addressed is: What is the limiting value of $\bar{\mu}$ as $r \to R$? Since a diffuse isotropic source is a plane Lambertian source at its surface, then from Eqs. 5.5 and 5.6 we have,

$$
\begin{aligned}
\bar{\mu}(R) &= \lim_{r\to R}\bar{\mu}(r) \\
&= \lim_{r\to R}\frac{\int_0^{\pi} L(r,\theta)\cos\theta\sin\theta d\theta}{\int_0^{\pi} L(r,\theta)\sin\theta d\theta} \\
&= \frac{L_s\int_0^{\pi/2}\cos\theta\sin\theta d\theta - \int_{\pi/2}^{\pi} L(R,\theta)\cos\theta\sin\theta d\theta'}{L_s\int_0^{\pi/2}\sin\theta d\theta + \int_{\pi/2}^{\pi} L(R,\theta)\sin\theta d\theta} \\
&= \frac{L_s\frac{1}{2} - E_{-}(R)}{L_s + E_{0-}(R)} \cong \frac{1}{2}
\end{aligned}
\tag{5.12}
$$

where L_S is the radiance of the Lambertian source and we have assumed that $L_s >> E_{-}(R), E_{0-}(R)$, which is clearly true for any realistic volume scattering function. In taking L_S out of the integral we have also assumed that $R << 1/c$ Essentially, we are assuming that the water optical properties and the relative size of the source is such that, at very close distances to the source, it will appear as a plane Lambertian source in air, where the proof holds exactly.

Now consider what happens to $\bar{\mu}$ in the region from the surface of the source to about one optical length ($\tau = 1$). The source subtends a half angle at r given by $\sin\alpha = R/r$. Then $\bar{\mu}$ may be written as

$$
\begin{aligned}
&\bar{\mu}(r) \\
&= \frac{\int_0^{a} L(r,\theta)\cos\theta\sin\theta d\theta + \int_a^{\pi} L(r,\theta)\cos\theta\sin\theta d\theta}{\int_0^{a} L(r,\theta)\sin\theta d\theta + \int_a^{\pi} L(r,\theta)\sin\theta d\theta} \\
&= \frac{\int_0^{a}\cos\theta\sin\theta d\theta + \int_a^{\pi} L(r,\theta)\cos\theta\sin\theta d\theta}{\int_0^{a}\sin\theta d\theta + \int_a^{\pi} L(r,\theta)\sin\theta d\theta} \\
&= \frac{L_s\frac{\sin^2 a}{2} + \int_a^{\pi} L(r,\theta)\cos\theta\sin\theta d\theta}{L_s 2\sin^2(a/2) + \int_a^{\pi} L(r,\theta)\sin\theta d\theta}
\end{aligned}
\tag{5.13}
$$

which is clearly an excellent approximation since the differential path to all points on the source is small and thus L_s is nearly constant with angle. In the region $r < 1/c$ it should also be a very good approximation to neglect the second terms in the numerator and denominator since α will be large and the radiance of the source dominates the radiance distribution. Therefore

$$\bar{\mu} \cong \frac{\sin^2 a}{4\sin^2(a/2)} = \frac{(R/r)^2}{2\left\{1-\sqrt{1-\left[(R/r)^2\right]}\right\}} \tag{5.14}$$

This function is plotted in Figure 5.4 with R/r as the independent variable. It is evident that, although $\bar{\mu} = 0.5$ at $r = R$, it rapidly approaches unity in a short distance from the surface of the source. At distances further than $R/r = 0.1$, $\bar{\mu}$ will decrease in nearly the same fashion as it would for a point source, and the two cases will rapidly become indistinguishable as $r \to \infty$. Experimentally then, where finite diffuse isotropic sources are used, the average cosine of the light field will be nearly identical to the IPS $\bar{\mu}$ at distances greater than, say, one optical length as long as the radius of the source is small compared to $1/c$.

5.4.2 The Mean Light Path and the Absorption Coefficient

If there were no scattering of light in a homogeneous ocean, then the irradiance flowing outward from the source would attenuate geometrically as $1/r^2$ and exponentially according to Beer's law as exp(-*ar*). More precisely,

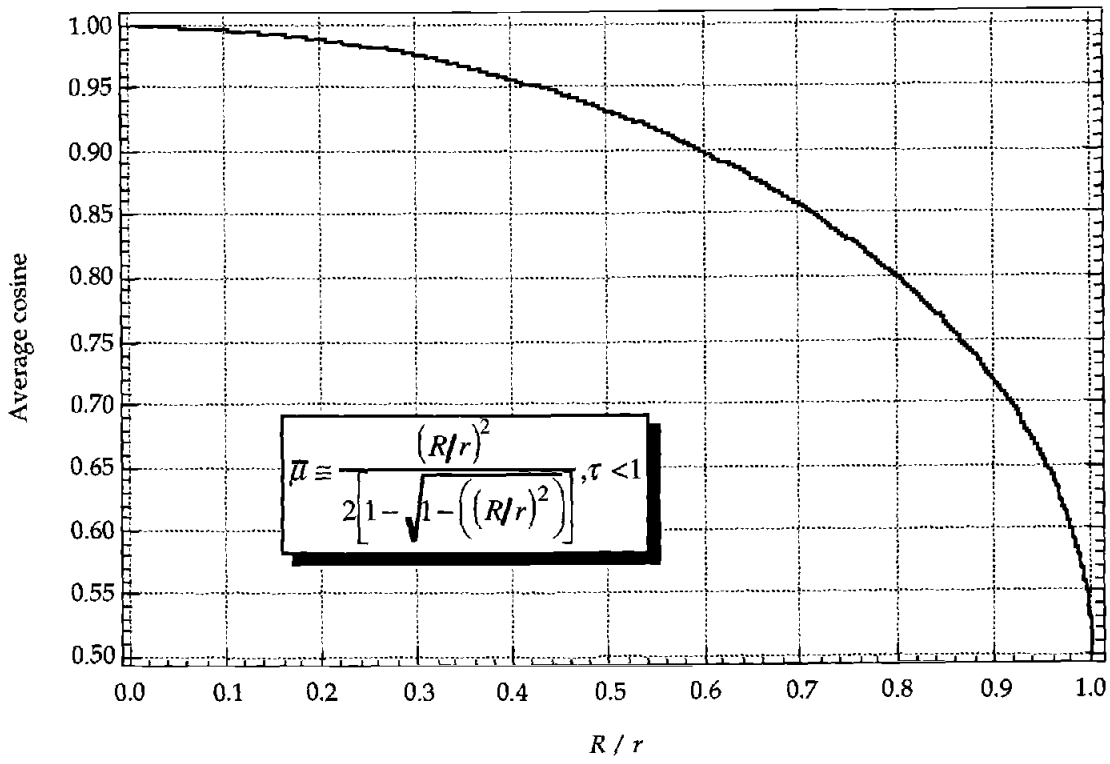

Figure 5.4 The average cosine within one optical length of a finite isotropic source where the radius of the source is one tenth of an optical length.

$$E(r) = E_+(r) = \frac{\Phi_s}{4\pi r^2}\exp(-ar), \tag{5.15}$$

showing explicitly that the net irradiance E equals the outward flowing irradiance E_+ since there is no scattering, i.e., $E_- = 0$. Φ_S is the radiant flux of the source.

Scattering increases the geometric distance photons travel, thereby increasing the probability of photon absorption. An emitted photon that makes it to a radial distance r after one or more scattering events will have actually traveled a total distance $r + \delta r$. To compute the irradiance at r, all photon paths to that point would have to be accounted for and the resulting calculation would be

unwieldy, but *Maffione et al.* [1993] showed that the net irradiance is given exactly by

$$E(r) = \frac{\Phi_s}{4\pi r^2} \exp(-a\bar{r}) \tag{5.16}$$

where

$$\bar{r} = \int_0^r \frac{dr'}{\bar{\mu}(r')} \tag{5.17}$$

is defined as the mean light path. So we see that $\bar{r}$, which depends solely on the average cosine, magically takes into account all of the photon paths when computing net irradiance at a distance r from the IPS.

Comparing Eq. 5.15 with Eq. 5.16 implies that we may write $\bar{r} = r + \overline{\delta r}$, where $\overline{\delta r}$ is defined as the mean increase in the light path due to scattering. The import of $\overline{\delta r}$ is that it applies to any geometry, yet nearly all methods for measuring the absorption coefficient [*Pegau et al.*, this issue] neglect it and use the geometric distance, analogous to r, for the path length. The mathematical formulation of the IPS method for determining a, summarized by Eqs. 5.16 and 5.17, provides an exact expression for the mean increase in the light path, namely,

$$\overline{\delta r}(r) = \int_0^r \left[\frac{1}{\bar{\mu}(r')} - 1 \right] dr' \tag{5.18}$$

which we investigate here with the MC model.

5.5 RESULTS

5.5.1 Comparison of Simulations with Measured PSF's

Measurements of the PSF at Lake Pend Oreille, Idaho, with both plane Lambertian and isotropic sources, provided us an opportunity to compare the MC model to measurements in natural water. The measurements were conducted as part of the ONR sponsored optical closure experiment in April-May, 1992. The experimental arrangement is described in *Maffione et al.* [1991, 1993]. Briefly, a light source [*Brown et al.*, 1991] is lowered into the water and images of the source are recorded by an integrating CCD camera [*Voss and Chapin*, 1990]. The electronic camera is lowered to some depth and the distance between the source and camera are varied by changing the depth of the source. During the Lake Pend Oreille experiment we used a 50-mm focal-length lens and a 532-nm interference filter (10-nm bandwidth) with the camera. This arrangement provided measurements of the PSF out to nearly 20°, although light levels were usually noise limited by 15°.

The light source arrangement allowed us to interchange a flat diffuser with a diffusing globe. The flat diffuser created a cosine (i.e., plane Lambertian) source with a diameter of 3.8 cm. The diffusing globe created an isotropic source with a diameter of 12.7 cm. Most measurements at Lake Pend Oreille were made with the isotropic source. Occasionally, we made measurements with the cosine source to see how these PSF's compared with the isotropic-source PSF's. The advantage of using the flat diffuser is that all of the light emitted by the light source is initially directed into the forward hemisphere, toward the camera,

allowing us to measure the radiance distribution at larger angles and at farther distances from the source than we could when all of the light is directed isotropically.

On May 6 a series of PSF's were measured using the isotropic source with the camera held at a 60-m depth. When the run was complete, the system was immediately hauled to the surface and the diffusing globe was replaced with the flat diffuser, creating a cosine source. Then another series of PSF measurements were made with the camera at the same depth. The absorption and beam attenuation coefficients were estimated with the IPS method [*Maffione et al.*, 1991, 1993]. At 60 m they were $a = 0.12\ m^{-1}$ and $c = 0.40\ m^{-1}$ at 532 nm. Thus the single scattering albedo was $\omega_0 = 0.70$. These optical properties most closely match our "coast" PSF simulations (ref. Table 5.1). Figures 5.5a-5.5d show comparison plots of the measured PSF's with the simulated coast PSF's at one, three, six, and ten optical lengths for the simulated data. These optical path lengths roughly correspond to the optical path lengths of the measured PSF's. The isotropic source PSF is missing in Figure 5.5d because there was not enough measurable light at this distance. The PSF units are arbitrary and were scaled to adjust the vertical height of the curves for better comparison. We are not interested in the absolute magnitudes, only the shapes of the PSF's, which are not affected by our scaling. The scales of the four plots are identical so that the slopes and their changes with distance can more easily be compared.

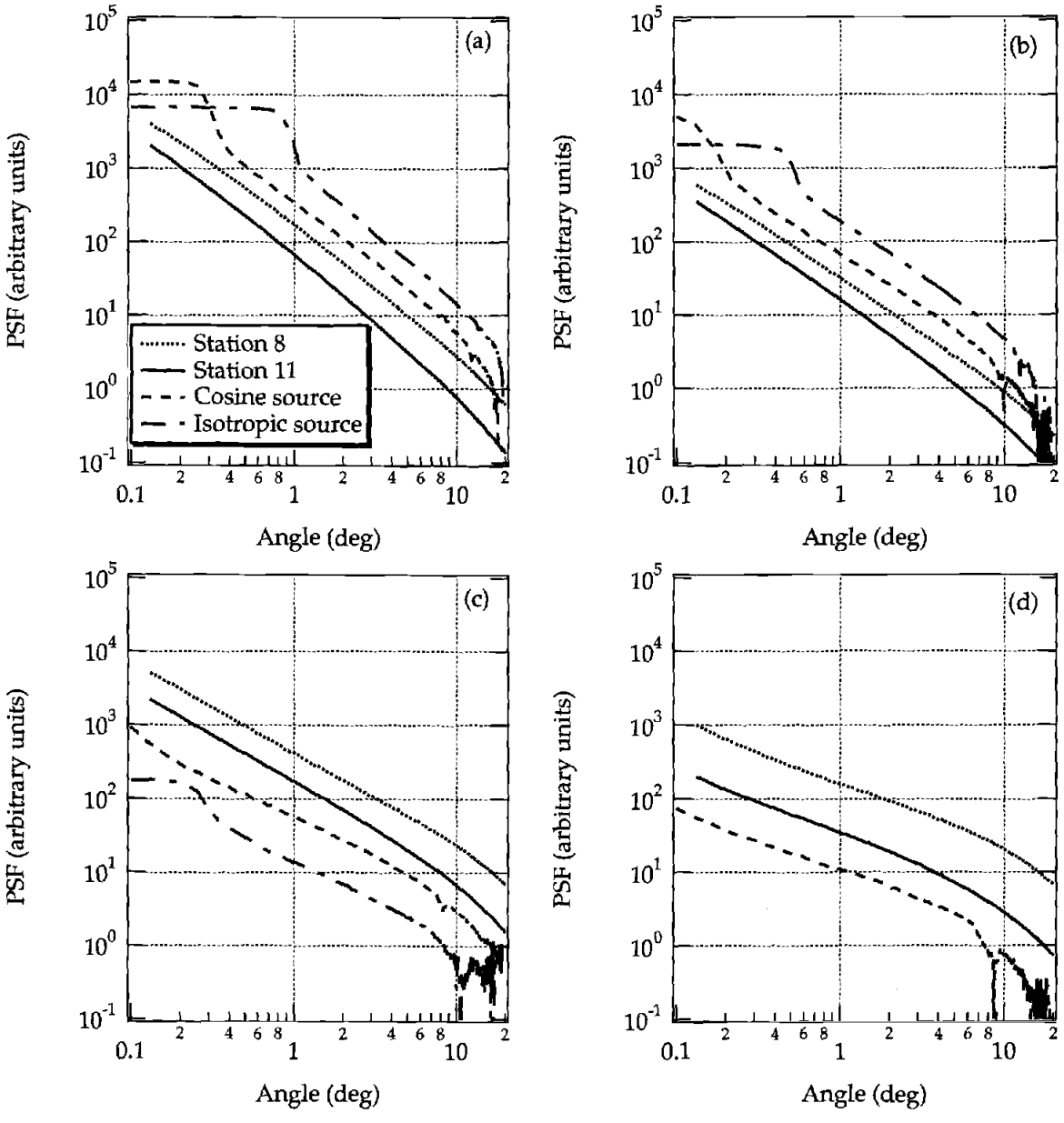

Figure 5.5 Comparisons of the Monte Carlo radiance distributions, or PSF's, and the measured PSF's at Lake Pend Oreille during the optical closure experiment. (a) Approximately one optical length from the source; (b) approximately three optical lengths from the source; (c) approximately six optical lengths from the source; (d) approximately ten optical lengths from the source.

As the distance from the source is increased, the slope of the PSF will decrease due to multiple scattering of photons into larger angles that were initially headed at smaller, forward angles. Figures 5.5a-5.5d clearly show the decreasing slopes at greater ranges for both the modeled and measured PSF's. The horizontal portion of the measured PSF's are the sources themselves. The extremely sharp drop-off is an edge effect caused by the sharp transition in the radiance distribution from directly transmitted plus scattering light to purely scattered light. For our comparison we are interested in the portion of the PSF away from source and edge effects.

At a fixed distance from the source, the slope of the PSF will be primarily dependent on the VSF and the ω_0 of the water. The station 11 VSF yields higher PSF slopes than the station 8 VSF, as expected, because the former VSF has a steeper slope than the latter (ref. Figure 5.2a). A steeper slope means a higher scattering probability function (ref. Figure 5.2b) which implies that a greater fraction of scattered photons are contained within the smaller scattering angles causing the PSF to decrease faster with increasing radiance angle. The slopes of the PSF's were computed at a radiance angle of about 5° and are plotted in Figure 5.6 as a function of optical path length. The slope of the PSF was computed by a linear regression on a log-log scale. In general, the measured PSF slopes fall between the model PSF slopes for the two VSF's used in the simulations. If the slopes at 3τ for the measured PSF's are ignored, the trends for the change in slopes with optical path length are fairly similar. The anomalous slopes at 3τ are probably a measurement artifact since linear trends were found

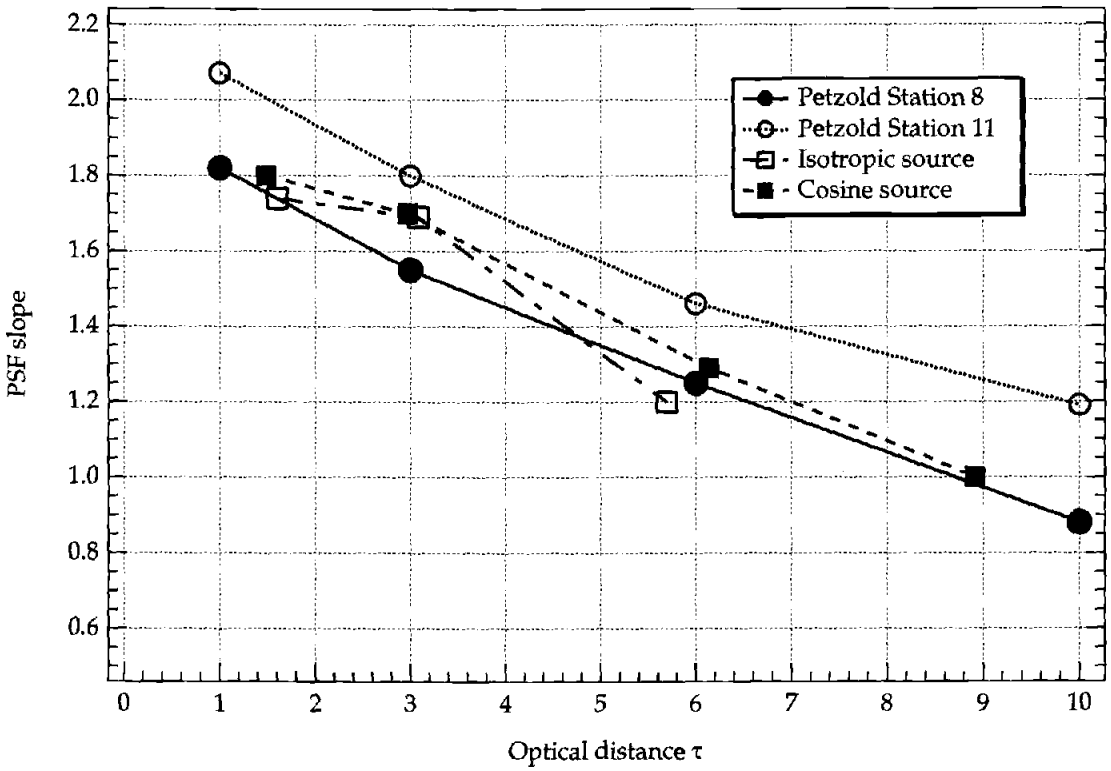

Figure 5.6 Comparison of PSF slopes from measurements at Lake Pend Oreille with the Monte Carlo "coast" runs.

when these plots were made using slopes computed at angles other than 5°. It is not the intent here to present an analysis of PSF slopes but rather to demonstrate that the model gives physically reasonable PSF's.

5.5.2 Model of the Average Cosine

The average cosine was computed with Eq. 5.6 at the seven optical path lengths for each water type (ref. Table 5.1) and for the two *Petzold* [1972] VSF's (station 8 and 11). Figure 5.7 shows the results for station 11. We found that $\bar{\mu}$ fit the exponential equation

$$\bar{\mu}(r) = k_0 + k_1 \exp(-k_2 r) \tag{5.19}$$

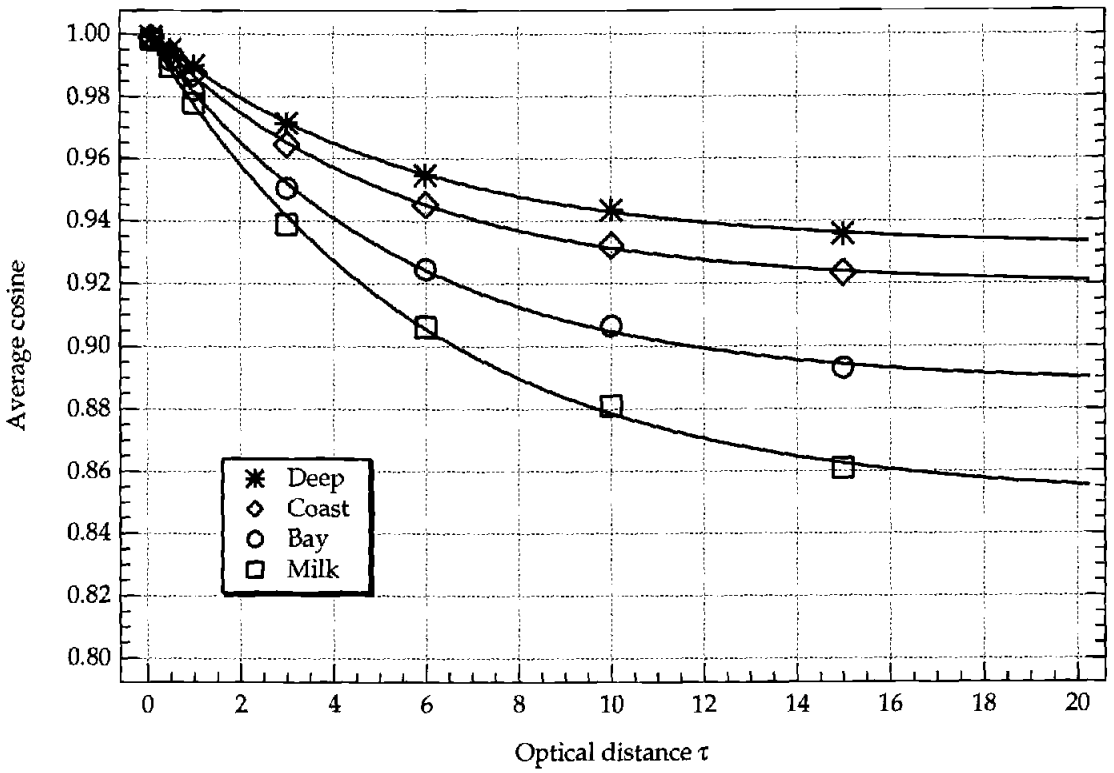

Figure 5.7 The average cosine as a function of optical path length from an IPS computed from the station 11 VSF simulations. Solid curves were determined from a regression to (5.19).

quite well for all of the simulations. The regression coefficients, k_0, k_1, k_2, for all of the cases we studied are given in Table 5.3. Note that $k_0 + k_1$ sums almost exactly to one in all cases, as it should by our proof that $\bar{\mu} \to 1 \text{as} r \to 0$. We did not constrain the regression to do so.

A fortunate coincidence of Eq. 5.19 is that it can be integrated to give analytic solutions to Eqs. 5.17 and 5.18. The solutions are

$$\bar{\tau} = k_0 + \frac{1}{k_0 k_2} ln\left[\bar{\mu}(\tau)\right] \tag{5.20}$$

and

TABLE 5.3 Coefficients for $\bar{\mu}$ Regression to the Equation (5.19)

	Station 8 VSF			Station 11 VSF		
Type	k_0	k_1	k_2	k_0	k_1	k_2
Deep	0.9024	0.0985	0.2309	0.9315	0.0693	0.1811
Coast	0.8846	0.1169	0.2428	0.9193	0.0817	0.1918
Bay	0.8466	0.1552	0.2546	0.8875	0.1136	0.1880
Milk	0.8132	0.1891	0.2578	0.8502	0.1506	0.1668

$$\overline{\delta\tau} = \tau\left(\frac{1}{k_0} - 1\right) + 1n\left[\bar{\mu}(\tau)\right] \tag{5.21}$$

where $\bar{\mu}(\tau)$ is given by Eq. 5.19. The mean increase in the light path, Eq. 5.21, is plotted in Figure 5.8 for the station 11 VSF. We see that $\overline{\delta\tau}$ reaches one tenth of an optical length at about $\tau = 3$ in the most highly scattering case (milk). Not until $\tau = 11$ does the mean light-path increase reach one optical length. For clear ocean water (deep), $\overline{\delta\tau} = 1$at $\tau = 19$! For all types of natural water, the mean increase in the light path is small compared to the distance from the source. It is important to point out that this is not necessarily the case for light-field geometries other than the spherically symmetric IPS geometry. For solar illumination, $\overline{\delta\tau}(z)$will in many cases be a significant fraction of z, where z is the vertical distance. In the next section we investigate the errors in ignoring $\overline{\delta\tau}$ when estimating the absorption coefficient with the IPS method.

Equation 5.19 shows that as $\tau \to \infty$, $\bar{\mu} \to k_0$ so that we might expect $\bar{\mu}_\infty = k_0$. It also appears from Figure 5.7 that $\bar{\mu}$ accurately approaches $\bar{\mu}_\infty$ according to

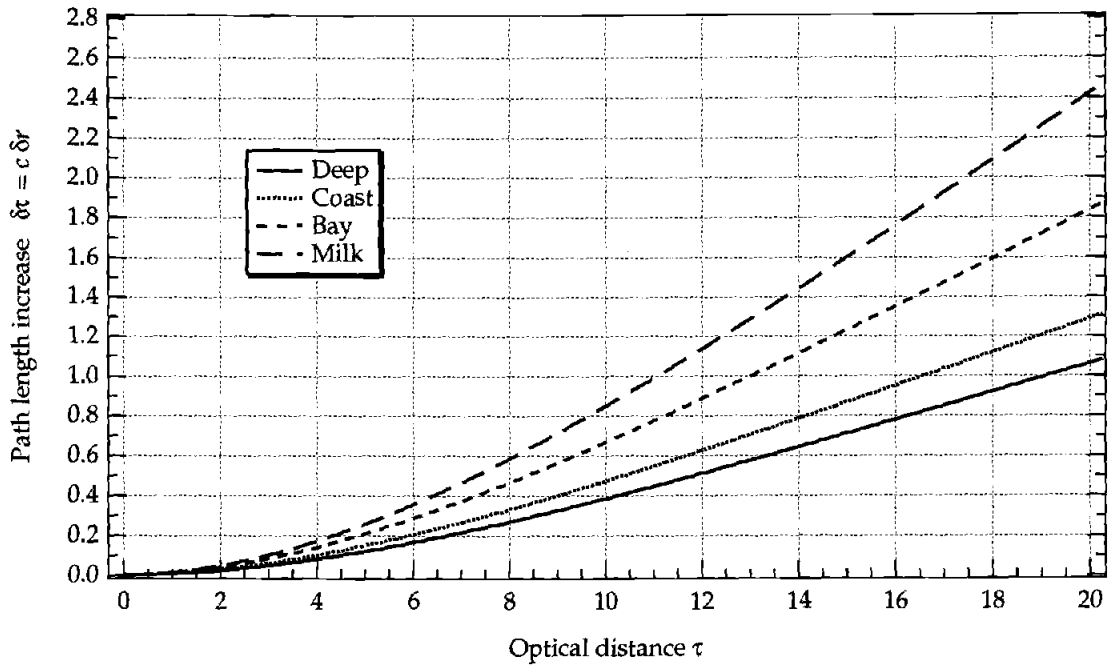

Figure 5.8 The mean path-length increase as a function of optical path length from an IPS computed from the Station 11 VSF simulations.

Eq. 5.19, but when the asymptotic values, k_0, are plotted versus ω_0 and compared to the asymptotic values computed by C. D. Mobley (private communication, 1994), similar to what was shown in Figure 5.3, we get the results shown in Figure 5.9. As pointed out earlier, all asymptotic values of the average cosine must be equal, independent of the boundary conditions for the same IOP's. Because the Mobley values compare exceptionally well with empirical data (ref. Figure 5.3), we are led to the conclusion that Eq. 5.19 does not accurately predict the asymptotic values of the average cosine, $\overline{\mu}_\infty$. Nonetheless, Eq. 5.19 does accurately model the behavior of $\overline{\mu}$ within at least 15 optical lengths from the source, which is clearly evident in Figure 5.7.

We estimated the model parameters in a regression to only the last three $\overline{\mu}$ values at $\tau = 6, 10, 15$ to see if the k_0 parameter would then better agree with C. D.

Mobley (personal communication, 1994). Although k_0 did decrease, it was by only a few percent and was still significantly too high. Our conclusion is that $\tau =$ 15 is still nowhere near the asymptotic light field for an IPS. Further evidence of this conclusion can be seen in Figure 5.10, where the normalized radiance distributions at τ = 15 are plotted together with the asymptotic radiance distributions computed by Mobley with his eigenmatrix method [*Mobley*, 1994]. It can be seen that even for the highly scattering case, ω_0 = 0.95, the inflection in the radiance distribution near zero is still not evident for the IPS boundary condition. Because the exponential fit of the $\bar{\mu}$ values at $\tau = 6$, 10, 15 to Eq. 5.19 was quite good and yet still predicted values of $\bar{\mu}_\infty$ that were significantly higher than expected, it is possible and even likely that $\bar{\mu}(\tau)$ itself undergoes an inflection as $\tau \to \infty$.

5.5.3 Determining the Absorption Coefficient

The absorption coefficient can be estimated experimentally by making measurements of the net irradiance $E(r)$ due to an isotropic source as a function of distance [*Maffione et al.*, 1991, 1993]. Taking the natural logarithm of Eq. 5.16 and rearranging gives

$$\ln\left[r^2 E(r)\right] = \ln\left(\frac{\Phi_s}{4\pi}\right) - a\bar{r} \tag{5.22a}$$

$$\cong \ln\left(\frac{\Phi_s}{4\pi}\right) - ar. \tag{5.22b}$$

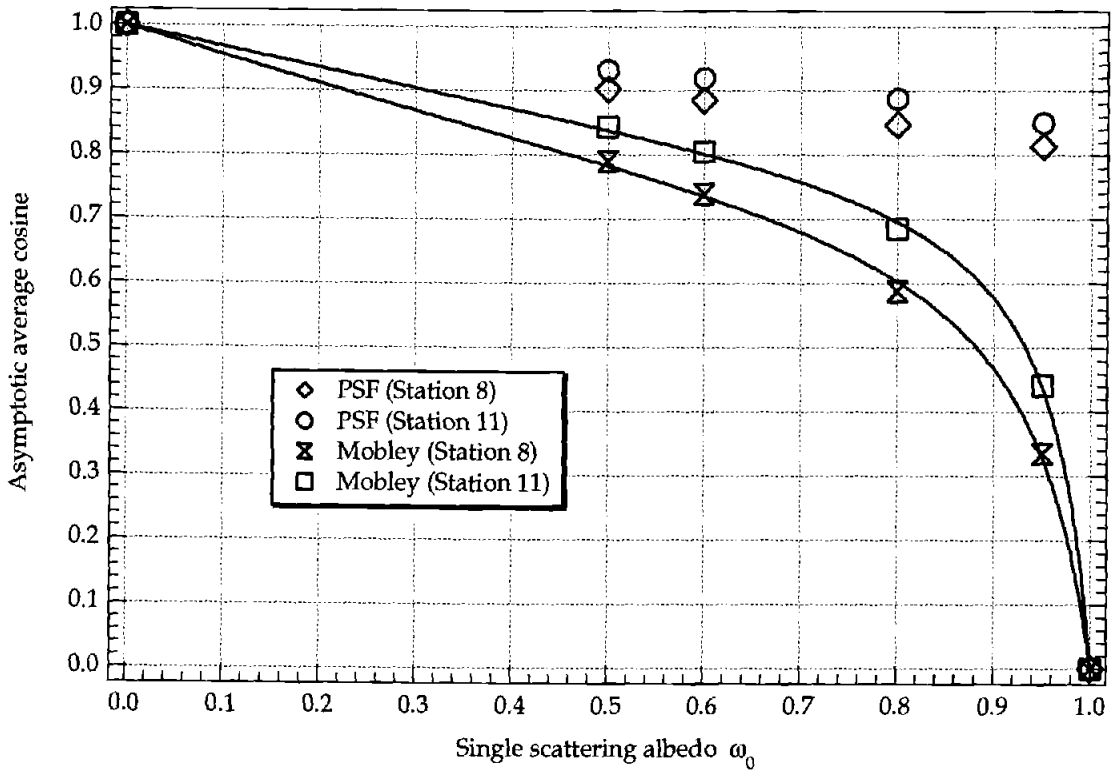

Figure 5.9 Comparison of average cosines from Monte Carlo simulations at 15 optical lengths with asymptotic average cosines from eigenmatrix computations.

The slope of a linear regression of the measurements of $E(r)$ to Eq. 5.22a yields the absorption coefficient, assuming $\bar{r}(r)$ is known. In practice, $\bar{r}(r)$ is not known and Eq. 5.22b is used to estimate a. As we showed above, to a very good approximation, especially near the source, $\bar{r} \cong r$.

From our simulations we can now estimate $\bar{r}(r)$ using Eq. 5.20 and investigate the errors in estimating a using Eq. 5.22b. Also, because the MC model uses a known input value of a, we can check the accuracy of the MC model and the $\bar{\mu}$ model (Eq. 5.19) by estimating a with Eq. 5.22a since this equation is exact. The results are summarized in Tables 5.4a and 5.4b, where the last column gives the percent error in estimating a with Eq. 5.22a. These errors

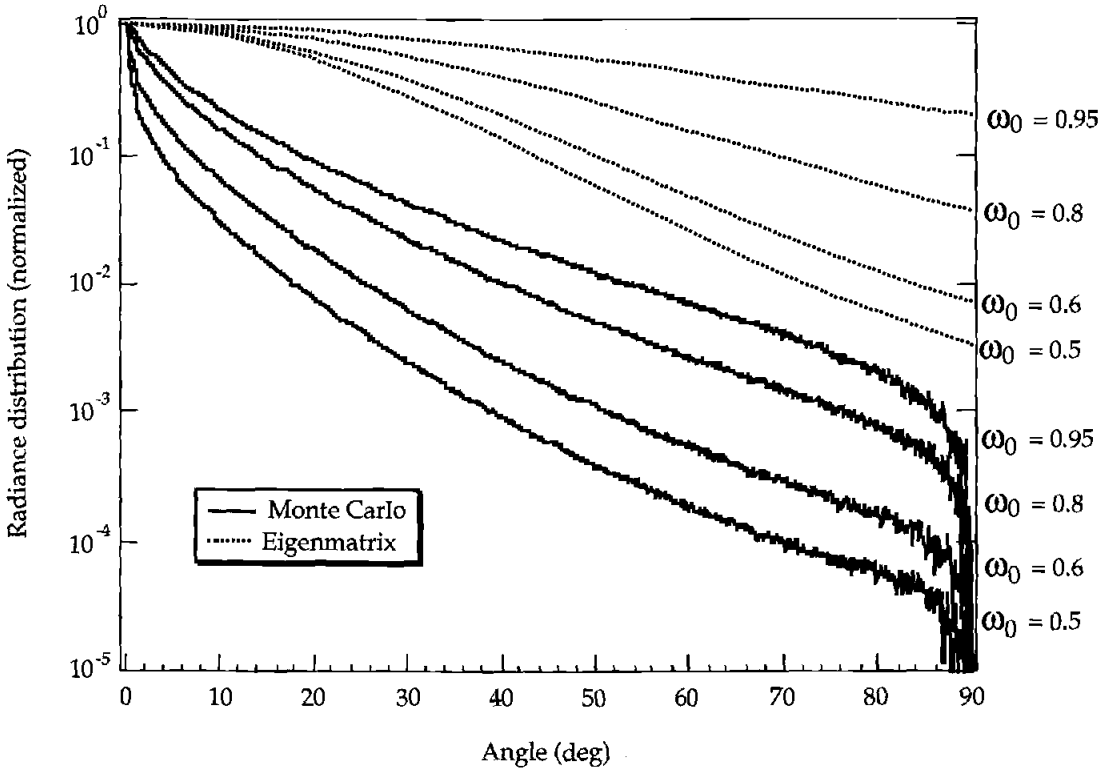

Figure 5.10 Comparison of normalized radiance distributions from Monte Carlo simulations at 15 optical lengths with asymptotic radiance distributions from eigenmatrix computations.

are due to errors in both the MC model and the $\bar{\mu}$ model together since the $\bar{\mu}$ model was needed to compute $\bar{r}(r)$. The fourth column gives the percent error in estimating a with Eq. 5.22b, which neglects the mean light-path increase $\overline{\delta r}$. These errors, however, include the errors due to the MC and $\bar{\mu}$ models as well as the errors in using the approximation (Eq. 5.22b). Therefore the difference between the errors in columns 4 and 6 is a better indicator of the errors due to using Eq. 5.22b for estimating a. Ignoring the milk runs, which are not realistic for natural waters, the largest error is then about 12% (bay, station 8 VSF) and the smallest is about 5% (deep, station 11 VSF).

One observation of these results is that the error in estimating a is a strong function of both ω_0 and the VSF. That the errors should be strongly related to ω_0 is expected, but the strong dependence on the VSF is somewhat surprising. The errors roughly double between the station 11 VSF and the station 8 VSF, yet the scattering probability functions do not differ that greatly between the two VSF's (ref. Figure 5.2b). Evidently, however, this difference does have a significant affect on the mean light path. Figure 5.11 shows the differences in the increase in the mean light paths, $\overline{\delta r}$ (station 8) -$\overline{\delta r}$ (station 11). Comparing this to Figure 5.8 shows that the change in $\overline{\delta r}$ is over half the magnitude of $\overline{\delta r}$ for the station 11 VSF.

5.6 CONCLUSIONS

The radiance distribution due to an isotropic point source embedded in the ocean can, in theory, be inverted to yield all of the inherent optical properties of the medium. Approximations have been developed by *Sorenson and Honey* [1968] and *Wells* [1969]. Sorenson and Honey's approximations can be used to estimate the absorption, attenuation, and backward scattering coefficients. Wells' paraxial approximation can be analytically inverted to yield the volume scattering function in the small-angle limit. The accuracy of these approximations depends on the shape of the volume scattering function as well as the distance to the light source. The only known exact solution for an IOP derived from an IPS light field was presented by *Maffione et al.* [1993]. They derived the absorption coefficient by transforming *Gershun's* [1936] Equation to spherical coordinates. Their

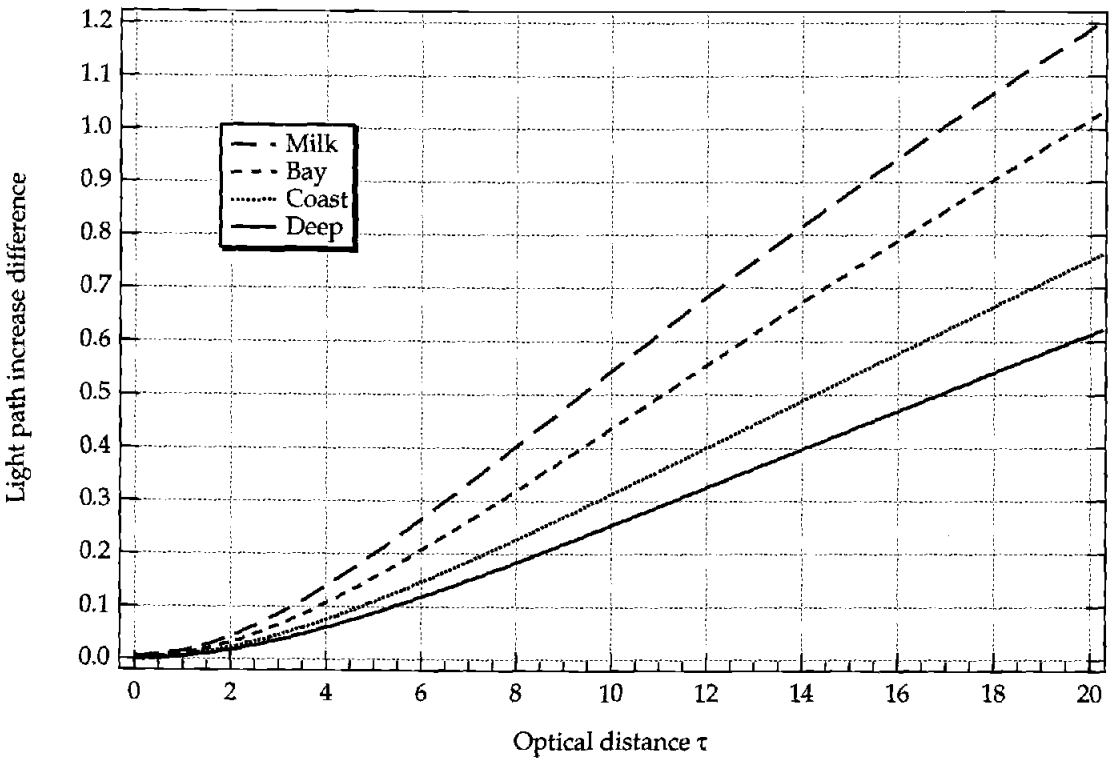

Figure 5.11 Differences in the mean light-path increase from the station 8 and 11 VSF's.

derivation showed that the average cosine $\bar{\mu}$ was fundamental to describing how scattering increases the optical path length and thus the probability of photon absorption.

A Monte Carlo model that computes the IPS radiance distribution was compared with point spread functions measured in Lake Pend Oreille, Idaho [*Maffione*, 1993]. MC simulations using volume scattering functions from *Petzold* [1972] compared quite well with the measured PSF's (Figures 5.5a-5.5d). The slopes of the measured PSF's fell within the slopes of the simulated PSF's (Figure 5.6).

For homogeneous water the asymptotic radiance distribution is only a function of the IOP's and independent of the boundary conditions [*Preisendorfer*, 1959; *Højerslev and Zaneveld*, 1977]. Given the same IOP's, the asymptotic light field due to an embedded IPS is thus identical to that for an ocean illuminated by solar, plane-wave radiation. Comparing the MC results at 15 optical lengths from the source to eigenmatrix calculations of the asymptotic daylight field [*Mobley*, 1994] showed that 15 optical lengths is nowhere near the asymptotic limit for an IPS light field, even for the murkiest of waters ($\omega_0 = 0.95$). Using the eigenmatrix results and a model for the asymptotic $\bar{\mu}$ presented by *Zaneveld* [1989], new coefficients for the model were computed that were shown to depend on the VSF (Table 5.2).

By describing the IPS radiance distribution as a delta sequence near the source, we proved that $\bar{\mu} \rightarrow 1$ as $r \rightarrow 0$. For a finite diffuse isotroptic source, we showed that $\bar{\mu} \rightarrow 1/2$ at the surface of the source. If $R << 1/c$, where R is the radius of the source and c the attenuation coefficient, then $\bar{\mu}$ rapidly approaches unity very near the surface, and at distances beyond one optical length, $1/c$, it behaves essentially as it would for an IPS. On the basis of our MC simulations we developed a simple analytic model, Eq. 5.19, for $\bar{\mu}$ valid out to at least 15 optical lengths from the source. This model can be used to compute the mean light path, (5.17), and the increase in the mean light path, Eq. 5.18, due to scattering. The analytic solutions to Eqs. 5.17 and 5.18 based on the model are given by Eqs. 5.20 and 5.21, respectively.

Sorenson and Honey [1968] argued that the absorption coefficient a could be estimated using Eq. 5.22b which does not depend on the increase in the mean light path due to scattering and hence assumes $\overline{\mu} = 1$. The exact result, Eq. 5.22a, was derived by *Maffione et al.* [1993] and does depend on the true value of $\overline{\mu}$. Our model for $\overline{\mu}$, Eq. 5.19, showed that the errors in neglecting the increase in the mean light path due to scattering are, for nearly all natural waters, between 5% and 12% of the true value of a.

Chapter 6

THEORY AND MEASUREMENTS OF THE COMPLETE BEAM SPREAD FUNCTION OF SEA ICE

Robert A. Maffione and Curtis D. Mobley

Submitted to *Limnology and Oceanography*

6.1 ABSTRACT

The beam spread function (BSF) of sea ice is of interest for several reasons. The BSF characterizes beam propagation through sea ice. Its equivalent, the point spread function (PSF), is essentially the optical impulse response of the medium, which has many useful connections to radiative transfer theory. In-ice measurements of the BSF over the full angular range 0 to 180 degrees, using a novel method, were made of first- and multi-year ice off the shore of Barrow, Alaska. All of the measured sea ice BSF's were drastically different than the BSF of ocean water, and they strongly indicated that sea ice is a highly scattering medium, with a single scattering albedo generally greater than 0.97. At pathlengths greater than 30 cm, the BSF was found to be nearly identical to the computed asymptotic radiance distribution. The rapid approach to the asymptotic state and the high single scattering albedo of sea ice suggests that photon diffusion theory should accurately describe radiative transfer in sea ice. Equating the results of diffusion theory with asymptotic radiative transfer theory yields a simple expression that relates the asymptotic attenuation coefficient K_∞ to the inherent optical property coefficients and the asymmetry parameter g of the scattering phase function. It is shown that the necessary optical parameters for computing g can be obtained from the measured BSF. Thus all the information necessary for modeling optical propagation in sea ice can be obtained from the BSF measurements using the method described here.

6.2 INTRODUCTION

Sea ice is generally a highly scattering optical medium. It's physical structure is highly complex as well, consisting of a usually unknown distribution of air bubbles, irregularly shaped brine pockets, fractures, and embedded particles, which all strongly scatter light [*Perovich and Gow*, 1991]. Measuring the optical properties of sea ice is equally challenging due to its solid nature and the usually harsh working conditions. Thus sea ice remains one of the least understood natural optical media.

To characterize the optical properties of sea ice, researchers usually have taken an approach similar to that employed for characterizing the optical properties of ocean water, but with greater limitations. For example, the spectral solar irradiance attenuation through sea ice has been measured and the results characterized by bulk irradiance attenuation coefficients for the entire slab of ice [*Grenfell and Maykut*, 1977; *Maykut and Grenfell*, 1975; *Perovich, Maykut, and Grenfell*, 1986]. In fact, nearly all optical measurements of sea ice in the field have involved ambient light measurements, from which apparent optical properties (AOP's) of sea ice can be directly computed. These measurements and the resultant AOP's are useful for characterizing optical propagation through sea ice, but they suffer from the same difficulties of interpretation as do AOP's of ocean water.

Obtaining data on the inherent optical properties (IOP's) of sea ice is highly desirable because IOP's yield information about the fundamental optical nature of the medium. Moreover, IOP's are necessary input for

radiative transfer models of light propagation in sea ice [*Grenfell*, 1991; *Perovich and Grenfell*, 1982]. But sea ice IOP's are exceedingly difficult to measure, even in the laboratory [*Light*, 1995; *Perovich and Grenfell*, 1981]. Nonetheless, a few researchers have made heroic attempts at measuring sea ice IOP's, including the absorption coefficient [*Grenfell and Perovich*, 1981; *Perovich and Govoni*, 1991; *Roesler and Iturriaga*, 1994], the scattering phase function [*Grenfell and Hedrick*, 1983; *Miller et al.*, 1994], and the index of refraction [*Maykut and Light*, 1996]. Thus far, however, reported results remain preliminary, especially regarding the IOP's of natural sea ice.

The beam spread function (BSF) and its mathematical equivalent, the point spread function (PSF), are useful radiometric functions for characterizing an optical medium [*Mertens and Replogle*, 1977]. The BSF is defined as the irradiance distribution due to a collimated beam as a function of distance R and polar angle θ from the source, normalized by the source power, or radiant flux. The PSF is defined as the radiance distribution due to a plane Lambertian source, as a function of R and θ, normalized by the source power divided by π, i.e., the PSF is normalized by the maximum source intensity. (See Mertens and Replogle [1977] for a thorough description of these two functions.) Although it was known for some time that the PSF and BSF are equal [*Honey*, 1979], a rigorous proof was only recently given by *Gordon* [1994].

The PSF is fundamental to imaging [*Wells*, 1969] and the BSF has direct applications to laser propagation and lidar [*Honey*, 1979]. Small-angle

scattering theory relates the PSF to the volume scattering function (VSF) in the paraxial, or small-angle, approximation in a way that can be analytically inverted to obtain the VSF from the measured PSF [*Wells*, 1969]. Due to the interest in underwater imaging and ocean lidar, considerable attention has been given to characterizing the PSF of ocean waters [*Voss*, 1990; *Maffione et al.*, 1991], although there has been little progress at inverting the measured PSF to obtain the VSF using small-angle scattering theory [*Voss*, 1991].

Since the PSF is essentially the radiance distribution due to a Lambertian source, it can be integrated to yield the scalar and planar irradiances. *Maffione et al.* [1993] have shown that the bulk absorption coefficient of the medium can be accurately determined from these two irradiance measurements as a function of distance from the source. No absolute calibration is needed, and furthermore the method is exact, so that its accuracy is unaffected by even a highly scattering medium. Thus, the method described below for measuring the complete BSF of sea ice, which is the equivalent PSF, can be integrated to yield both the scalar and net irradiances due to a Lambertian source. From these two irradiance quantities, the absorption coefficient, diffuse attenuation coefficient, and the average cosine of the light field can be determined.

The only reported attempt at measuring the PSF of sea ice was performed by *Gilbert and Buntzen* [1986] using a method developed by *Honey* [1979] and instrumentation developed by *Moore* [1985]. Gilbert and Buntzen attempted to measure the bulk PSF of Arctic sea ice by lowering a Lambertian light source into the water below the ice and recording the radiance distribution

emerging above the ice with a camera. Problems with their particular experimental method in the harsh arctic environment limited the usefulness of these measurements. Nonetheless, a subsequent analysis of the Gilbert and Buntzen data by *Voss et al.* [1992] showed that the PSF of sea ice is far broader than the PSF of ocean water, indicating a high degree of scattering by sea ice.

Measurements of the planar irradiance distribution due to a collimated source — which is a paraxial approximation to the BSF — were made of a slab of laboratory grown saline ice by *Schoonmaker et al.* [1989]. Their results also showed that sea ice is a highly scattering medium. Schoonmaker et al. computed the BSF with forward and inverse Hankel transforms of their planar irradiance measurements. Using the same optical geometry as Schoonmaker et al., *Longacre and Landry* [1994] measured the planar irradiance distribution due to a beam propagating vertically through a bulk slab of Arctic sea ice. As in Schoonmaker et al.'s setup, Longacre and Landry's measurements were not strictly the BSF, but their results once again confirmed that sea ice is a highly scattering medium. *Tanis* [1994] also used a similar setup to make beam spreading measurements of sea ice samples taken from cores. Tanis's goal was to use his measurements in Wells's small-angle scattering inversion algorithm [*Wells*, 1971] to obtain the small-angle VSF. However, recent investigations by *Joelson* [1996], using a Monte Carlo model, indicate that small-angle scattering theory breaks down for highly scattering media because these theories do not take into account the scattering of photons back into the forward light path. These theories take into account

only multiple scattering that occurs within the paraxial angles (nominally < 10°). Therefore it does not appear that the small-angle VSF can be determined for sea ice, which is a highly scattering medium, with the Wells inversion algorithm.

A new method for measuring the BSF of sea ice is described below. It is shown that this method allows the BSF to be measured over the full 180° range of polar angles in a manner that properly relates it to the strict definition of the BSF. This method determines the BSF over horizontal paths of selected distances, as opposed to previous field techniques which measure only vertical paths through the entire ice sheet. Moreover, the horizontal-path BSF can be measured as a function of depth within the ice. This method was tested near Barrow, Alaska, in the springs of 1993, 1994, and 1995, and several data sets of the complete BSF of sea ice were obtained. These experiments were conducted as part of the Office of Naval Research (ONR) sponsored program, Electromagnetic Properties of Sea Ice (EMPOSI). The results of the 1995 experiment are used in the analysis presented here.

6.3 INSTRUMENTS AND METHODS

In collaboration with S. Pegau and R. Zaneveld of Oregon State University, instrumentation was developed for measuring beam attenuation in sea ice. The optical instrumentation was built by WET Labs, Inc., and a unique ice coring rig was built by the Polar Ice Coring Office (PICO), then at the University of Alaska, Fairbanks. After initial field trials, the optical instrumentation was modified for measuring the BSF in the manner

illustrated in Figure 6.1. Two holes are cored in the ice with a separation R, where R is defined as the horizontal distance through the ice separating the holes. A collimated light source, in this case a laser diode within a cylindrical housing, is lowered into one hole (left one in Figure 6.1). An irradiance detector, also in a cylindrical housing, is lowered into the other hole and aligned with the axis of the source beam. As discussed above, the BSF is the irradiance distribution around a constant arc from a collimated source, as illustrated in the inset in Figure 6.1. For an isotropic medium, it is entirely equivalent if the irradiance detector is kept fixed and the source is rotated. For example, in the inset of Figure 6.1, if the beam is pointed at the position of $E(\theta)$, then the irradiance $E(0)$ will be identical to the irradiance at $E(\theta)$ when the source is pointing in its original direction at $E(0)$. Therefore as the source beam in the cylindrical housing on the left in Figure 6.1 is rotated, the irradiance distribution recorded by the detector is BSF(θ).

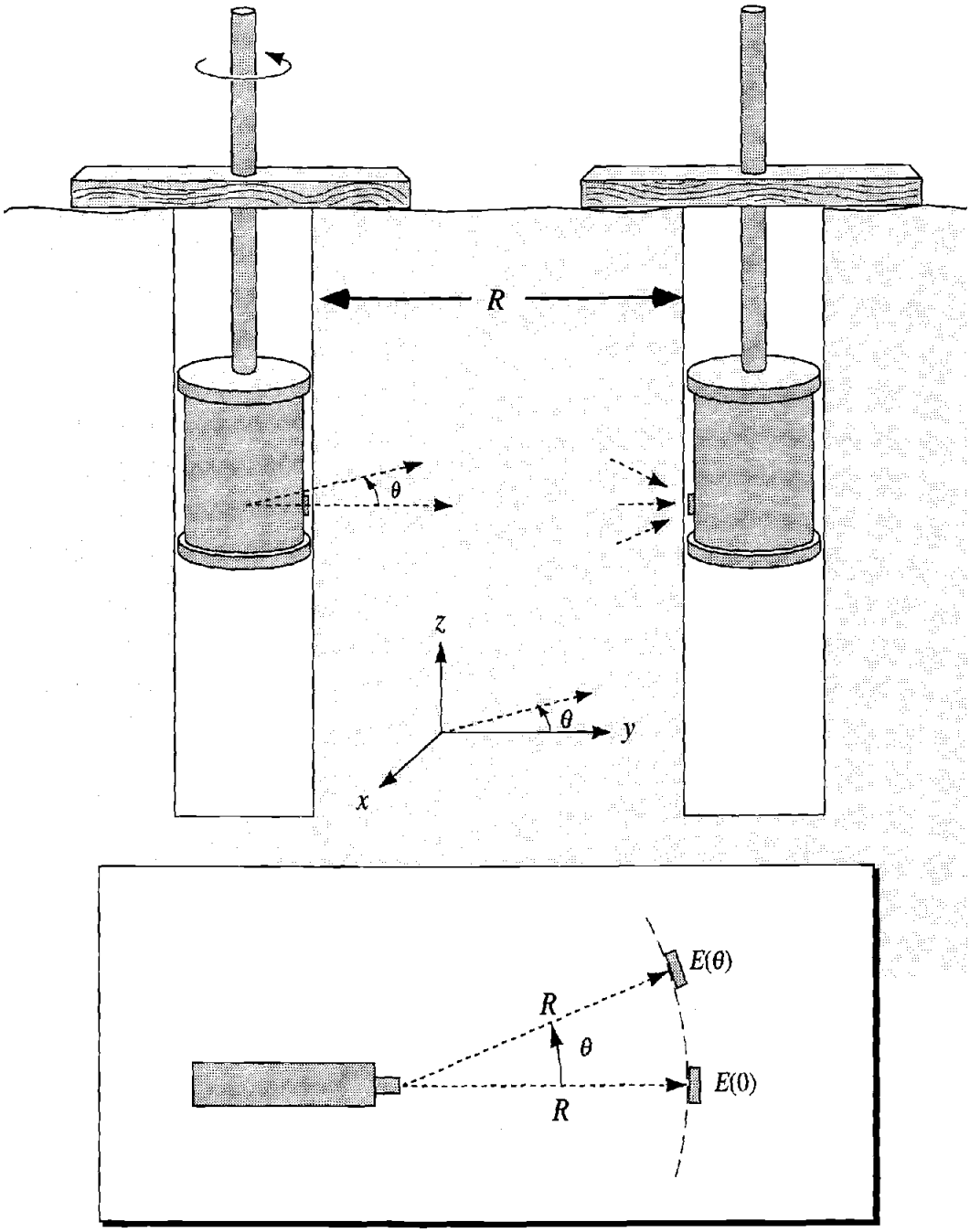

Figure 6.1 Experimental setup for measuring the complete BSF of sea ice *in situ*.

The only assumption in this method is that the medium is isotropic, at least optically. It is well known that sea ice can be anisotropic due to the columnar alignment of the ice crystals during formation. Fractures in the ice, which can channel a light beam, also cause anisotropy. In general, however, the anisotropic structures within sea ice should have a small effect on irradiance-level radiative transfer unless there is high spatial coherence in crystal alignment. The severity of anisotropic effects on the BSF measurements can be characterized in the following manner. By rotating the source beam counter clockwise (looking down), the BSF is measured from 0 to +180 degrees, and by rotating it clockwise, the BSF is measured from 0 to -180 degrees. If the medium is isotropic, a plot of the BSF from -180 to +180 degrees should be a symmetric curve about 0 degrees. As shown in the next section, anisotropic effects do show up in the data, but they are mainly local effects at discrete angles, probably due to light channeling from fractures. These discrete effects can easily be removed or smoothed out since the primary interest here is the overall shape of the BSF. In most cases, the overall shape of the BSF was found to be symmetric.

The optical instrumentation consisted of separate source and detector units housed in water-tight canisters. The light source was a laser diode which emitted approximately 1 mW at a nominal wavelength of 670 nm. The beam had a nominal divergence of 3 mrad as specified by the manufacturer. The laser diode was electronically modulated for phase synchronous detection with the photodetector. The signal from the

photodetector was digitized within its housing and then recorded and displayed on a laptop computer. Both the source and detector housings were built out of a polycarbonate material and were designed to be water-tight since the ice holes sometimes fill with sea water. Unfortunately, this material did not hold up under the stress of the Arctic environment, and one of the canisters often leaked. The optical instrumentation did not incorporate an electronic means, such as an optical encoder, for recording the rotation angle. Thus the BSF was measured at discrete angles, usually in 5 or 10 degree increments, and the angles were measured manually with a protractor and pointer. Approximately 25 to 50 digitized photodetector signals were recorded for each angle and averaged to produce a single value of the BSF at that angle.

The ice coring rig, built by PICO, was specifically designed for the application of measuring in-ice optical properties. When set in place, the rig was able to core a series of holes over a total linear distance of about 1 m. The cores were approximately 15 cm in diameter. The purpose of drilling a series of holes was to make BSF measurements over several different pathlengths. This was accomplished by first drilling two holes with the largest desired separation, making the BSF measurement, and then drilling another hole between these two for a shorter pathlength BSF measurement. The process was repeated until the shortest desired pathlength was achieved, which was typically about 15 cm.

6.4 RESULTS

The measurements presented here were made on shorefast first- and multi-year ice in the Chuckchi Sea near the coast of Barrow, Alaska in April, 1995. These data, although not extensive or comprehensive, have the greatest angular resolution and range, covering $-180 \leq \theta \leq +180$, of the data sets obtained during the 1993, 1994, and 1995 Barrow trips. Comparison of the 1995 data with the 1994 data over the limited angular range of -90° to +90° did not reveal any differences that affect the conclusions presented here. The 1993 experiment was preliminary and mainly for testing the experimental design and instrumentation. The coring rig, optical instruments, and associated equipment were towed to the sites with snow mobiles, where measurements were performed over the course of about a week. The most extensive measurements were made on first-year ice, although some measurements were obtained of a multi-year floe embedded in the first-year ice. BSF measurements were made both as a function of separation distance R and depth z within the ice. The angular range of the BSF measurements usually spanned from 0° to 180°, both clockwise and counterclockwise. Occasionally, time or equipment constraints restricted measurements to one direction, usually counterclockwise (looking down) from 0° to +180°, and in some instances measurements were made to only 90°. Unless stated otherwise, graphs are of data from the first-year site.

The BSF was usually measured in dry holes, although occasionally the holes flooded, either by seepage or because the holes were deliberately drilled down into the water. The inner walls of the holes were generally smooth, but certainly not to optical tolerances so that some effect on the beam as it passed through the ice interface was expected. But hole surface roughness should generally cause only random effects that can be averaged out, and shouldn't cause any significant or systematic effect on the shape of the BSF. These effects should be greatest when the holes are dry due to the larger index of refraction change at the ice interface compared to when the holes are wet. Figure 6.2 shows two BSF's that were measured in the same hole at the same depth when the hole was dry and later flooded with sea water. The

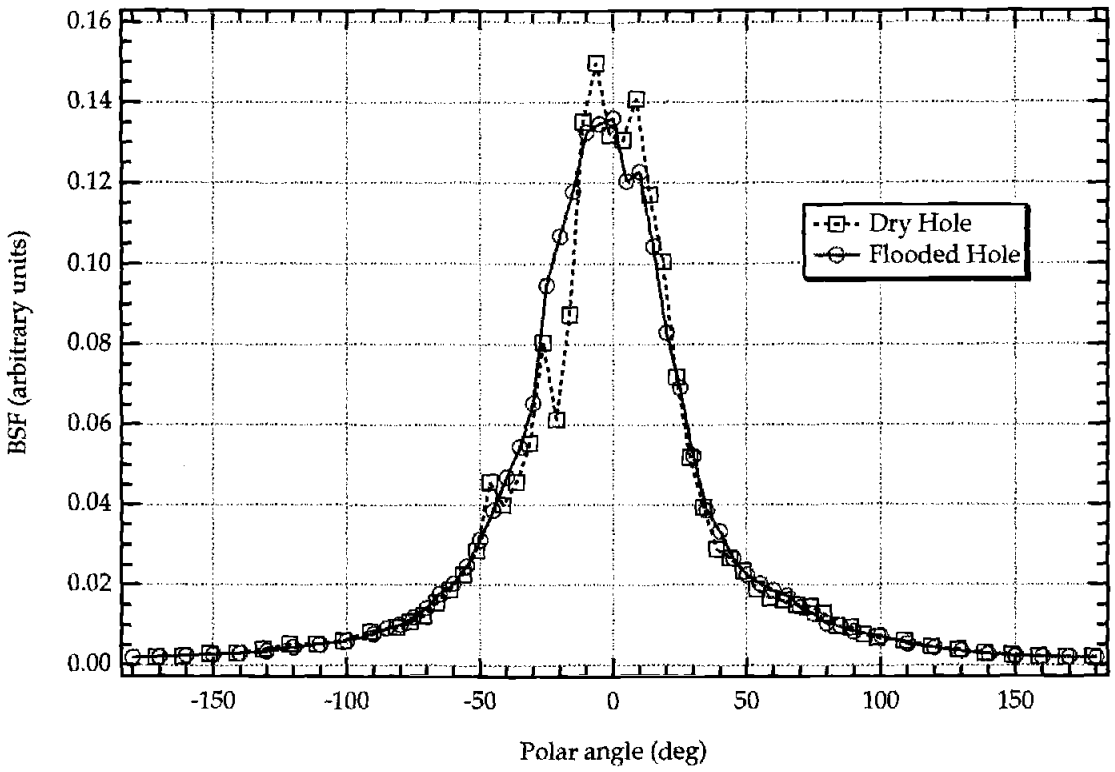

Figure 6.2 Sea ice BSF with the holes dry and flooded with sea water. Pathlength through the ice was R = 30 cm.

pathlength was R = 30 cm. Except for some random differences, the two curves are essentially identical. As expected, the curve with the most variability is the data from the dry hole. Some of the variability is also due, perhaps, to "light channeling" by fractures and brine pockets.

An important feature of all the sea ice BSF's that were measured is their broadness, or angular width, which indicates a high degree of scattering. Indeed, the irradiance of the scattered laser light could be measured when the detector was pointed at 180°. Figure 6.3 shows the BSF of a multi-year floe at two depths, with R = 30 cm. The broadness of these BSF's is again clearly evident and similar to the first-year ice BSF's. Compare this with the PSF,

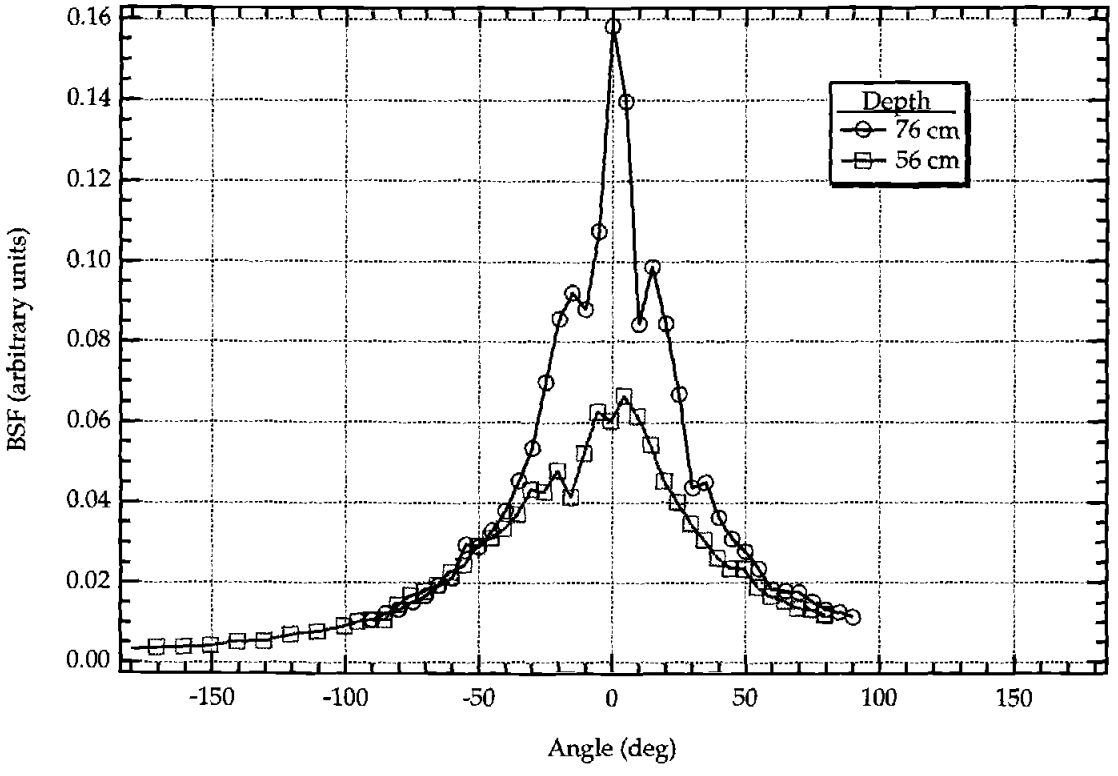

Figure 6.3 Sea ice BSF of multi-year ice at two depths. Pathlength through the ice was R = 30 cm.

which is equivalent to the BSF, of ocean water, shown in Figure 6.4. The ocean water PSF was measured by one of the authors (Maffione) in Monterey Bay, California, using a method similar to that first described by *Honey* [1979] and later used by *Voss and Chapin* [1990] and *Maffione et al.* [1991]. The ocean water PSF is so highly peaked that it must be graphed on a log plot. In the first 30° it decreases by four orders of magnitude, after which the dynamic range of the digital camera begins to be reached. In contrast, the sea ice BSF barely drops by one order of magnitude over 90°. Moreover, there is a large difference in pathlengths between the ocean water PSF and sea ice BSF. The pathlength of the ocean water PSF was 10 m, whereas the sea ice BSF pathlength was 0.30 m. Since multiple scattering increases with pathlength, the highly scattering nature of sea ice, when compared with ocean water at least, is quite dramatic.

Figure 6.5 shows a series of ice BSF's that were measured as a function of depth within the ice, with a pathlength between source and receiver of $R = 30\,\mathrm{cm}$. Again the broad, bell-shaped like curves are evident in all the BSF's. A visual examination of both the core and ice hole revealed layering of the ice sheet. Layers were identified by their slightly darker or more milky appearance compared with other regions of the ice sheet. There was some correlation between the BSF amplitudes and the ice layers, especially where the layer was very distinct, such as near the bottom of the ice sheet corresponding to the 106 cm BSF. The correlation of the BSF amplitudes with the other layers was not as pronounced, although this may have been due to

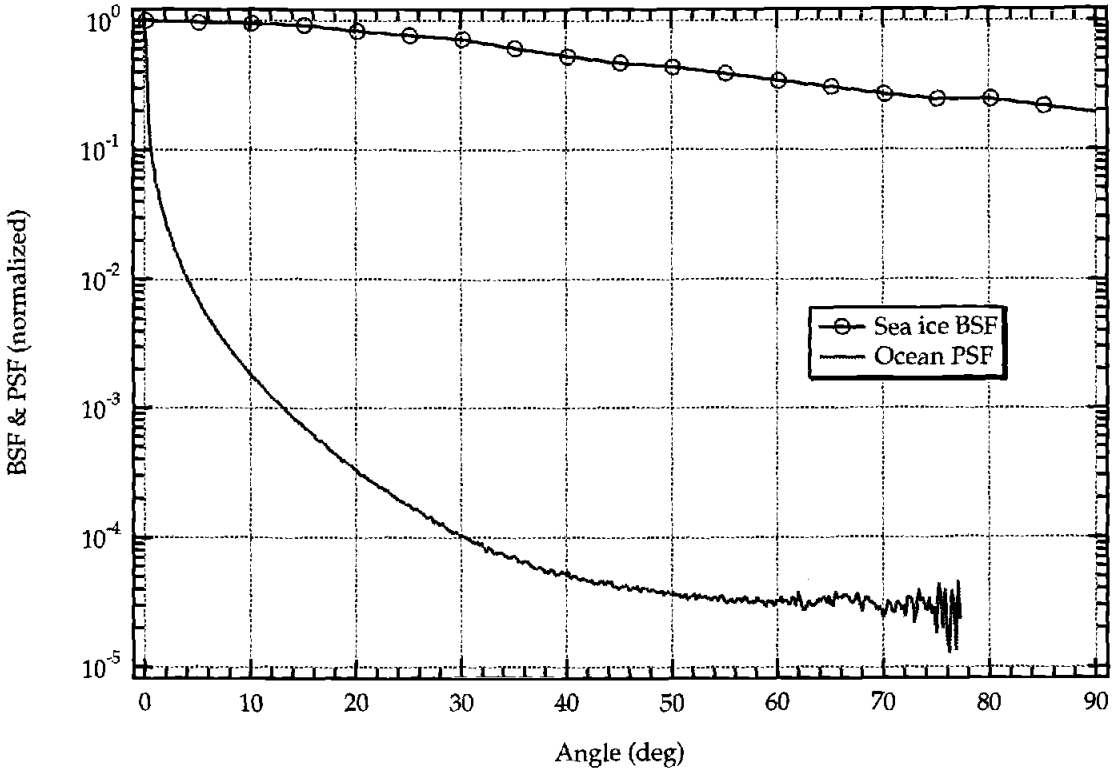

Figure 6.4 Comparison of the BSF of sea ice and the equivalent PSF of ocean water. Sea ice pathlength was 30 cm; ocean water pathlength was 10 m.

the fact that the layers were not characterized in an independent, quantitative manner; layers were observed by visual inspection of the ice cores. No definitive correlation was found between the BSF shapes and the layers.

As already discussed, an important assumption in this technique for measuring the BSF is that the medium is isotropic, at least for light propagation at the irradiance level. Sea ice often forms anisotropic structures, most notably columnar crystals which may align in a predominant direction. Fractures, on certain spatial scales, are anisotropic structures as well. If the spatial coherence of these anisotropic structures is not highly pronounced, then anisotropic effects should average out at the irradiance level of light

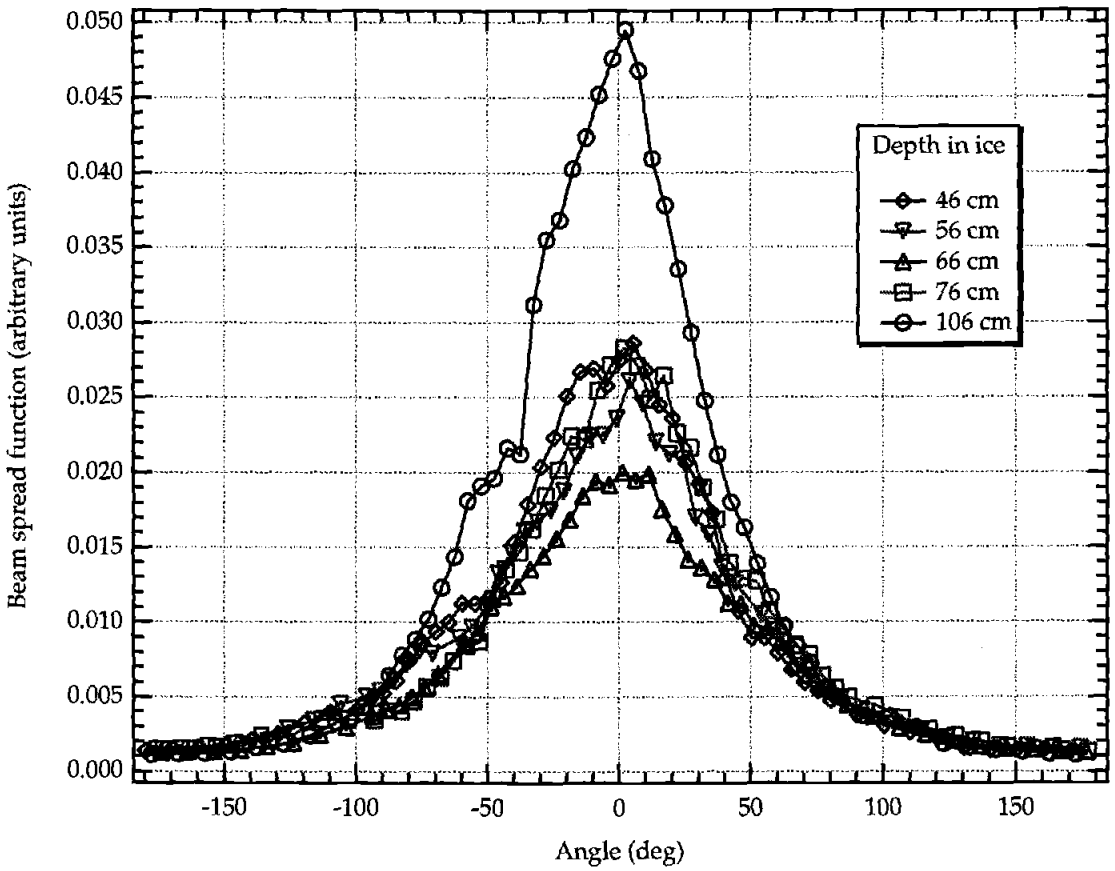

Figure 6.5 The BSF as a function of depth in sea ice. Pathlength was $R = 30$ cm.

propagation. The data shown in Figures 6.2, 6.3, and 6.5 are all relatively symmetric about 0°, save for local variations at discrete angles. Indeed, an examination of all the measured BSF's revealed no systematic asymmetry.

Another dataset which supports the assumption of an isotropic medium for irradiance-level propagation is shown in Figure 6.6. Here one BSF was measured with the 0° beam axis pointing in the direction of the ice C-axis, and the other BSF was measured with the 0° beam axis perpendicular to the C-axis. The experimental arrangement consisted of three holes forming a right angle, with the laser in the vertex hole. Both measurements were made

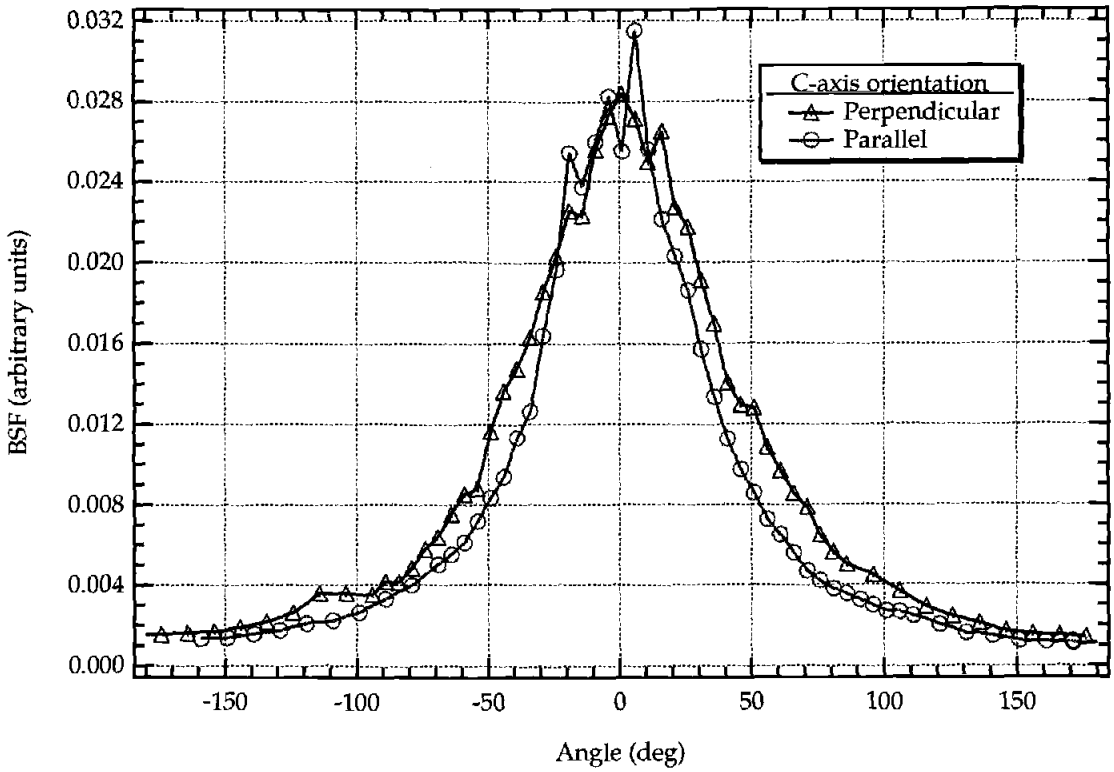

Figure 6.6 The BSF for two different orientations of the 0° beam axis with the C-axis of the ice crystals. Pathlength was R = 30 cm.

at the same depth, 76 cm, and the same pathlength, 30 cm. The two BSF's exhibit symmetry about 0°, and are similar both in shape and amplitude. It is difficult, however, to draw any definitive conclusions by comparing the parallel and perpendicular BSF's because differences may be due to local variability in the ice. Still, the consistent symmetry about $\theta = 0°$ in all the BSF's, even when the 0° beam axis was randomly oriented with respect to the ice C-axis, strongly supports the assumption that sea ice an isotropic medium for irradiance-level propagation.

A potential source of experimental error is the finite size of the holes and instrumentation. In theory, the BSF is the irradiance distribution at a

point in space generated by a point collimated source. Although the source and detector apertures are small compared with other relevant dimensions, the rotation of the source about a total circumference of $2\pi \times 7.5\,\text{cm} \cong 47\,\text{cm}$ introduces a potentially significant pathlength variation between source and detector. Ideally, one would like to measure the BSF using small-diameter holes whose size is insignificant compared with either a diffuse attenuation length, $1/K$, where K is the diffuse attenuation coefficient, or the distance R between the source and detector. Let the measured BSF be denoted BSF_m; then to first order, the measured BSF, denoted BSF_m, can be corrected with the formula

$$\text{BSF}(R,\theta) = \text{BSF}_\text{m}(R,\theta)\exp(r-R)K, \tag{6.1}$$

where

$$r = \sqrt{d(d/2+R)(1-\cos\theta)+R^2}$$

is the linear distance between the source and detector and d = 15 cm is the diameter of the hole. Equation 6.1 simply removes the irradiance attenuation due to the pathlength difference r - R.

To apply the BSF correction, Eq. 6.1, the irradiance attenuation coefficient K needs to be known or estimated. It is defined by

$$K(r,\theta) \equiv \frac{-1}{\text{BSF}(r,\theta)}\frac{\partial \text{BSF}(r,\theta)}{\partial r},$$

so that

$$\text{BSF}(r,\theta) = \text{BSF}(r_0,\theta)\exp\left(-\int_{r_0}^{r} K(r',\theta)\,dr'\right). \tag{6.2}$$

In general, the irradiance attenuation of the direct beam will be larger than the irradiance attenuation of the multiply scattered light from the beam. In other words, $K(r,\theta)$ takes on its maximum value at $\theta = 0°$. Moreover, as r increases, $K(r,\theta)$ will approach a constant for all θ, the asymptotic attenuation coefficient K_∞ [*Preisendorfer*, 1959]. $K(r,\theta)$ can be estimated from measurements of $\mathrm{BSF}(r,\theta)$ at two discrete pathlengths r_1 and r_2 by

$$K(r,\theta) \cong \frac{\ln[\mathrm{BSF}(r_1,\theta)] - \ln[\mathrm{BSF}(r_2,\theta)]}{r_2 - r_1}. \tag{6.3}$$

At $\theta = 0°$, no BSF correction is required since $r = R$. The most accurate estimate of $K(r,\theta)$ is thus expected to be when $\theta = 0°$. A series of BSF measurements, shown in Figure 6.7, were made at three pathlengths, R = 15, 30, and 50 cm. Figure 6.8 shows a plot of $\ln[\mathrm{BSF}(0,R)]$ vs. R, from which K

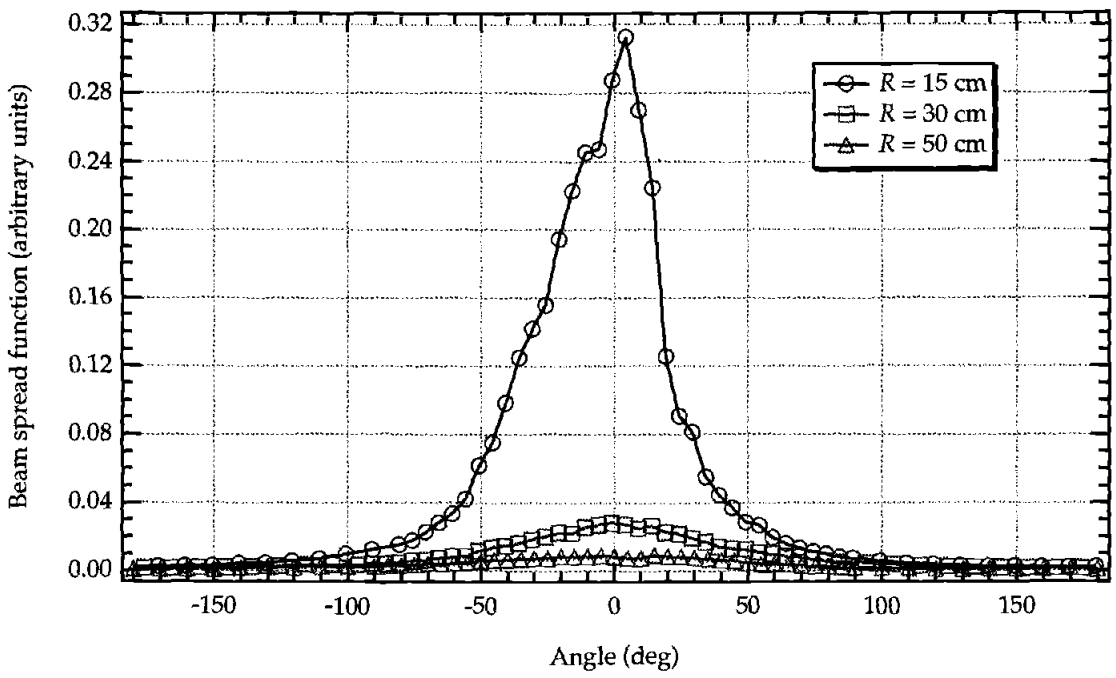

Figure 6.7 BSF as a function of sea ice pathlength R.

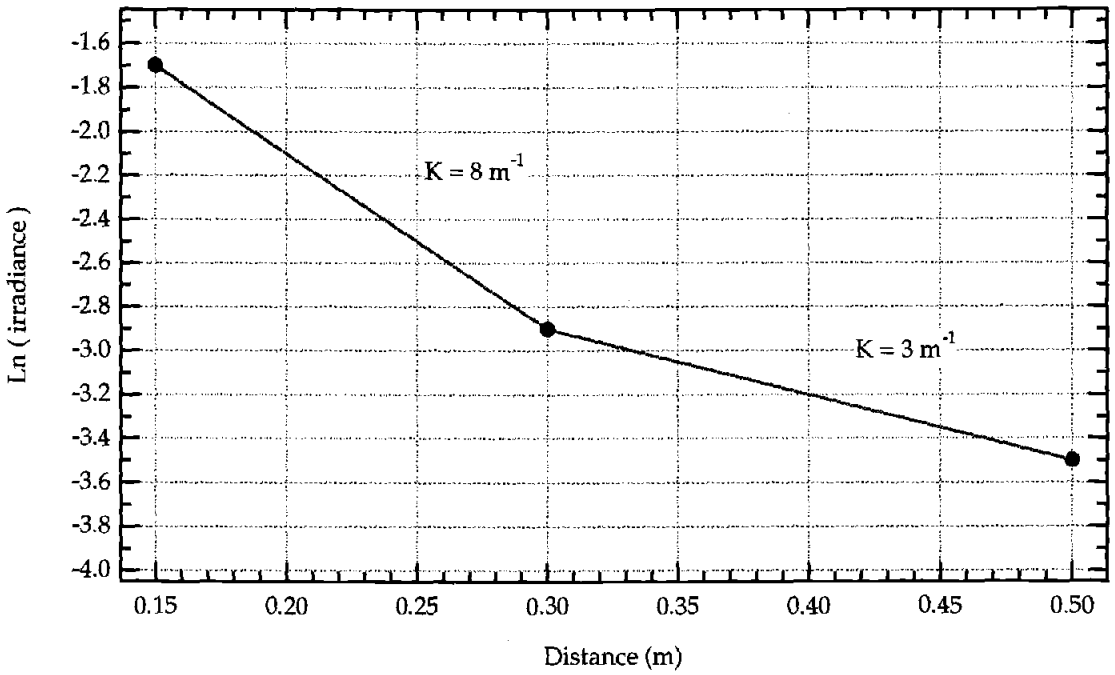

Figure 6.8 Plot of $\ln[BSF(0,R)]$ for the three BSF's in Figure 6.7. K was computed with Eq. 6.3.

was estimated for the two regions, 15 to 30 cm and 30 to 50 cm. As expected, K decreases as R increases. Indeed, this rather dramatic decrease, from $K = 8\ m^{-1}$ to $3\ m^{-1}$ over a change in R of only 35 cm again illustrates the highly scattering nature of sea ice.

The BSF correction, Eq. 6.1, becomes more significant as K increases and R decreases. Thus, for the present data, the largest correction is for $R = 15$ cm and $K = 8\ m^{-1}$. Figure 6.9 shows the corrected and uncorrected BSF for $R = 15$ cm, using a constant value of $K = 8\ m^{-1}$. The correction at small angles is insignificant, since $r \cong R$, and becomes noticeable only at large angles. Nonetheless, the overall shape of the BSF is still not significantly altered. Also, the correction at larger angles is certainly overestimated because, as

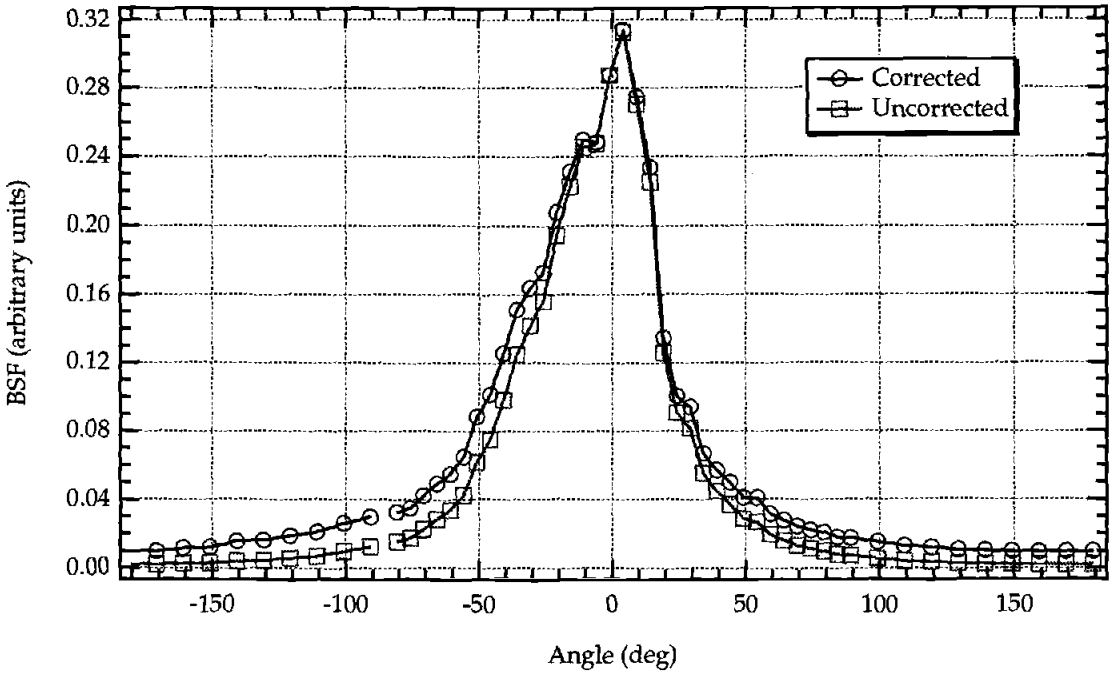

Figure 6.9 Result of applying the correction, Eq. 6.1, to the 15 cm pathlength BSF data in Figure 6.7. This is the most extreme correction and is likely overestimated. For BSF data where $R > 15$ cm, the correction was negligible.

already noted, $K(r,\theta) < K(R,0)$. Indeed, it is likely that $K(r,\theta) \cong K_\infty$ since the BSF at angles other than 0° is diffuse irradiance due to multiply scattered photons. When $K = 3\,\mathrm{m}^{-1}$ was used for $\theta > 30°$, the BSF correction was insignificant. For $R \geq 30$ cm, the BSF correction was negligible even when values of $K > 3\,\mathrm{m}^{-1}$ were used. The conclusion is that the finite size of the instrumentation does not cause any significant change in the measured BSF's, and the correction can be ignored, at least for the present data.

The apparent bell-shaped curve of the BSF's shown in the previous figures suggests a Gaussian function for fitting the data. *Schoonmaker et al.* [1989] used a Gaussian function to fit their laboratory BSF data, which, as described earlier, was actually a paraxial approximation to the BSF as defined

by *Mertens and Replogle* [1977]. A least-squares regression of the BSF data in Figure 6.6 to the Gaussian function

$$\text{Gauss}(\theta) = A\exp\left(-\frac{\theta^2}{2\sigma^2}\right), \tag{6.4}$$

is shown in Figure 6.10. For clarity, only one BSF (perpendicular) is shown, but the results were similar for the other BSF (parallel) as well. Two regressions were performed and shown as the solid curves in Figure 6.10. In one of the regressions, A and σ were both free parameters, and in the other regression A was constrained to the peak value of the BSF data. The best fit occurred when the Gaussian function was constrained to one free parameter,

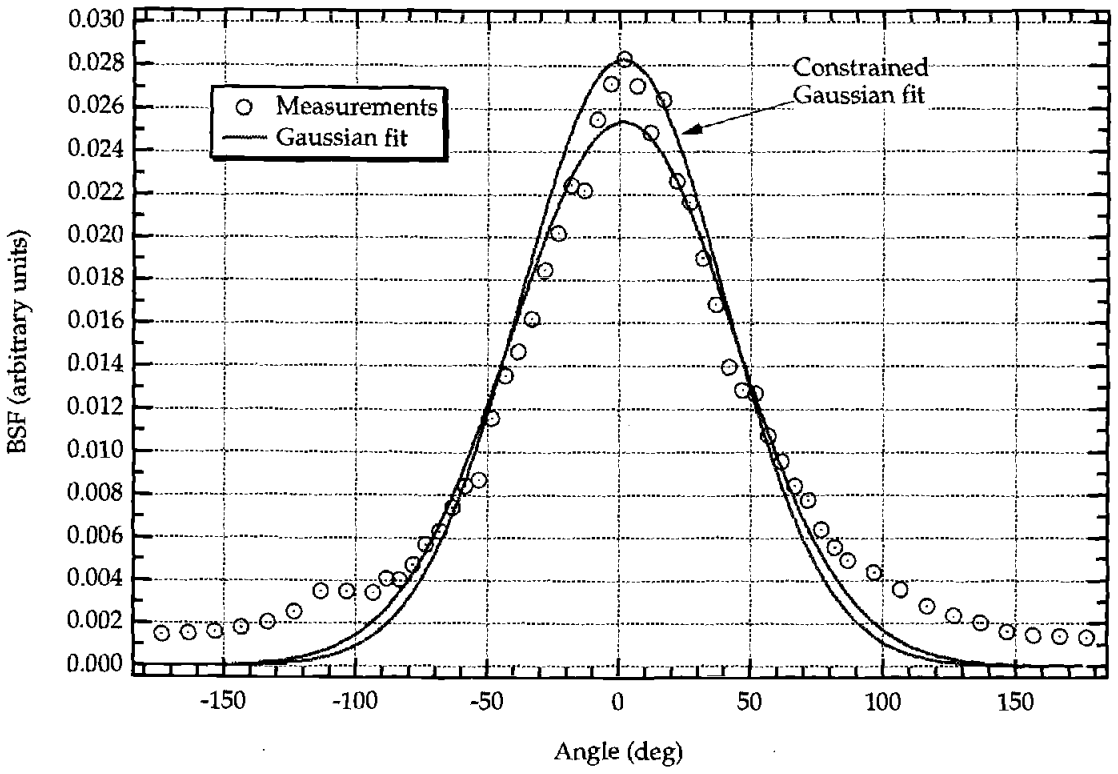

Figure 6.10 Constrained and unconstrained regressions to the BSF in Figure 6.6 (perpendicular) using the Gaussian function, Eq. 6.6.

the standard deviation σ. Nonetheless, even a constrained Gaussian function did not appear to adequately describe any of the BSF data, especially at angles greater than about 80°, which is clearly evident in Figure 6.10.

It was found that all of the BSF data regressed extremely well, over the full angular range , to a Lorentzian function, which can be expressed in the form

$$\mathrm{Lor}(\theta) = \frac{A}{\left[(\theta/\sigma)^2 + 1\right]}, \tag{6.5}$$

where A is the maximum value at $\theta = 0°$ and σ is the half-maximum angle. Figure 6.11 shows the results of fitting a Lorentzian to the same data used in the Gaussian fit shown in Figure 6.10. In the Lorentzian fit, both A and σ were free parameters and the regression gave the values A = 0.028 and $\sigma = 41°$. For the other BSF, where the 0° beam axis was oriented parallel to the ice C-axis, the regression gave the values A = 0.029 and $\sigma = 32°$.

The Lorentzian serves as a useful function for fitting the BSF data to compare their half-maximum angles σ. For example, a regression to the Lorentzian, Eq. 6.5, with the three BSF's in Figure 6.7, yielded the σ values 22°, 42°, 47°, corresponding to the pathlengths 15, 30, and 50 cm, respectively. The increasing width of the BSF with increasing pathlength is due to multiple scattering, but it is again the highly scattering nature of sea ice that rapidly increases the BSF width over such relatively short pathlengths. A 200% change in σ occurred over a 15 cm change in R, from 15 to 30 cm. Note, however, that the next 20 cm change in R, from 30 to 50 cm, yielded a 12%

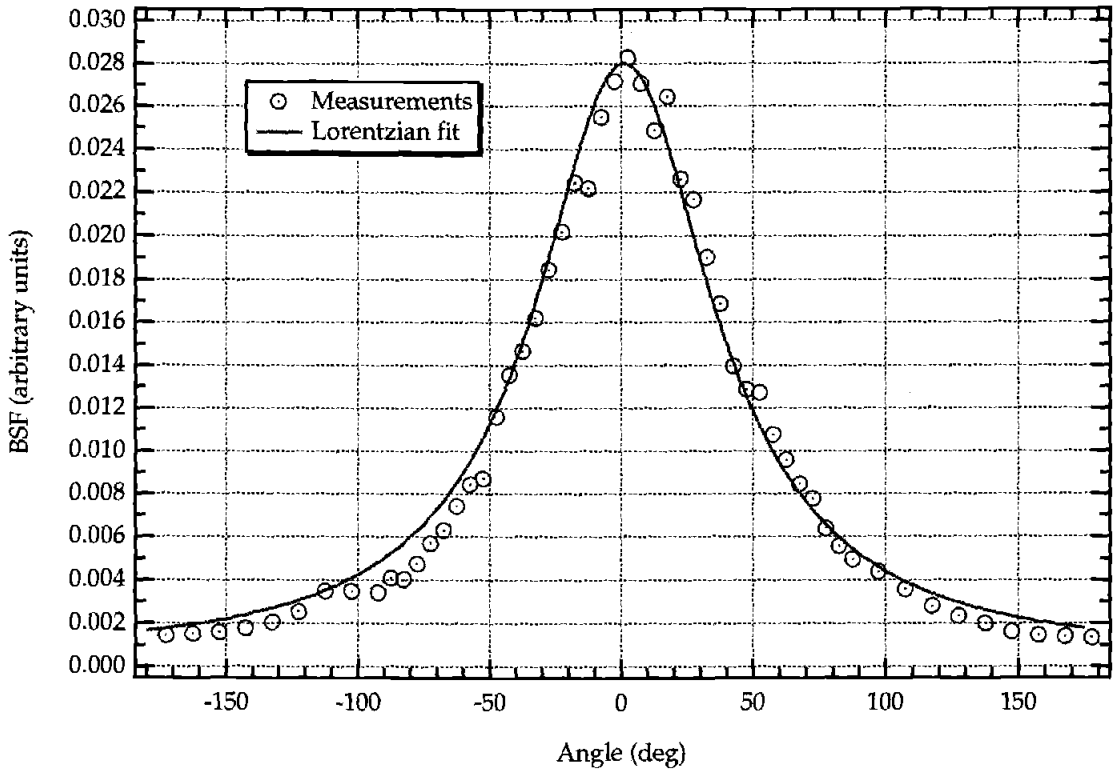

Figure 6.11 Result of regressing the BSF data in Figure 6.10 to a Lorentzian function, Eq. 6.5.

change in σ. This sharply decreasing change in σ indicates the rapid approach, over relatively short geometrical distances, of the BSF towards its asymptotic, constant shape.

6.5 DISCUSSION

The ultimate objective of the present work is to better understand the optical nature of sea ice and to develop practical models for describing and predicting radiative transfer in sea ice. The physically complex nature of sea ice makes modeling it from first principles nearly impossible. Moreover, single scattering approximations can not be used because, as shown above and by the work of others, sea ice is a highly scattering medium. This also

complicates the direct measurement of IOP's. The highly scattering nature of sea ice may, however, allow for the application of some useful simplifications in the theory of radiative transfer.

Asymptotic radiative transfer theory predicts that the radiance distribution, once asymptotic, does not change its shape and decays in amplitude as $\exp(-K_\infty R)$, where K_∞ is the asymptotic attenuation coefficient. The theory also predicts that both the shape of the radiance distribution and K_∞ are functions of only the IOP's of the medium and are independent of the boundary conditions [*Priesendorfer*, 1959]. Thus, for a given set of IOP's, the asymptotic radiance distribution and K_∞ are uniquely given regardless if the light field is generated by solar illumination or a submerged source. Therefore, the asymptotic radiance distribution due to a submerged source is identical to the asymptotic radiance distribution for plane wave illumination at the boundary of the medium, such as solar illumination on the surface of the ocean, or in this case sea ice.

As explained earlier, the PSF is the radiance distribution due to a Lambertian source and, by reciprocity, so is the BSF. The sea ice BSF measurements are thus equivalent to the in-ice radiance distribution due to a submerged Lambertian source. In general, sea ice is a far more highly scattering medium than ocean water, so that the asymptotic state is approached much more rapidly in sea ice. This is true not only in terms of geometrical distance, but also in terms of optical pathlength $\tau \equiv R/c$, where c is the beam attenuation coefficient. Over a given optical pathlength, more

scattering events occur in a medium with a high single scattering albedo $\omega_0 = b/c$, where b is the total scattering coefficient, than in a medium with a lower ω_0. How far from the source the light field becomes asymptotic, in terms of τ, depends mainly on ω_0, and to a lesser extent on the scattering phase function [*Gordon et al.*, 1993]. But in terms of geometrical distance R, the dependence is mainly on the absolute value of b.

The BSF measurements as a function of pathlength, shown in Figure 6.7, strongly suggest that the BSF is closely approaching the asymptotic radiance distribution for R > 30 cm. As shown in Figure 6.8, the irradiance attenuation appears to be approaching an asymptotic limit that is probably close to $K = K_\infty \cong 2\ m^{-1}$. The change in the shape of the BSF, as measured by σ, is also rapidly approaching an asymptote. As noted earlier, σ changed by 200% from 15 to 30 cm, but then changed by only 12% from 30 to 50 cm. The definitive test is to compare the BSF to the asymptotic radiance distribution, $L_\infty(\theta)$, for the appropriate choice of IOP's. $L_\infty(\theta)$ is uniquely determined by ω_0 and the scattering phase function, $\tilde{\beta}(\psi)$, where ψ is the scattering angle.

The asymptotic radiance distribution, $L_\infty(\theta)$, can be computed accurately using an eigenmatrix method which is incorporated into a numerical radiative transfer model called Hydrolight [*Mobley*, 1995]. To properly compare $L_\infty(\theta)$ with the BSF, ω_0 and $\tilde{\beta}(\psi)$ of the sea ice needs to be known or estimated. From Monte Carlo radiative transfer calculations of highly turbid

water, *Kirk* [1994] found that K_∞ can be accurately related to a, the absorption coefficient, and b by

$$K_\infty = \sqrt{a^2 + Gab}, \tag{6.6}$$

where G is a regression parameter. Kirk reported the value of $G = 0.233$ for the highly scattering cases, and for all cases which covered the range $0.5 \le \omega_0 \le 0.995$, he reported an average value of $\overline{G} = 0.245$. Based on the results shown in Figure 6.7, K likely falls within the range $8\ \mathrm{m}^{-1} \le K \le 2\ \mathrm{m}^{-1} \cong K_\infty$, with the lower value applying to $R > 50$ cm.

At 670 nm, a for ocean water is predominantly determined by pure water absorption and, to a lesser degree, by chlorophyll, except when concentrations are extremely high. For pure water, $a(670) \cong 0.43\ \mathrm{m}^{-1}$ [*Smith and Baker*, 1981]. Although phytoplankton were embedded in the ice, their concentrations were not high and probably contributed no more than 0.2 m^{-1}, and at most 0.3 m^{-1}, to $a(670)$. Thus for sea ice, a reasonable range for $a(670)$ is $0.43\ \mathrm{m}^{-1} \le a \le 0.73\ \mathrm{m}^{-1}$. Any temperature dependence on $a(670)$ is negligible [*Trabjerg and Højerslev*, 1996], especially compared with the variability in phytoplankton absorption.

Solving Eq. 6.6 for b gives

$$b = \frac{K_\infty^2 - a^2}{Ga}, \tag{6.7}$$

which is used to compute $c = a + b$ and $\omega_0 = b/c$. The beam attenuation coefficient c is plotted in Figure 6.12 for different values of a spanning the range $0.43\ \mathrm{m}^{-1} \le a \le 0.73\ \mathrm{m}^{-1}$, with $G = 0.233$. For K_∞ between 2 and 3 m^{-1}, c

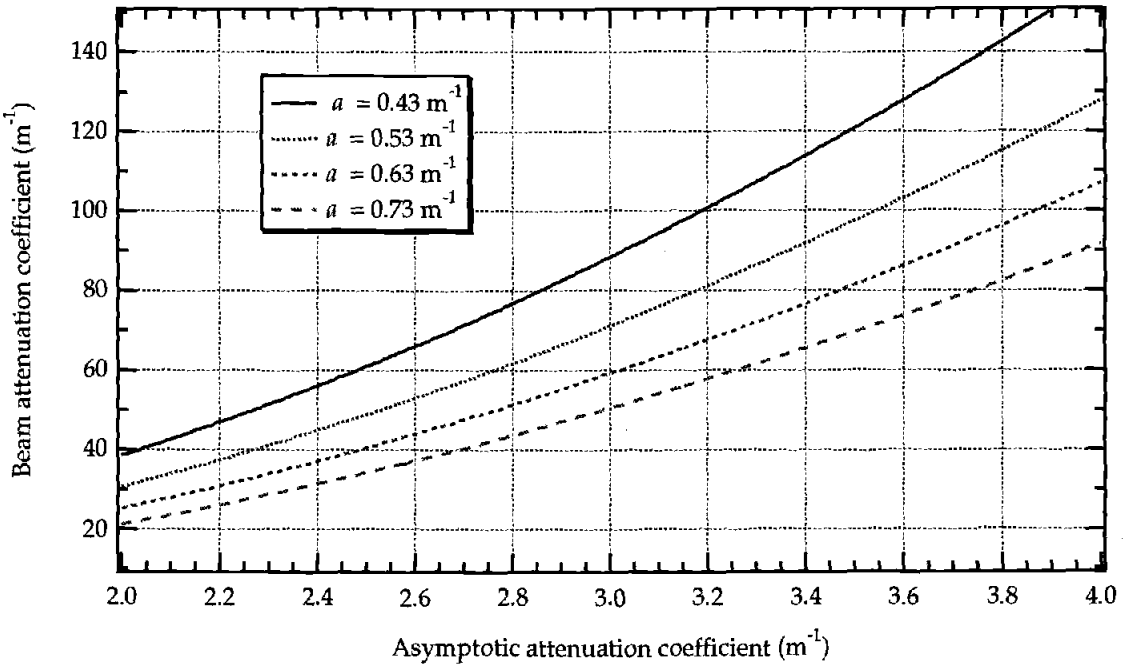

Figure 6.12 Computation of $c = a + b$ as a function of K_∞, for four values of a, using Eq. 6.7 to calculate b.

ranges from 20 to 90 m^{-1}. Assuming a likely value of $a(670) \cong 0.53\ m^{-1}$ gives $c \cong 50\ m^{-1}$ for $K_\infty = 2.5\ m^{-1}$. Plots of ω_0 are shown in Figure 6.13 for the same four values of a used for Figure 6.12. The results confirm that $\omega_0 > 0.95$, and is probably greater than 0.98 for the likely values of a and K_∞.

The remaining IOP to be estimated is the scattering phase function $\tilde{\beta}(\psi)$. Because the inhomogeneities in sea ice that cause scattering are predominantly large compared to visible wavelengths, $\tilde{\beta}(\psi)$ is expected to be a highly forward-peaked scattering-phase function. Measurements of scattering by ice confirm this [*Grenfell and Hedrick*, 1983; *Miller et al.*, 1994]. A useful form for $\tilde{\beta}(\psi)$ is the *Henyey-Greenstein* [1941] phase function, namely

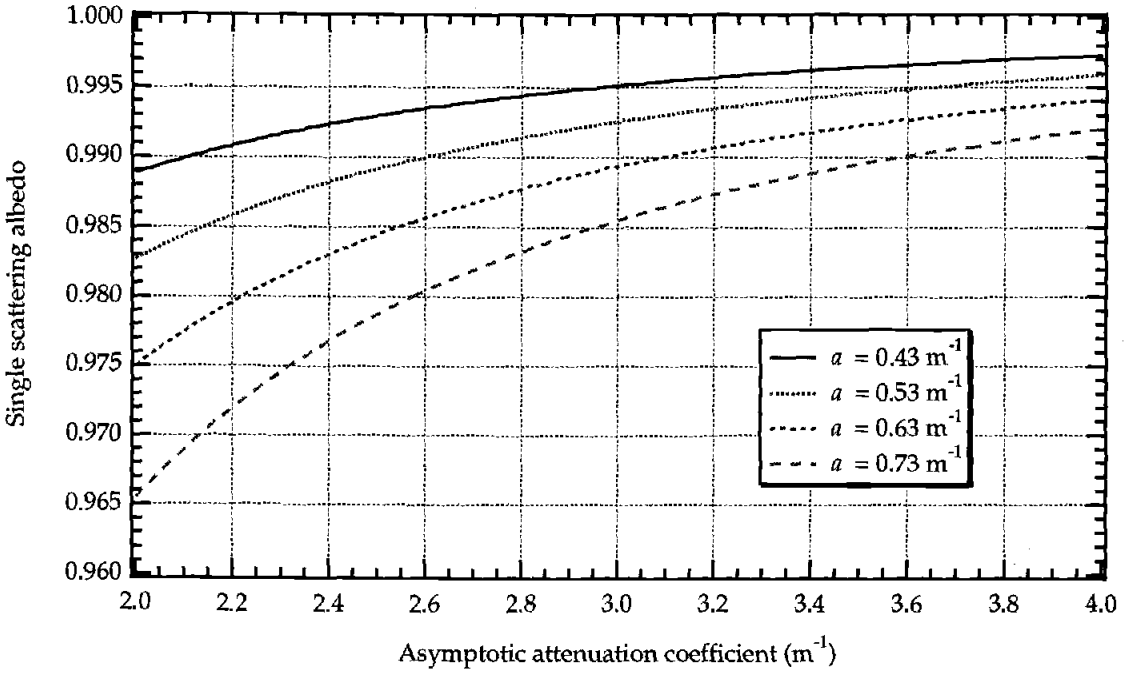

Figure 6.13 Computation of $\omega_0 = b/c$ as a function of K_∞ using Eq. 6.7 to calculate b. The same four values of a are used as in Figure 6.12.

$$\tilde{\beta}(\psi) = \frac{1}{4\pi} \frac{1-g^2}{\left(1+g^2-2g\cos\psi\right)^{3/2}}, \tag{6.8}$$

where g is the average cosine of the scattering angle for $\tilde{\beta}(\psi)$, otherwise known as the asymmetry parameter, defined by

$$g \equiv 2\pi \int_{-1}^{1} \tilde{\beta}(\psi)\cos\psi \, d(\cos\psi).$$

Monte Carlo calculations of radiative transfer in the ocean show that irradiance propagation is only weakly dependent on the shape of $\tilde{\beta}(\psi)$ in the near-forward direction (< 30°) [*Gordon*, 1993]. Therefore K_∞ should not be a strong function of $\tilde{\beta}(\psi)$, and neither should the shape of the asymptotic radiance distribution $L_\infty(\theta)$, since it consists only of photons that have scattered at least once, and more likely have undergone many scattering

events. So regardless of the fine details of $\tilde{\beta}(\psi)$, the H-G phase function, Eq. 6.8, should be adequate for irradiance-level and asymptotic computations of the light field in sea ice.

It remains then to estimate g, the asymmetry parameter of the phase function. As previously shown, ω_0 of sea ice is generally greater than 0.95, and is likely 0.98 or greater for the sea ice of which the BSF measurements were made. The high ω_0 of sea ice suggests that photon diffusion theory may adequately describe radiative transfer in sea ice. In the asymptotic limit, photon diffusion theory predicts that

$$K_\infty = \sqrt{3a(c - gb)}. \tag{6.9}$$

(See *Maffione* [1996] for a complete derivation and discussion of this equation.) Equating Eq. 6.9 to Kirk's result, Eq. 6.6, and solving for g gives

$$g = \frac{2/\omega_0 - G + 1}{3}, \tag{6.10}$$

which is plotted in Figure 6.14 over the range, $0.95 \le \omega_0 \le 1$. For $\omega_0 \cong 0.98$, Eq. 6.10 predicts $g \cong 0.935$.

The asymptotic radiance distribution was computed with Hydrolight using an H-G phase function with g = 0.935, $\omega_0 = 0.98$, and a = 0.58 m^{-1}. Figure 6.15 shows the results, with $L_\infty(\theta)$ plotted over the BSF measured at $R = 50$ cm. The dotted line is the regression of the data to a Lorentzian, Eq. 6.5. Clearly, $L_\infty(\theta)$ matches the BSF quite well and confirms that the BSF is indeed closely approaching the asymptotic radiance distribution.

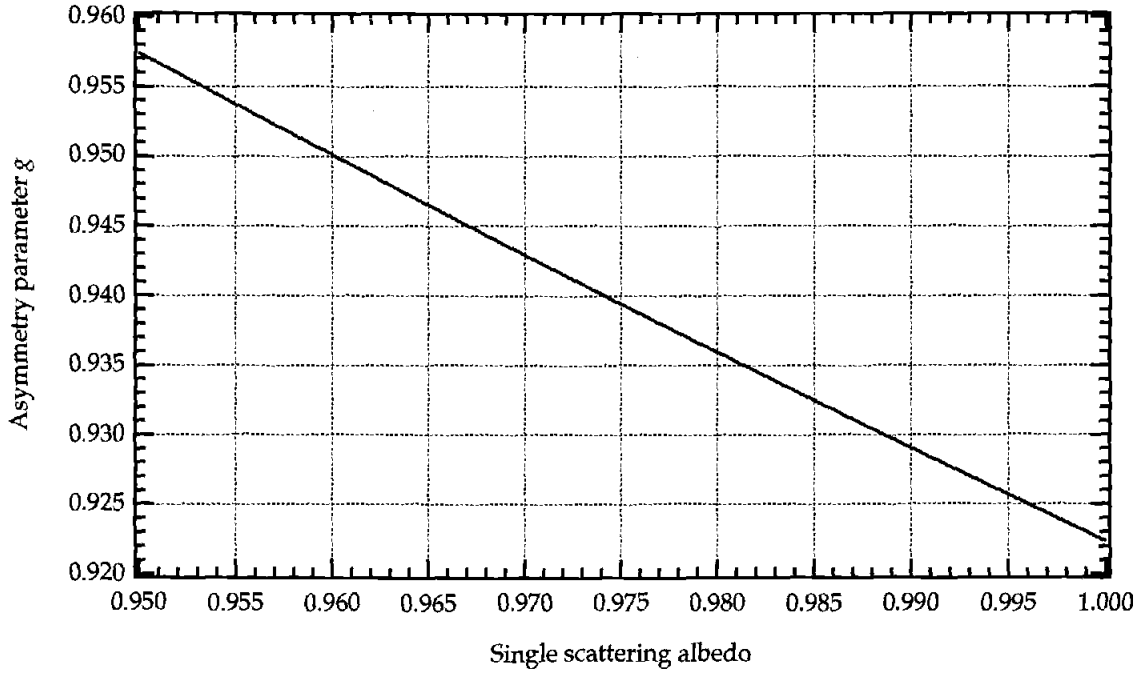

Figure 6.14 Asymmetry parameter g computed with Eq. 6.10 using $G = 0.233$.

6.6 CONCLUSIONS

A new method for measuring profiles of the BSF of sea ice also yields the complete (axially symmetric) radiance distribution due to a submerged Lambertian source. The BSF of sea ice is significantly different than the BSF of ocean water due to the highly scattering nature of sea ice. Based on an equation developed by Kirk for highly turbid water, and estimates of K_∞ and a for sea ice in the visible spectrum, sea ice can generally be expected to have a single scattering albedo $\omega_0 > 0.97$. The high ω_0 of sea ice suggests that photon diffusion theory can adequately describe radiative transfer in sea ice, at least at the irradiance level. Combining a result of this theory with Kirk's equation predicts that the asymmetry parameter g of the scattering phase function is

approximately in the range $0.9 \leq g \leq 0.95$. An exact computation of the asymptotic radiance distribution matched quite well the measured BSF at a pathlength of 50 cm, strongly suggesting that the BSF rapidly approaches, over geometrical distances, the asymptotic radiance distribution. Thus, for sufficient pathlengths, both asymptotic radiative transfer theory and photon diffusion theory can be used to interpret BSF measurements of sea ice. Application of these theories provide useful relationships for estimating sea ice IOP's, such as K_∞, ω_0, and g.

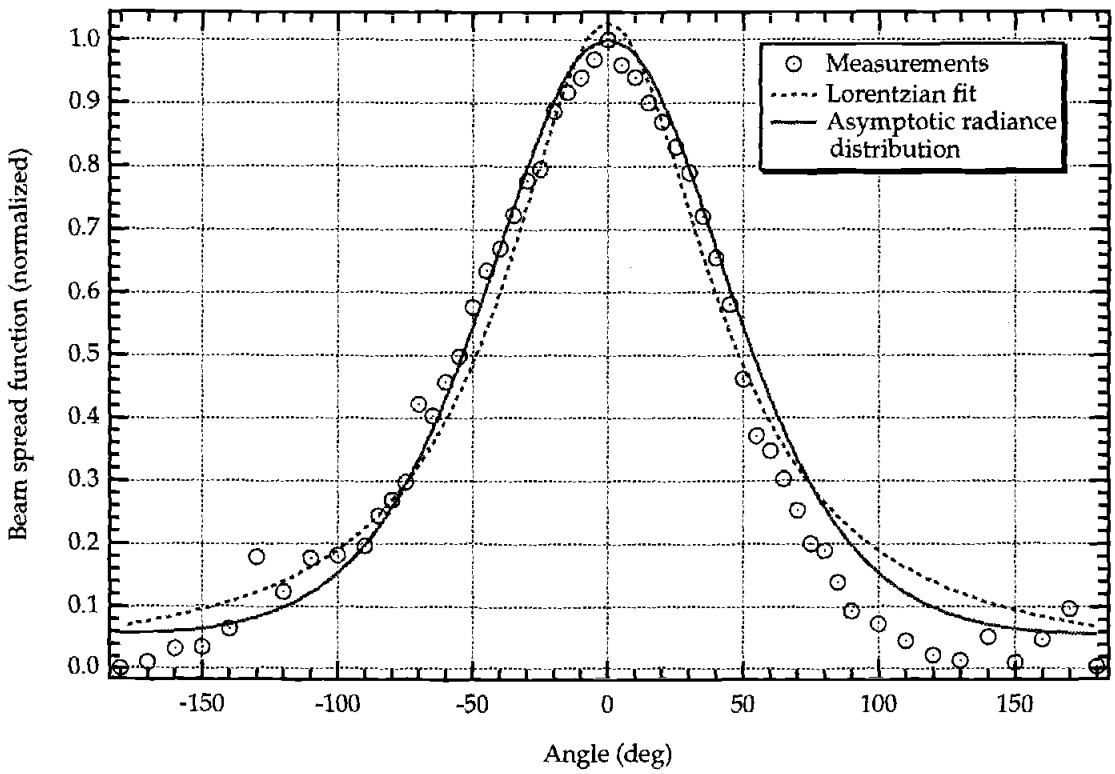

Figure 6.15 Comparison of computed asymptotic radiance distribution with the measured BSF for the pathlength $R = 50$ cm.

Chapter 7

7. CONCLUSIONS

7.1 Summary

It was stated in the introduction that theoretical advances have far outpaced experimentation in optical oceanography. New models and analytical relationships among ocean-optical properties appear in journals practically on a monthly basis. Yet in most cases these models are based on numerical simulations or, at best, scant data sets that almost never include both input and output model parameters (i.e., closure is not achieved). Many ocean-optical properties remain to be empirically characterized and understood, and without the means to do so, experiments for testing theoretical advances are impossible. It is the author's hope that this thesis has helped in some small measure to bridge the wide gap between theory and experiment in optical oceanography.

Ocean-color remote sensing (OCRS) is poised to emerge as one of the most, if not the most, powerful tool for studying global-ocean primary production. The usefulness of this tool relies not only on the ability of the sensors themselves, but also on the models needed for interpreting the remotely-sensed signals. Ultimately, these models involve inherent and apparent optical properties of the ocean. For OCRS models, the two primary IOP's are the spectral absorption coefficient $a(\lambda)$ and the spectral backward scattering coefficient $b_b(\lambda)$, since, as is well known, the remotely-sensed

reflectance is proportional to $b_b/(a+b_b)$. Although $a(\lambda)$ has been measured for decades with a variety of instruments and methods, surprisingly little attention has been given to measuring $b_b(\lambda)$ — until recently.

Chapter 2 presented new instruments and methods for routinely measuring $b_b(\lambda)$ *in situ*. These instruments and methods involved fixed-angle backscattering sensors. A rigorous analysis showed that these sensors can be calibrated with reference to an NIST traceable reflectance standard, and the calibration provides a measurement of $\beta(\psi*)$ accurate to within a few percent of the true $\beta(\psi*)$ when the sensor's response function, $W(z;c)$, is properly characterized. A complete procedure was given for determining $W(z;c)$. Once $W(z;c)$ is known, the centroid angle of scattering, ψ^*, for that sensor can be determined. It was shown that, depending upon the design of the sensor, ψ^* can change by 10° or more for drastic changes in the attenuation of the water..

Since a fixed-angle backscattering sensor, when properly calibrated, measures $\beta(\psi^*)$, a procedure for converting this measurement to an estimate of b_b is needed. An analysis was performed of the conjecture that b_b can be estimated with a measurement of the VSF at a single angle in the backward hemisphere. Oishi's analysis of this conjecture [*Oishi*, 1990] concluded that $1.14\times 2\pi\beta(120°)-0.43\times 10^{-4}\,\mathrm{m}^{-1}$ provides the best estimate of b_b for the computed and observed scattering functions he considered. However, he also reported that $1.08\times 2\pi\beta(140°)-1.62\times 10^{-4}\,\mathrm{m}^{-1}$ gives the least maximum likely

error in estimating b_b. VSF measurements by *Petzold* [1972] were examined in this thesis, where it was argued that his turbid water measurements were probably systematically low in the backward hemisphere because they were not properly corrected for light attenuation by the water. When the turbid water measurements were excluded in the type of analysis performed by Oishi, it was found that estimating b_b from $\chi 2\pi\beta(\psi_\chi)$, where χ is a constant for the particular angle ψ_χ, there was no statisically significant difference between using $\beta(120°)$ or $\beta(140°)$, or even VSF values between these angles. The expression $b_b \cong 1.1\times 2\pi\beta(140°)$ was suggested as providing the best estimate of b_b from measurements of $\beta(\psi^*)$ using the BB-4, where ψ^* is nominally 140°.

Optical remote sensing of the oceans includes not only passive ocean-color remote sensing but also active remote sensing with lidar. These are two entirely different methods with their own sets of problems. Airborne oceanographic lidar (AOL) typically involves a monostatic laser transmitter and narrow-angle receiver. The upper ocean is essentially "pinged" with a pulse of highly collimated monochromatic light, and the "impulse response" of the ocean is recorded as the directly backscattered light of the pulse by the ocean. As with OCRS, AOL is useful only when there are appropriate models for interpreting the light signals. For AOL, the two primary IOP's are $\beta(\pi)$ and c (analogous to b_b and a for OCRS). Although c has been routinely measured, no direct measurements of $\beta(\pi)$ had ever been made until the

work presented in Chapter 3, and some previous work by *Maffione and Honey* [1992].

In addition to the application to AOL, the VSF at and near 180° is of theoretical interest. It has been hypothesized, based mainly on Mie calculations, that the VSF could rise sharply from 170° to 180°, depending on the nature and size distribution of the marine particles. There was also some conjecture that enhanced, coherent backscattering might occur at 180° for a laser beam. The results presented in Chapter 3, based on measurements made in the Gulf of Mexico near Panama City, Florida, revealed that the VSF increased by more than 50% from 179 to 180°. A sharp enhancement, possibly due to coherent backscattering, was also observed at 180° with an angular width of about 0.03°. Measurements made at six discrete wavelengths from 457 to 532 nm revealed that the spectral dispersion of backscattering at and near 180° was substantially greater than the dispersion at 135° measured with multispectral bi-static backscattering sensors. These results have direct implication to both the AOL models and the calibration of these lidar systems.

The spectral absorption coefficient $a(\lambda)$ is important to all areas of optical oceanography and plays a central role in bio-optical oceanography and OCRS, as noted earlier. *Gershun* [1939] first proposed a method for measuring a which involved measuring scalar irradiance and the attenuation of vector irradiance due to solar illumination of the ocean. Assuming no internal sources and elastic scattering only, Gershun's equation is exact and provides a practical means for measuring a. Curiously, Gershun's exact method had to

wait 40 years before it was correctly pursued by *Højerslev* [1976] and later by *Spitzer and Wernand* [1980]. Yet none of these researchers carried out any further, systematic work with Gershun's method. *Sorenson and Honey* [1968] and *Duntley* [1971] apparently were the first to suggest using a submerged isotropic light source to determine a that is, in retrospect, an extension of Gershun's method. But there is nothing in their published work to suggest that they understood the connection to Gershun's equation, and their results were not rigorously derived or completely accurate.

Chapter 4 gave the first rigorous derivation of the equation which relates the absorption coefficient to the scalar irradiance and attenuation of net "radial" irradiance due to a submerged isotropic light source (ILS). Interestingly, it was found that Sorenson and Honey's result was an approximation in the near field, that is, within a few attenuation lengths of the source, and Duntley's result was an approximation in the far field, or asymptotic limit, far from the source. Equation 4.20 is, like Gershun's equation, exact but requires only the assumption of homogeneity in the IOP's. It was shown that the one-dimensional form of Gershun's equation is obtained in the asymptotic limit as the distance from the source goes to infinity.

The ILS method has many advantages over Gershun's method, as well as many other methods, for determining the (total) absorption coefficient, although it certainly has its disadvantages as well. One powerful advantage is that the experimental conditions can be controlled quite well. For example,

both the light source and irradiance detectors can be spectrally filtered, so that (other) internal sources and inelastic scattering effects can be quantified, or mitigated without any loss in accuracy. Another advantage, as demonstrated in Chapter 5, is that the average cosine of the light field due to an ILS decreases slowly from unity as the distance from the source increases. Moreover, the backward-scattered irradiance is only a tiny fraction of the outward flowing irradiance from the source. Consequently, a can be determined accurately from measurements of only the outward flowing (radial) irradiance, which is a relatively easy measurement to make. Another, often overlooked though important advantage, is that the ILS method, like Gershun's method, determines the absorption coefficient of ocean water in its natural, "undisturbed" state, unlike methods that require filtering or flow-through systems. The major disadvantage is that the ILS method, like Gershun's method, is strictly an *in-situ* method that does not directly lend itself to determining the absorption coefficient of the individual water constituents.

Chapter 5 directly extended the results of the previous chapter with an investigation of the average cosine, $\bar{\mu}$, of the light field due to an ILS. This AOP is fundamental to nearly all studies of the submarine light field, whether the light field is due to solar illumination or a submerged light source. In the latter case it was shown that $\bar{\mu} \to 1$ as the distance to the source approaches zero, and decays slowly to its asymptotic limit as the distance goes to infinity. The light field due to a submerged ILS was simulated with a

Monte Carlo model. The simulated radiance distributions, or point spread functions (PSF), were compared with measurements of the PSF made in Lake Pend Oreille, Idaho. It was found that the log-log slopes of the PSF's changed nearly identically as a function of optical pathlength τ from the source. Differences could be attributed to measurement errors and uncertainties about the optical properties of the water. Simulations of $\bar{\mu}(\tau)$ could be accurately modeled with a simple exponential function of τ where the coefficients depended on both the single scattering albedo and the VSF. A somewhat surprising finding was that the light field due to a submerged ILS did not approach its asymptotic state at 20 optical pathlengths, in strong contrast to the case of solar illumination where the daylight field is nearly asuymptotic at 5, or at most 10, optical pathlengths.

Ocean water in its frozen state is a radically different optical medium than the liquid ocean. Understanding optical propagation in sea ice presents a unique set of challanges in optical oceanography due to the complex physical structure of sea ice, its solid state, and the harsh working environment. Although the AOP's of sea ice can be determined using similar, albeit modified, methods used in the ocean, most IOP's of sea are nearly impossible to measure directly. Chapter 6 presented a new method for characterizing the optical properties of sea that may have universal application to highly-scattering media. The technique involves measuring the in-ice beam spread function (BSF) which, by reciprocity, is the radiance distribution due to a submerged Lambertian source, also known as the point spread function.

Measurements definitively demonstrated that sea ice is a highly scattering medium, with a single scattering albedo ω_0 generally greater than 0.97. The highly scattering nature of sea ice causes the PSF to rapidly approach the asymptotic radiance distribution. The asymptotic state, together with a high ω_0, justifies the application of photon diffusion theory for optical propagation in sea ice. Equating results from diffusion and asymptotic radiative transfer theory yields a simple yet important relationship between the asymptotic attenuation coefficient and the sea ice IOP's. This relationship includes the phase function asymmetry parameter g, which is important for characterizing the sea ice VSF for modeling purposes. It is thus possible to determine g from measurements of the BSF as a function of pathlength using the method described in Chapter 6.

7.2 Future Research

The development of a spectral backscattering sensor that is calibrated to measure $b_b(\lambda)$ is a new and important advance in optical oceanography. Previously, $b_b(\lambda)$ was determined from painstaking measurements of $\beta(\psi)$ with general-angle scattering meters that are rarely in use. Now $b_b(\lambda)$ can be as easily and routinely measured as temperature and salinity are with a commercial CTD. Spectrophotometric measurements of $a(\lambda)$ have provided much information about the nature of marine particles, most notably phytoplankton, and $b_b(\lambda)$ complements these measurements, yielding information about particle size distributions and composition. Existing

models of the spectral dependence of $b_b(\lambda)$ are based on Mie calculations and a paucity of empirical data. Measurements of $b_b(\lambda)$ by *Maffione et al.* [1995] in a variety of coastal waters indicate that these models are grossly inadequate. Thus, much research on $b_b(\lambda)$, which is now possible, remains to be done.

Ocean lidar is becoming increasingly important as a research tool in optical oceanography. The current body of knowledge of beam propagation and backscattering in the ocean is based almost entirely on numerical modeling and lidar measurements themselves. Rarely are ocean measurements conducted to study beam propagation and backscattering, and much remains to be learned. Beta Pi, as the only instrument of its kind, will continue to play an important role in ocean lidar research and applications. One area of on-going research by the author is comparing simultaneous measurements with Beta Pi and the bi-static b_b sensors. This investigation will help to characterize both the shape of the VSF in the backward hemisphere and its spectral dispersion.

Submerged source techniques are an effective method for investigating beam propagation. Indeed, the origin of submerged source techniques can be traced directly to beam propagation studies [Duntley, 1971]. Understanding and modeling the point spread function remains an active area of research. In addition to their application to beam propagation studies, submerged source techniques are a powerful means for conducting *in-situ* experiments of radiative transfer theory. Since optical closure is still a distant goal, submerged source experiments need to continue.

Understanding optical propagation in sea ice has grown in importance due to global climate change research. There is evidence, for example, that increases in ultraviolet radiation due to severe ozone depletion in Antarctica, is leading to increases in UV radiation on phytoplankton beneath sea ice. It is therefore important to understand how UV radiation propagates through sea ice. The submerged source technique of Chapter 6, modified for a UV source and detector, would provide important data on this problem. Although there is increased absorption by sea ice in the UV, scattering increases as well so that ω_0 ought to remain high in the UV. Thus the asymptotic-diffusion model developed in Chapter 6 should describe UV propagation in sea ice and can be applied to no-going investigations in this area.

BIBLIOGRAPHY

Bennett, G.T., E.S. Fry, and F.M. Sogandares, 1986. Photothermal measurement of the absorption coefficient of water at 590 nm., *Ocean Optics VIII* , M.A. Blizard, Editor, Proc. SPIE, **637**, 172-180.

Brown, R.A., R.C. Honey, and R.A. Maffione, 1991. Isotropic light source for underwater applications, *Underwater Imaging Photography. and Visibility*, R.W. Spinrad, Editor,Proc. SPIE, **1537**, 147-150.

Dana, D.R. and R.C. Honey, 1990. Optical scattering measurements at Panama City, Florida, in May 1990, SRI Project 8959, Final Report, SRI Inc., Menlo Park, CA.

Doss, W and W. Wells, 1992. Undersea compound radiometer, *Appl. Opt.* , **31**, 4268-4274.

Duntley, S.Q., 1971. Underwater lighting by submerged lasers and incandescent sources, SIO Ref. 71-1, Scripps Institution of Oceanography, La Jolla.

Elliott, J.P., 1955. Milne's problem with a point source, *Proc. Roy. Soc. London Ser. A* , **228**, 424-433.

Fry, E.S., G.W. Kattawar, and R.M. Pope, 1992. Integrating cavity absorption meter, *Appl. Opt.* , **31**, 2055-2065.

Gershun, A.A., 1939. The light field, *J. Math. Phys.* , **18**, 51-151 (transl. by P. Moon and G. Timoshenko).

Gilbert G.D. and R.R. Buntzen, 1986. In-situ measurements of the optical properties of Arctic sea ice, *Ocean Optics VIII*, M.A. Blizard, Editor, Proc. SPIE, **637**, 252-263.

Gilbert, G.D., R.C. Honey, R.E. Myers, and G.P. Sorenson, 1969. Optical absorption meter, SRI Project 7440, Final Report, SRI Inc., Menlo Park, CA, 70 pp.

Gordon, H.R., 1980. Irradiance attenuation coefficient in a stratified ocean: a local property of the medium, *Appl. Opt.*,. **19**, 2092-2094.

Gordon, H.R., 1982. Interpretation of airborne oceanic lidar: effects of multiple scattering, *Appl. Opt.*, **21**, 2996-3001.

Gordon, H.R., 1985. Ship perturbations of irradiance measurements at sea. 1: Monte Carlo simulations, *Appl. Opt.* , **24**, 4172-4182.

Gordon, H.R., 1987. Bio-optical model describing the distribution of irradiance at the sea surface resulting from a point source embedded in the ocean, *Appl. Opt.* , **26**, 4133-4148.

Gordon, H.R., 1993. Sensitivity of radiative transfer to small-angle scattering in the ocean: Quantitative assessment, *Appl. Opt.*, **32**, 7505-7511.

Gordon, H.R., 1994. Equivalence of the point and beam spread function of scattering media: A formal demonstration, *Appl. Opt.*, **33**, 1120-1122.

Gordon, H.R., O.B. Brown, and M.M. Jacobs, 1975. Computed relationships between the inherent and apparent optical properties of a flat homogenous ocean, *Appl. Opt.*, **14**, 417-427.

Gordon, H.R., O.B. Brown, R.E. Evans, J.W. Brown, R.C. Smith, K.S. Baker, and D.C. Clark, 1988. A semianalytic model of ocean color, *J. Geophys. Res.*, **93**(D9), 10909.

Gordon, H.R., K. Ding, and W. Gong, 1993. Radiative transfer in the ocean: computations relating to the asymptotic and near-asymptotic daylight field, *Appl. Opt.*, **32**, 1606-1619.

Grenfell, T.C., 1991. Radiative transfer model for sea ice with vertical structure variations, *J. Geophys. Res.*, **96**, 16,991-17,001.

Grenfell, T.C. and D. Hedrick, 1983. Scattering of visible and near infrared radiation by NaCl ice and glacier ice, *Cold Reg. Sci. Technol.*, **8**, 119-127.

Grenfell, T.C. and G.A. Maykut, 1977. The optical properties of ice and snow in the Arctic Basin, *J. Glaciol.*, **18**, 445-463.

Grenfell, T.C., and D.K. Perovich, 1981. Radiation absorption coefficients of polycrystalline ice from 400-1400 nm, *J. Geophys. Res.*, **86**, 7447-7450.

Helliwell, W.S., G.N. Sullivan, B. Macdonald, and K.J. Voss, 1990. Ship shadowing: model and data comparison, in *Ocean Optics X*, R.W. Spinrad, Editor, Proc. SPIE, **1302**, 55-71.

Henyey, L.C. and J.L. Greenstein, 1941. Diffuse radiation in the galaxy, *Astrophys. J.*, **93**, 70-83.

Hoge, F.E., R.E. Berry, and R.N. Swift, 1986a. Active-passive airborne ocean color measurement. 1: instrumentation, *Appl. Opt.*, **25**, 39-47.

Hoge, F.E., R.N. Swift, and J.K. Yungel, 1986b. Active-passive airborne ocean color measurement. 2: applications, *Appl. Opt.*, **25**, 48-57.

Højerslev, N., 1975. A spectral light absorption meter for measurements in the sea, *Limnol. Oceanogr.* , **20**, 1024-1034.

Højerslev, N., 1994. A history of early optical oceanographic instrument design in Scandinavia, Chapter 7 in *Ocean Optics*, R.W. Spinrad, K.L. Carder, and M.J. Perry, Editors, Oxford University Press, New York, 118-147.

Højerslev, N.K. and J.R.V. Zaneveld, 1977. A theoretical proof of the existence of the submarine asymptotic daylight field, Rept. No. 34, Københavns Univ. Inst. Fysisk Oceanog., Copenhagen, 16 pp.

Honey, R.C., 1979. Beam spread and point spread function and their measurement in the ocean, *Ocean Optics VI*, S.Q. Duntley, Editor, Proc. SPIE, **208**, 242-248.

Honey, R.C. and R.A. Maffione, 1992. Measurement of the optical backscatter coefficient in ocean water, *Aquatic Sciences Meeting Program Abstracts*, Am. Soc. of Limnol. and Oceanogr., Santa Fe, NM., February 1992.

Ishimaru, I. and L. Tsang, 1988. Backscattering enhancement of random discrete scatters of moderate size, *J. Opt. Soc. Am.* A, **5**, 228-236.

Jaffe, J.S., 1995. Monte Carlo modeling of underwater-image formation: validity of linear and small-angle approximations, *Appl. Opt.*, **34**, 5413-5421.

Jerlov, N.G., 1976. *Marine Optics*, 2nd edition, Elsevier Scientific Publishing Company, New York, 231 pp.

Joelson, B.D., 1996. Multiple scattering effects on pulse propagation in optically turbid media, Ph.D. Thesis, Texas A&M University.

Jonasz, M., 1990. Volume scattering function measurement error: effect of angular resolution of the nephelometer, *Appl. Opt.*, **29**, 64-70.

Kirk, J.T.O., 1994. Estimation of the absorption and the scattering coefficients of natural waters by use of underwater irradiance measurements, *Appl. Opt.*, **33**, 3276-3278.

Kopelevich, O.V. and E.M. Mezhericher, 1983. Calculation of spectral characteristics of light scattering by sea water, *Izv. Akad. Nauk SSSR, Fiz. Atmos. Okeana*, **19**, 144.

Kuga, Y. and A. Ishimaru, 1984. Retroreflectance from a dense distribution of spherical particles, *J. Opt. Soc. Am.* A, **1**, 2100-2105.

Kuga, Y. and A. Ishimaru, 1989. Backscattering enhancement by randomly distributed very large particles, *Appl. Opt.*, **28**, 2165-2169.

Kullenberg, G., 1974. Observed and computed scattering functions, in *Optical Aspects of Oceanography*, N.G. Jerlov and E. S. Nielsen, Editors, Academic Press, New York, 25-49.

Light, B., 1995. A structural-optical model of cold sea ice, M.S. Thesis, Univ. of Wash., Seattle, 146 pp.

Longacre, J.R. and M.A. Landry, 1994. In-situ measurements of optical scattering from the water-ice interface of sea ice, *Ocean Optics XII*, J.S. Jaffe, Editor, Proc. SPIE, **2258**, 944-953.

Maffione, R. A., 1993. Results of inherent- and apparent-optical-property measurements at Lake Pend Oreille, *OSA Annual Meeting Technical Digest*, **4**.

Maffione, R.A., 1996. Theoretical developments on the optical properties of highly turbid waters, *Limnol. Oceanogr.*, (submitted).

Maffione, R.A. and D.R. Dana, 1996. *In-situ* characterization of optical backscattering and attenuation for lidar applications, SPIE (in press).

Maffione, R.A. and R.C. Honey, 1991. Results of in-situ closure measurements over long-pathlengths in the ocean, *OSA Annual Meeting Technical Digest*, **17**.

Maffione, R.A. and R.C. Honey, 1992. Instrument for measuring the volume scattering function in the backward direction, *Ocean Optics* XI, Proc. SPIE **1750**, 15-26.

Maffione, R.A. and J.S. Jaffe, 1995. The average cosine due to an isotropic light source in the ocean, *J. Geophys. Res.*, **100**, 13,179-13,192.

Maffione, R.A., D.R. Dana, and R.C. Honey, 1991. Instrument for underwater measurement of optical backscatter, *Underwater Imaging, Photography, and Visibility*, R.W. Spinrad, Editor, Proc. SPIE, **1537**, 173-184.

Maffione, R. A., D. R. Dana, and J. M. Voss, 1995. Spectral Dependence of Optical Backscattering in the Ocean, *OSA Annual Meeting Program*, Portland, Ore.

Maffione, R.A., R. C. Honey, and R. A. Brown, 1991. Experiment for testing the closure property in ocean optics, in *Underwater Imaging. Photography, and Visibility*, R.W. Spinrad, Editor, Proc. SPIE, **1537**, 115-126.

Maffione, R.A., K.J. Voss, and R.C. Honey, 1993. Measurement of the spectral absorption coefficient in the ocean with an isotropic source, *Appl. Opt.*, **32.**, 3273-3279.

Maykut, G.A. and T.C. Grenfell, 1975. The spectral distribution of light beneath first-year sea ice in the Arctic Ocean, *Limnol. Oceanogr.*, **20**, 554-562.

Maykut, G.A., and B. Light, 1996. Refractive index measurements in freezing sea ice and sodium chloride brines, *Appl. Opt* . (in press).

Mertens, L. E., and F. S. Replogle, Jr., 1977. Use of the point spread function for analysis of imaging systems in water, *J. Opt. Soc. Am.*, **67**, 1105-1117.

Miller, D., M.S. Quinby-Hunt, and A.J. Hunt, 1994. Polarization dependent measurement of light scattering in sea ice, *Ocean Optics XII*, J.S. Jaffe, Editor, Proc. SPIE, **2258**, 908-919.

Mobley, C. D., 1994. *Light and Water: Radiative Transfer in Natural Waters*, Academic Press, San Diego, Calif., 592 pps.

Mobley, C.D. 1996. Monte Carlo simulation of a point light source in an infinite medium, Technical Report, SRI International, Menlo Park, 39 pp.

Mobley, C. D., B. Gentili, H. R. Gordon, Z. Jin, G. W. Kattawaar, A. Morel, P. Reinersman, K. Stamnes, and R. H. Stavn, 1993. Comparison of numerical models for computing underwater light fields, *Appl. Opt.*, **32**, 7484-7504.

Moore, C.A. 1985. Development and testing of specialized instrumentation for the measurement of beam-spread function, SRI Project 8266, Final Report. SRI, Inc., Menlo Park, CA.

Moore, C.A., R. Honey, D. Hancock, S. Damron and R. Hilbers, 1984. Development and use of computerized optical sea-truth instrumentation for LIDEX-82, Final Report, 1982, SRI Project 3878, SRI Inc., Menlo Park, California.

Morel, A., 1973. Diffusion de la lumiére par les eaux de mer. résultats experimentaux et approach théorique, in NATO AGARD lecture series No. 61, *Optics of the Sea*, Chap. 3.1, 76 pp. Translation by G. Halikas, Scripps Inst. Oceanogr., La Jolla, 1975, 161 pp.

Morel, A., 1974. Optical properties of pure water and pure sea water, *Optical Aspects of Oceanography*, N.G. Jerlov and E. S. Nielsen, Editors, Academic Press, New York, 1-23.

Oishi, T., 1990. Significant relationship between the backward scattering coefficient of sea water and the scatterance at 120°, *Appl. Opt.*, **29**, 4658-4665.

Pegau, W. S., J. S. Cleveland, W. Doss, C. D. Kennedy, R. A. Maffione, J. L. Mueller, R. Stone, C. C. Trees, A. D. Weidemann, W. H. Wells, and J. R. V. Zaneveld, 1995. A comparison of methods for the measurement of the absorption coefficient in natural waters, *J. Geophys. Res.*, **100**, 13,201-13,220.

Perovich, D.K., and J.W. Govoni, 1991. Absorption coefficients of ice from 250 to 400 nm, *Geophys. Res. Lett.*, **18**, 1233-1235.

Perovich, D.K. and A.J. Gow, 1991. A statistical description of the microstructure of young sea ice, *J. Geophys. Res.*, **96**, 16,943-16,953.

Perovich, D.K. and T.C. Grenfell, 1981. Laboratory studies of the optical properties of young sea ice, *J. Glaciol.*, **27**, 331-346.

Perovich, D.K. and T.C. Grenfell, 1982. A theoretical model of radiative transfer in young sea ice, *J. Glaciol.*, **28**, 341-357.

Perovich, D.K., G.A. Maykut, and T.C. Grenfell, 1986. Optical properties of ice and snow in the polar oceans: I. Observations, *Ocean Optics VIII*, M. Blizard, Editor, Proc. SPIE, **637**, 232-241.

Pettersson, H., 1934. A transparency-meter for sea-water, *Medd. Oceanogr. Inst. Gothenburg, Ser. B*, **4**(4).

Petzold, T. J., 1972. Volume scattering functions for selected ocean waters, SIO Ref. No. 72-78, Scripps Inst. Oceanogr., La Jolla, 79 pps.

Preisendorfer, R. W., 1959. Theoretical proof of the existence of characteristic diffuse light in natural waters, *J. Mar. Res.*, **18**, 1-9.

Preisendorfer, R.W., 1961. Application of radiative transfer theory to light measurements in the sea, *Sym. on Radiant Energy in the Sea*, N.G. Jerlov, Editor, Monograph No. 10, 11-30.

Preisendorfer, R.W., 1965. *Radiative Transfer on Discrete Spaces*, Pergamon, New York, Chapter X.

Preisendorfer, R.W., 1976. *Hydrologic Optics*, in 6 volumes, Pacific Mar. Envirn. Lab/NOAA, Seattle, WA.

Prieur, L., and A. Morel, 1971. Etude théoretique du régime asymptotique: Relations entre charactéristiques optiques et coefficient d'extinction relatif a la pénétration de la lumiére du jour., *Cah. Oceanogr.*, **23**, 35-48.

Roesler, C.S. and R. Iturriaga, 1994. Absorption properties of marine-derived material in Arctic Sea Ice, *Ocean Optics XII*, J.S. Jaffe, Editor, Proc. SPIE, **2258**, 933-943.

Schellenberger, G., 1965. "Über zusammenhänge zwischen optischen parametern von gewässern, *Acta Hydrophys.* **10**, 79-105.

Schoonmaker, J.S., K.J. Voss, and G.D. Gilbert 1989. Laboratory measurements of optical beams in young sea ice, *Limnol. and Oceanogr.*, **34**, 8.

Shuleikin, V.V., 1923. On the colour of the sea, *Phys. Rev.*,**22**, 86-100.

Smart, J.H., A.B. Fraser, and M.J. Jose, 1991. Variability in optical properties across the Gulf of Alaska, *Proc. of Oceans 91*, Honolulu, HI, 657-666.

Smith, R.C., and K.S. Baker, 1981. Optical properties of the clearest natural waters (200-800 nm), *Appl. Opt.*, **20**, 177-184.

Sorenson, G., and R. C. Honey, 1968a. Instrumentation for measuring visibility-limiting characteristics of sea water, *Proc. Soc. Photo-Opt. Instr. Eng.*, **12**, 115-122.

Sorenson, G. and R. C. Honey, 1968b. Underwater visibility meter concept study, SRI Final Report, SRI Inc., Menlo Park, CA.

Spitzer, D. and M. R. Wernand, 1980. *In situ* measurements of absorption spectra in the sea, *Deep-Sea Res.*, **28A**, 165-174.

Stavn, R.H., 1982. The three-parameter model of the submarine light field: radiant energy absorption and energy trapping in nepheloid layers, *J. Geophys. Res.* , **87**, 2079-2082.

Tanis, F.J. 1994. Use of beam spreading measurements to estimate volume scattering properties in sea ice, *Ocean Optics XII*, J.S. Jaffe, Editor, Proc. SPIE, **2258**, 965-973.

Timofeeva, V.A., 1971. Optical characteristics of turbid media of the sea-water type, *Izv. Atmos. Ocean. Phys.*, **7**, 863-865.

Trabjert, I. and N.K. Højerslev, 1996. Temperature influence on light absorption by fresh water and seawater in the visible and the near-infrared spectrum, *App. Opt.*, **35**, 2653-2658.

Trees, C.C. and K. J. Voss, 1990. Optoacoustic spectroscopy and its application to molecular and particle absorption, *Proc. Soc. Photo-Opt. Instrum. Eng.* , **1302**, 149-156.

Tsang, L. and A. Ishimaru, 1984. Backscattering enhancement of random discrete scatterers, *J. Opt. Soc. Am.* A, **1**, 836-839.

Tyler, J.E., and W.H. Richardson, 1958. Nephelometer for the measurement of volume scattering function *in situ*, *J. Opt. Soc. Am.*, **48**, 354-357.

Voss, K.J., 1989a. Electro-optic camera system for measurement of the underwater radiance distribution, *Opt. Eng.*, **28**, 241-247.

Voss, K.J., 1989b. Use of the radiance distribution to measure the optical absorption coefficient in the ocean, *Limnol. Oceanogr.* , **34**, 1614-1622.

Voss, K.J., 1991. variation of the point spread function in the Sargasso Sea, *Underwater Imaging, Photography, and Visibility*, R.W. Spinrad, Editor, Proc. SPIE, **1537**, 97-103.

Voss, K. J. and A. L. Chapin, 1990. Measurement of the point spread function in the ocean, *Appl. Opt.*, **29**, 3638-3642.

Voss, J.M., R.C. Honey, G.D. Gilbert, and R.R. Buntzen, 1992. Measuring the point spread function of sea ice *in-situ*, *Ocean Optics XI*, G.D. Gilbert, Editor,Proc. SPIE, **1750**, 517-526

Wells, W. H., 1969. Loss of resolution in water as a result of multiple small-angle scattering, *J. Opt. Soc. Am.*, **59**, 686-691.

Wilson, W. H., 1979. Spreading of light beams in ocean water, *Ocean Optics VI*, S.Q. Duntley, Editor, Proc. SPIE., **208**, 115-122.

Zaneveld, J. R. V., 1989. An asymptotic closure theory for irradiance in the sea and its inversion to obtain the inherent optical properties, *Limn. & Oceanogr.*, **34**, 1442-1452.

Zaneveld, J.R.V. and H. Pak, 1972. Some aspects of the axially symmetric submarine daylight field, *J. Geophys. Res.* , **77**, 2677-2680.

Zaneveld, J. R. V., and W. S. Pegau, 1993. Overview of the optical closure experiment at Lake Pend Oreille, *OSA Annual Meeting Technical Digest,*, **4**.

Zaneveld, J.R.V., R. Bartz, and J. C. Kitchen, 1990. A reflective-tube absorption meter, *Proc. Soc. Photo-Opt. Instrum. Eng.* ,**1302**, 124-136.